

ABLATION COOLED MATERIAL REMOVAL WITH BURSTS OF ULTRAFAST PULSES

A DISSERTATION SUBMITTED TO
THE GRADUATE SCHOOL OF ENGINEERING AND SCIENCE
OF BILKENT UNIVERSITY
IN PARTIAL FULFILLMENT OF THE REQUIREMENTS FOR
THE DEGREE OF
DOCTOR OF PHILOSOPHY
IN
ELECTRICAL AND ELECTRONICS ENGINEERING

By
M. Can Kerse
January, 2016

ABLATION COOLED MATERIAL REMOVAL WITH BURSTS of
ULTRAFAST PULSES

By M. Can Kerse

January, 2016

We certify that we have read this dissertation and that in our opinion it is fully adequate, in scope and in quality, as a dissertation for the degree of Doctor of Philosophy.

F. Ömer Ilday(Advisor)

Ergin Atalar(co. Advisor)

Atilla Aydınlı

Ayhan Altıntaş

Mehmet Burçin Ünlü

Onur Ferhanoglu

Approved for the Graduate School of Engineering and Science:

Levent Onural
Director of the Graduate School

ABSTRACT

ABLATION COOLED MATERIAL REMOVAL WITH BURSTS OF ULTRAFAST PULSES

M. Can Kerse

Ph.D. in Electrical and Electronics Engineering

Advisor: F. Ömer Ilday

January, 2016

Material processing with femto-second pulses allows precise and non-thermal material removal and being widely used in scientific, medical and industrial applications. However, due to low ablation speed at which material can be removed and the complexity of the associated laser technology, where the complexity arises from the need to overcome the high laser induced optical breakdown threshold for efficient ablation, its potential is limited. Physics of the interaction regime hinders a straightforward scaling up of the removal rate by using more powerful lasers due to effects such as plasma shielding, saturation or collateral damage due to heat accumulation. In analogy to a technique routinely used for atmospheric re-entry of space shuttles since 1950s, ablation cooling, is exploited here to circumvent this limitation, where rapid successions of pulses repeated at ultra-high repetition rates were applied from custom developed lasers to ablate the target material before the residual heat deposited by previous pulses diffuse away from the interaction region. This constitutes a new, physically unrecognized and even unexplored regime of laser- material interactions, where heat removal due to ablation is comparable to heat conduction. Proof-of-principle experiments were conducted on a broad range of targets including copper, silicon, thermoelectric couplers, PZT ceramic, agar gel, soft tissue and hard tissue, where they demonstrate reduction of required pulse energies by three orders of magnitude, while simultaneously increasing the ablation efficiency by an order of magnitude and thermal- damage-free removal of brain tissue at $\sim 2 \text{ mm}^3/\text{min}$ and tooth at $\sim 3 \text{ mm}^3/\text{min}$, an order-of-magnitude faster than previous results.

Keywords: Ablation cooling, Ultrafast material processing, Burst mode laser, Non-thermal ablation, Ultra-high repetition rate.

ÖZET

ULTRA-HIZLI ATIMLI KÜME MODU İLE SOĞUK ABLASYONLU MALZEME KALDIRMA

M. Can Kerse

Elektrik ve Elektronik Mühendisliği, Doktora

Tez Danışmanı: F. Ömer Ilday

Ocak, 2016

Femtosaniye lazer atımları, gerek geniş çaplı bilimsel çalışmalarda, gerekse de tıp ve endüstri alanlarında kesin, keskin ve ısısız hasara sebep olmayan malzeme işleme imkanı vermektedir. Ancak, bu potansiyeli düşük malzeme kaldırma hızı ve karmaşık lazer teknolojisi sebebiyle sınırlıdır. Bu tür lazer sistemlerinin karmaşık olmasının temel nedeni, etkin ablasyon için gerekli olan yüksek atım enerjisi eşliğidir. Buna ek olarak, lazer - malzeme etkileşimi fiziği de daha güçlü lazerler ile kaldırılan malzeme miktarının doğrusal artışına plazma kalkını, saturasyon ve ısı birikiminden dolayı oluşan çevresel hasar gibi sebeplerden dolayı engel teşkil etmektedir. Burada, bahsedilen sınırları aşmak için, uzay mühendisliğinde 1950'lerden beri sıklıkla kullanılan, ablasyon ile soğutma, prensibinden faydalanarak, özel olarak ürettiğimiz sistemlerden çıkan lazer atımlarını arka arkaya çok hızlı bir şekilde hedef noktasına, etkileşim bölgesi içinde bir önceki atımdan geriye kalan ısı daha etrafa yayılmadan tatbik etmekteyiz. Böylelikle, ablasyon dolayısıyla malzemeden uzaklaşan ısının, malzeme içine iletilen ısıya eşit olabileceği farkına varılmamış ve hatta keşfedilmemiş lazer-malzeme etkileşimi rejimini göstermekteyiz. Bu olguyu göstermek için bakır, silikon, termoelektrik malzeme, PZT seramik, agar jöle, yumuşak ve sert dokuyu da içeren çok geniş yelpazedeki örnekler üzerinde yaptığımız deneylerle ablasyon için gerekli atım enerjilerini 1000 kat azaltırken, ablasyon etkinliğini de 10 kat artırmakla beraber çevre dokuya hasar vermeden malzeme kaldırma hızı beyin dokusunda $\sim 2 \text{ mm}^3/\text{dk}$ ve diş dokusu üzerinde $\sim 3 \text{ mm}^3/\text{dk}$ mertebelerine ulaşmıştır ki literatürde daha önceden yayınlanan sonuçlardan 10 kat daha fazladır.

Anahtar sözcükler: Soğutmalı ablasyon, Ultra-hızlı malzeme işleme, Küme modlu lazer, Isısız olmayan ablasyon, Ultra-yüksek tekrar frekansı.

Acknowledgement

I admit that coming that far was a long, tiresome and emotional process. In an engineering point of view, one could say that the system that we are fed as the input is highly non-linear, so, one should always compensate all the losses and hard times encountered and learn how to get up after all times that you fall. As once I heard from a colleague, “No man is an island”. I could not have finished without the emotional and intellectual support that I get. The following people have been indispensable to me during the process that I underwent in graduate school.

I thank: My advisors, F.Ömer Ilday and Ergin Atalar for their kindest support, motivation and guidance in every possible way, where they all made this possible; My thesis committee, Atilla Aydınli, Ayhan Altıntaş, who, together with my advisors helped and motivated me about my future career and Onur Ferhanoglu and Mehmet Burçin Ünlü; Y.Ziya Ider, Orhan Arıkan, Ömer Morgül, Nail Akar, Vakur B. Ertürk, Levent Onural and Ibrahim Turan for their guidance and sincere support during my PhD.; Tarık Çelik for his guidance before and during my undergraduate times; Hamit Kalaycoğlu and Parviz Elahi for their amazing contributions especially with their amazing skills and with their unique laser systems, and for their sincere friendship; Barbaros Çetin for his amazing contributions on numerical simulations and his intimate support; Gamze Aykut for animal care and brain slicing; my friend and my colleague Mehmet Doğan Aşık for histological analyses and for sincere talks; Denizhan Koray Kesim, Seydi Yavaş, Önder Akçaalan, Bülent Öktem, Heinar Hoogland, Ronald Holzwarth, Serim Ilday, Onur Tokel, Ghaith Makey, Saniye Sinem Yılmaz, Samad Nadimi, Inam Mirza, Koray Yavuz, Mustafa Karatok, Hayrettin Köymen, Haydar Çelik, Oktay Algın, Volkan Aykaç, Yaşar Aykaç, Turgay Dalkara, Müge Yemişçi Özkan, Kıvılcım Kılıç, Siyami Karahan, Hasan Güner, Arda Büyüksungur for all their help, contributions and useful comments on the work; BIOMATEN (METU, Ankara, Turkey) for micro-CT analyses; Gizem Gençoğlu and Mutlu Erdoğan for making all boring days shiny at the office; Daniel Press, Ahmet Turnalı, Özgün Yavuz, Ihor Pavlov and all other current and former members of UFOLAB; Aydan Ercingöz, Taner Demir, Volkan Açikel, Emre Kopanoğlu, Esra Abacı Türk,

Umut Gündoğdu and all other current and former members of UMRAM; Murat Güre, Ergün Karaman, Coşkun Kocabaş, Osman Balcı, Ertuğrul Karademir, Emre Ozan Polat, Mehmet Altun, Kemal Sağlam, Bedrettin Duran and other members of ARL.

I also thank all the good and best friends: Ihsan Yapıcıoğlu, Muammer Yalçın, Emre Özyıldız, F. Göktürk Cirit, H. Buğra Akcan, Semih Karacasu, Muratcan Akyıl, Özgür Benzeş, Ali Deniz Gülaçtı, Ahmet Şensoy, Alexander Suhre, Gökçe Balkan, Ege Çakır and all former and possible future members of our amateur band Vertigo; Özlem Şeyda Uluç, Doğaç Gülnerman, Ozan Özgül, Bora Biçer, Zahide Pamir Karatok, Burak Elibol, Merve Şahinsoy, Kemal Gürel, H. Ibrahim Şahin, Selçuk Çelebi, Sertuğ Kostik, Oganalp Canatan, Ali Emre Mutlu, Ozan Alparslan, Aybüke Yedidağ, Gökçe Aydoğdu, Elif Aydoğdu, Gülis Zengin, Ali Özgür Yöntem, Niyazi Şenlik, Kıvanç Köse, Nil Tuğçe Patan, Aslı Karataş, Evrim Akgün, Pınar Sezginalp, Selin Açık, Eda Çalgüner; Engin Demir, Taylan Berkin Töral, A. Uğur Ergen, Deniz Yurtsever and all other scuba-diving buddies and BILSAT.

I thank my parents Mualla & İlhan Kerse and my beloved brother Kıvanç Kerse for their love, understanding and for always being *there*. Especially I thank my father for his guidance through this crucial trip. Last but not least, I heartily thank my beloved wife Bahar Özkan Kerse, without her love, friendship, support and understanding, I couldn't have sustained my energy and motivation throughout these challenging times.

I acknowledge TÜBİTAK BİDEB 2211 funding for supporting me during my PhD and the work presented in this thesis was supported from the EU FP7 Project CROSS-TRAP, ERC Consolidator Grant “Nonlinear Laser Lithography”, Ministry of Health and TÜBİTAK grants 112T944, 209T058.

I devote this thesis to uncle Şener Bilgin, who has recently died from cancer, and to my friend M. Deniz Aksoy who died in a tragic traffic accident. I still remember our research related conversations. My dear friend, thanks to your visionary advices at the early stages of my graduate studies, I could orient my research in this interesting direction. May them both rest in peace...

Contents

- 1 INTRODUCTION** **1**

- 2 MATHEMATICAL MODEL and NUMERICAL SIMULATIONS** **10**
 - 2.1 Toy Model 10
 - 2.1.1 Claim 1: Reduced heating of the target 15
 - 2.1.2 Claim 2: Scaling down of pulse energy with repetition rate 18
 - 2.2 Numerical Simulations Based on Single Temperature Model . . . 23
 - 2.3 Numerical Simulations Based on Two Temperature Model 28

- 3 EVIDENCE of ABLATION COOLING** **36**

- 4 COPPER, SILICON and PZT CERAMIC PROCESSING** **43**
 - 4.1 Cu and Si Ablation Efficiency Experiments 44
 - 4.2 Cu and Si Micro-Machining with Uniformly Distributed and Bursts of Pulses 53
 - 4.3 PZT Processing 62

- 5 SOFT and HARD TISSUE ABLATION** **64**
 - 5.1 Agar Gel and Soft Tissue Ablation 65
 - 5.1.1 Experiments with 300 fs system 66
 - 5.1.2 Experiments with 1 ps system 72
 - 5.2 Hard Tissue (Dentine) Ablation 75
 - 5.2.1 Experiments at 500 MHz repetition rate 75
 - 5.2.2 Experiments at 1.73 GHz intra-burst repetition rate 82

6	CONCLUSIONS	92
A	Burst Mode Laser Systems	106
A.1	1 MHz - 3.5 GHz intra-burst repetition rate, 1 ps pulse duration .	106
A.2	22.3 MHz intra-burst repetition rate, 300 fs pulse duration	110
A.3	500 MHz intra-burst repetition rate, 1 ps pulse duration	113
B	Parameters of Toy Model in Figures	115

List of Figures

2.1	A simple schematic of temperature elevation above critical value due to single pulse heating. The area of painted region gives a proportional value to the energy removed from the material	13
2.2	A simple schematic of the temperature elevation above critical value due to multiple pulses. The area of painted regions gives a proportional value to the energy removed from the material	14
2.3	Generic dependence of thermal energy diffusing into the bulk (solid red line) as a function of repetition rate according to the toy model. The repetition rate is normalized to the characteristic repetition, which is $f_0 = 1/\tau_0$. The experimentally investigated repetition rates for silicon are shown as blue circles to provide context. . . .	16
2.4	Scaling of ablation amount with pulse energy and repetition rate, based on the toy model: (a) The analytic solution of the surface temperature, and (b) amount of ablated material based on toy model is plotted for $N = 25$ pulses at a repetition rate of 100 MHz (blue line), $N = 100$ pulses at a repetition rate of 400 MHz (red line) and $N = 400$ pulses at a repetition rate of 1600 MHz (orange line). The pulse energies are scaled down with increasing number of pulses, such that the total energy is the same for each case. Parameters are: $T_c = 15000K$, $T_0 = 300K$, $\tau_R/\tau_0 = 5$, $\Delta T = 50000K/\eta$, where $\eta = 1, 4, 16$ for 100 MHz, 400 MHz, 1600 MHz, respectively.	21
2.5	Predictions of toy model with the calculations for 1 MHz, 25 MHz, 108 MHz, 432 MHz and 3456 MHz.	22

2.6 Surface and sub-surface heating during ablation with (a) laser pulses at low repetition rate and (b) laser pulses at high repetition rate. Please note that per pulse energies, so, the total delivered energy, are exactly the same 25

2.7 (a) Schematic representation of the ablation process for low (negligible ablation cooling) and high (significant ablation cooling) repetition rates, respectively: Temperature profiles are illustrated (left) for $t = t_1$, which is shortly after the arrival of the first pulse for both cases; (middle) for $t = t_2$, which is shortly after (before) the arrival of the last (second) pulse for the high-repetition-rate (low-repetition-rate) laser; (right) for $t = t_3$, which is shortly after the arrival of the last pulse for the low-repetition-rate laser. The colouration of the target material is based on simulation results shown in (b), according to the colour bar indicated therein and at the indicated time intervals of $t = t_1$, $t = t_2$, and $t = t_3$. (b) Calculated evolution of the temperatures at the surface (solid lines) and below (at a depth of 30 times the optical penetration depth) the surface (dotted lines) for repetition rates of 10 MHz (black lines) and 1600 MHz (blue lines). The pulse energies and number of pulses are the same for both cases. The higher repetition rate results in significantly lower temperatures below the surface due to ablation cooling. (c) Expanded view of the shaded section of the plot in (b) 26

2.8 Calculated evolution of the surface temperature (dashed lines) and amount of ablated material (solid lines) for repetition rates of 100 MHz (green lines), 400 MHz (blue lines) and 1600 MHz (red lines). The ablation rate remains approximately the same when the product of pulse energy and repetition rate is maintained. The spikes in surface temperatures precisely indicate the arrival of pulses, which are not shown explicitly for clarity. 27

2.9 Simulations showing the effect of ablation cooling for Ni based on STM: Calculated evolution of the surface temperature, and 5 μm below the surface, for repetition rates of 10 MHz and 1600 MHz. The results are qualitatively similar to the results of the STM shown above. The spikes in surface temperatures precisely indicate the arrival of pulses, which are not shown explicitly for clarity. The results are qualitatively similar to the results of the TTM shown below. 33

2.10 Simulations showing the effect of ablation cooling for Ni based on TTM: Calculated evolution of the surface temperature, and 5 μm below the surface, for repetition rates of 10 MHz and 1600 MHz. The results are qualitatively similar to the results of the STM shown above. 34

2.11 Simulations for Ni based on STM: Calculated evolution of the surface temperature (dashed lines) and amount of ablated material (solid lines) for repetition rates of 100 MHz (green lines), 400 MHz (blue lines) and 1600 MHz (red lines). The ablation rate slightly increases when the product of pulse energy and repetition rate is maintained. The predictions are in excellent qualitative agreement with those of the TTM shown below. 35

2.12 Simulations for Ni based on TTM: Calculated evolution of the surface temperature (dashed lines) and amount of ablated material (solid lines) for repetition rates of 100 MHz (green lines), 400 MHz (blue lines) and 1600 MHz (red lines). The ablation rate slightly increases when the product of pulse energy and repetition rate is maintained. The predictions are in excellent qualitative agreement with those of the STM shown above. 35

3.1 Experimental setup and temperature measurement to evidence ablation cooling. (a) Thermoelectric module placement and direction of laser illumination. (b) Picture of the actual setup. 38

3.2 Measured thermoelectric voltages induced on Thermoelectric Modules. (a) Measured thermoelectric voltages induced on Thermoelectric Module 1 (target material, solid lines) and the Thermoelectric Module 2 (attached to the coverslip that collects some of the ablated particles, dashed lines) for laser processing with significant ablation cooling (blue lines) and with negligible ablation cooling (red lines). (b) Measurements of thermoelectric voltage induced due to temperature rise in the target material during laser processing with and without ablation cooling, implemented with burst and uniform modes, respectively. The results consistently show that the target material heats substantially less with ablation cooling than without ablation cooling, even though the total laser energy incident is the same. 40

3.3 Transparency test. (a) Measurements of temperature in thermoelectric module 2 (connected to coverslip), when the same laser processing procedure is applied without a target material below. Any heating is due to absorption of the laser beam by the coverslip. Measurements made on a fresh sample (black trace) and samples which have been partially covered with ablated material using the burst mode (blue trace) and the uniform mode (red trace) are virtually identical. (b) Picture of coverslip, which was processed using burst mode and uniform mode, shows the vast difference in deposited material and consequently the difference in ablation efficiency. 41

3.4 Burst and uniform mode application on black painted thermoelectric module. (a) Image of painted thermoelectric module after processing. Some paint remains after application of uniform mode whereas, burst mode removes all the paint (clear zone). (b) Temporal evolution of thermoelectric voltage change of the painted substrate with and without ablation cooling, implemented with burst (blue line) and uniform (red line) modes, respectively. . . . 42

4.1 Raster scan pattern 44

4.2 Scaling down of pulse energy with increasing repetition rate. Volume of (a) Cu and (b) Si ablated by a single burst of pulses as a function of burst energy and burst fluence for different intra-burst repetition rates. Ablation efficiency in terms of number of atoms of (c) Cu and (d) Si ablated per incident photon as a function of pulse energy and pulse fluence for different repetition rates. Full symbols highlight inverse scaling of pulse energy with repetition rate. 46

4.3 Scaling down of pulse energy with increasing repetition rate including the toy model. Volume of (a) Cu and (b) Si ablated by a single burst of pulses as a function of burst energy and burst fluence for different intra-burst repetition rates. 47

4.4 Representative crater depth profiles obtained at various repetition rate and pulse combinations after a single burst. 48

4.5 Photographs of the 20 μm -thick copper foil after a series of trepanning operations with laser processing, including 60 zones with 150- μm diameter and 60 zones with 500- μm diameter. 54

4.6 Microscope images of 20 μm thick copper foil after trepanning together with the bar chart representing number of passes required vs. laser mode. (a) 400 pulsed burst at 1.73 intra-burst repetition rate. (b) 100 pulsed burst at 432 MHz intra-burst repetition rate. (c) 25 pulsed burst at 27 MHz intra-burst repetition rate. (d) 27 kHz uniform repetition rate. (e) Number of passes required for drilling vs. laser operation mode. Each trepanning pass takes 0.15 seconds with 10 mm/s scanning speed in order to have 50 % overlapping spots. The error bars reflect the standard deviation of 10 trials for each mode. 56

4.7 SEM images of thin copper foils after trepanning with 400-pulsed bursts at 1.73 GHz pulse repetition rate, 1 kHz burst repetition rate, 600-nJ pulse energy and 240 mW of average power on sample (burst mode) and corresponding uniformly repeated pulses at 27 kHz, 9.7- μ J pulse energy and 240 mW of average power (uniform mode). The scan speed was 10 mm/s in order to maintain 50 % overlap between bursts: (a) 150- μ m diameter circle removed with burst mode. (b) 500- μ m circle removed with burst mode. (c) The 20- μ m thick and 500- μ m wide foil piece, which was removed in (b). (d) 150- μ m diameter circle removed with uniform mode. (e) 500- μ m circle removed with uniform mode. (f) The 20- μ m thick and 500- μ m wide foil piece removed with uniform mode in (e). 57

4.8 SEM images of 150- μ m thick copper sheets after a scan following a very tightly wound spiral pattern (12.5- μ m separation between each spiral arm) with 400 pulsed bursts at 1.73 GHz pulse repetition rate, 1-kHz burst repetition rate, 600 nJ of pulse energy and 240 mW of average power on sample (burst mode) and corresponding uniformly repeated pulses at 27 kHz, 9.7 μ J of pulse energy and 240 mW of average power (uniform mode). The scan speed is 10 mm/s in order to maintain 50% overlap between bursts. (a) Burst-mode processed hole with 500- μ m diameter. (b), (c) Magnified edges of (a). (d) Uniform-mode processed hole with 500- μ m diameter. (e), (f) Magnified edges of (d). 59

4.9 Drilling holes through 450- μ m thick silicon wafer with burst mode: SEM images of holes formed by scans following a very tightly wound spiral pattern (12.5 μ m separation between each spiral arm) with bursts of 400 pulses at 1.73 GHz intra-burst repetition rate, 1 kHz burst repetition rate, pulse energy of 600 nJ, and 240 mW of average power incident on sample. The scan speed was set to 10 mm/s in order to achieve 50% overlap between bursts. (a), (b) Two 500- μ m through holes created using the burst mode. (c), (d) Magnified view of edges. 60

- 4.10 SEM images of 450- μm thick silicon wafers using uniform mode operation, tracing over concentric circles (12.5 μm separation between each circle) using 9.6- μJ pulses at 25 kHz and 240 mW of average power. The scan speed was 10 mm/s. (a) Extensive SiO_2 formation is observed after processing. (b) Image taken from the same region, after the sample was chemically cleaned to remove the SiO_2 formation. (c), (d) Magnified edges of (b). 61
- 5.1 (a) Microscope image of hydrogel block, raster-scanned with 200-kHz uniform repetition rate and 4-pulsed burst mode at the indicated pulse energies. Micro CT images of the processed rat brain tissue sample: (b) Top view of the coronal slice where four excisions made in (1) 4 pulsed-burst mode and (2) 200-kHz uniform repetition rate. (c) Sagittal view of the excisions in (b). 67
- 5.2 (a) Color and contrast enhanced sagittal view of 4-pulsed burst ablation region from 3D volumetric reconstruction of Micro CT data. Dashed lines represent the edges of processed region. (b) Light microscopy image of 4-pulsed burst ablation region after histological preparation. (c) Color and contrast enhanced sagittal view of 200 kHz ablation region from 3D volumetric reconstruction of Micro CT data. Dashed lines represent the edges of processed region. Arrows show the thermal damage zone. (d) Light microscopy image of 200 kHz ablation region after histological preparation. . . . 69
- 5.3 SEM images of the edges. (a) Lesion ablated with 4 pulsed-burst mode. (b) Lesion ablated with 200 kHz uniform mode. 71

5.4 Histology results of the regions ablated with intra-burst repetition rate of 432 MHz with 7 pulses per burst, burst repetition rate of 27 kHz and average power of 2.7 W. (a) Light microscope image of H&E stained ablated region. (b) Fluorescent microscope image of DAPI stained ablated region, obtained from another sample. (c) Light microscope image of H&E stained ablated region, where scanning has been momentarily stopped to intentionally cause a heat-affected zone. (d) Fluorescent microscope image of the DAPI-stained ablated region, where scanning has been momentarily stopped to intentionally cause a heat-affected zone, obtained from another sample. 73

5.5 Comparison of burst-mode and uniform-mode ultrafast laser processing based on light microscopy: Laser ablation results for human dentine obtained while keeping all laser parameters (including peak and average power, spot size and total exposure) fixed except for mode of operation, (a) 500 MHz burst mode with scan velocity of 0.1 mm/s, (b) 500 MHz burst mode with scan velocity of 0.5 mm/s, (c) 25 kHz uniform mode with scan velocity of 0.1 mm/s, (d) 25 kHz uniform mode with scan velocity of 0.5 mm/s. 77

5.6 3D depth profile obtained with Laser Scanning Microscope: (a) 500 MHz burst mode with scan velocity of 0.1 mm/s, (b) 500 MHz burst mode with scan velocity of 0.5 mm/s. 78

5.7 LSM-acquired high-resolution image showing the excellent edge equality of the same holes obtained at scan speeds of (a) 0.1 mm/s and (b) 0.5 mm/s. 78

5.8 Scanning Electron Microscope images of ablated lesions of human tooth processed with (a) 25 pulsed 500 MHz burst mode with burst period of 1 ms and at a scanning velocity of 0.1 mm/s and (b) 25 pulsed 500 MHz burst mode with burst period of 1 ms and at a scanning velocity of 0.5 mm/s. It should be noted that cracks at the edges are due to vacuum procedure during SEM imaging, and the bright zones are due to the excess charge accumulation on tooth sample. 79

5.9 Surface profile of tooth samples, after ablation process, obtained with an OCT system. Processed with (a) 500 MHz burst mode and at a scanning velocity of 0.1 mm/s, (b) 500 MHz burst mode and at a scanning velocity of 0.5 mm/s, (c) 25 kHz uniform repetition rate mode at a scanning velocity of 0.1 mm/s and (d) 25 kHz uniform repetition rate mode at a scanning velocity of 0.5 mm/s. 80

5.10 B-Scan results of tooth samples, after ablation process, obtained with the OCT system. The slice in view was obtained from the middle of the ablation zone. Processed with (a) 25 pulsed 500 MHz burst mode with burst period of 1 ms and at a scanning velocity of 0.1 mm/s, (b) 25 pulsed 500 MHz burst mode with burst period of 1 ms and at a scanning velocity of 0.5 mm/s, (c) 25 kHz uniform repetition rate mode at a scanning velocity of 0.1 mm/s and (d) 25 kHz uniform repetition rate mode at a scanning velocity of 0.5 mm/s. The dashed red lines indicate the surface. 81

5.11 Section view of tooth samples obtained with in the OCT system. The dark spots due to carbonization of tissue during 25 kHz uniform repetition rate processing are identified. Processed with (a) 25 pulsed 500 MHz burst mode with burst period of 1 ms and at a scanning velocity of 0.5 mm/s and (b) 25 kHz uniform repetition rate mode at a scanning velocity of 0.5 mm/s. 81

5.12 Comparison between the effect of burst and uniform modes after processing at low speeds (safe power levels for uniform mode): (a) Optical image of the ~800 μm-deep hole drilled in Experiment 5 (using burst mode at 1728 MHz intra-burst repetition rate). (b) LSM image of the same hole. (c) Optical image of the ~200 μm-hole drilled in Experiment 6 (using uniform mode at 1 kHz repetition rate). (d) LSM image of the same hole. The processing results for uniform mode have excellent quality, when the repetition rate and average power are low enough. It is also important to note that the burst mode is at least 4 times more efficient despite using 25 times less energetic pulses. 84

5.13 Comparison between the effect of burst and uniform modes after processing at low speeds (safe power levels for uniform mode): (a) Optical image of the $\sim 1200 \mu\text{m}$ -deep hole drilled in Experiment 3 (using burst mode at 1728 MHz intra-burst repetition rate). (b) LSM image of the same hole. (c) Optical image of the $\sim 250 \mu\text{m}$ -hole drilled in Experiment 4 (using uniform mode at 1 kHz repetition rate). (d) LSM image of the same hole. The processing results for uniform mode have excellent quality, when the repetition rate and average power are low enough. It is also important to note that the burst mode is at least 5 times more efficient despite using 25 times less energetic pulses. 86

5.14 Close-up imaging of hole created in Experiment 3. (a) LSM image of the edge of the hole recorded before the SEM imaging. (b) SEM imaging of the hole (compare with the optical microscope image in Fig. 5.13 a. and b.). The chips and crack has occurred during the vacuum formation as required for SEM imaging. 87

5.15 Comparison between the effect of burst and uniform modes after processing at high speeds: (a) Optical image of the $\sim 750 \mu\text{m}$ -deep hole drilled in Experiment 7 (using burst mode at 1728 MHz intra-burst repetition rate). (b) LSM image of the same hole. (c) SEM image of the $\sim 750 \mu\text{m}$ -deep hole drilled in Experiment 7 (using burst mode at 1728 MHz intra-burst repetition rate). (d) Optical image of the hole drilled in Experiment 8 (uniform mode at 25 kHz repetition rate). (e) LSM image of the same hole. (f) SEM image of the aborted drilling experiment (Experiment 8), using uniform mode at 25 kHz repetition rate. The experiment was aborted due to excessive carbonisation. These results show that despite using same average powers and delivering same total amount of energy, burst mode is able to successfully drill dentine without any apparent heat damage, whereas uniform mode results in excessive thermal damage. 89

5.16 Scaling the ablation rate. (a) 400 pulsed-burst mode with 600 nJ/pulse energy at 1 kHz burst repetition rate equivalent to 240 μ J/burst energy and 240 mW average power. (b) 25 kHz uniform mode with 9.7 μ J/pulse energy equivalent to 240 mW average power. Total scan time = 322 seconds (50 total passes) obtained with 10 mm/s scan speed in order to have 50 % overlap. 91

A.1 Schematic diagram of the experimental setup. CFBG: chirped fiber bragg grating, AOM: acousto-optical modulator, AWG: arbitrary waveform generator, FPGA: field programmable gate array, DM: dichroic mirror, WDM: wavelength division multiplexer, PBS: polarizing beam splitter, PPF: pump protection filter, SM: single-mode, DC: double-clad. 107

A.2 Repetition Rate Multiplier of Fig. A.1. CFBG: chirped fiber bragg grating, WDM: wavelength division multiplexer, PBS: polarizing beam splitter, PPF: pump protection filter, SM: single-mode, DC: double-clad, 50/50: 50 % coupler. 108

A.3 (a) Pulse trains of amplified bursts: 15 ns long burst with 50 pulses, 130 ns long burst with 400 pulses and 230 ns long burst with 800 pulses. Due to the band-width limitation of the diagnostics, the pulses inside bursts are unresolvable. (b) Optical spectrum of burst output with 230 ns burst duration. (c) Autocorrelation result for compressed pulses at 16 μ J after pulsed power amplifier stage. . . 109

A.4 (a) Intensity (top) and pulse separation time (bottom) variability of the 3.5 GHz oscillator output. (b) Measured RF spectrum of the 3.5 GHz seed signal. Highly resolved 10 KHz span around the center frequency (top). 20 GHz span showing the frequency components and the harmonics (bottom). (c) Measured RF spectrum of 230 ns long bursts repeated at 1 kHz: Frequency span of 20 MHz centered at 3.455 GHz (bottom), close up 1 kHz lines with a span of 10 kHz versus frequency offset from the central frequency of 3.455 GHz, with a resolution band-width of 30 Hz (top). . . . 110

A.5	Schematic diagram of the laser and tissue processing setups; PM, polarization maintaining; PPF, pump protection filter; WDM, wavelength division multiplexer; DC, double clad; DM, Dichroic Mirror; HWP, half-wave plate.	111
A.6	For 8 μJ compressed pulse energy: (a) measured optical spectrum, (b) measured temporal profile of 200 kHz pulses and 4-pulsed bursts, (c) measured, simulated and PICASO-retrieved autocorrelation, (d) inferred pulse shape using the PICASO algorithm and simulated pulse shape.	112
A.7	Laser, optical scanning and sample positioning setup custom-built for the hard-tissue and piezoelectric ceramic cutting experiments.	114

List of Tables

4.1	Comparison of Cu processing results from this work and previous publications.	51
4.2	Comparison of Si processing results from this work and previous publications.	52
4.3	Comparison of results on cutting PZT ceramic into 1 mm-diameter circular sections.	63
5.1	Comparison of results for drilling through dentine without active cooling.	83

Chapter 1

INTRODUCTION

Applications of ultrafast laser material processing have become extremely diverse [1–12], enabled by rapid developments that have taken place in the field of ultrafast lasers, particularly, in Yb-doped fibre [13–15] and solid state lasers [16] in the past decade. Despite these improvements, ultrafast material processing is still complex, costly and quite slow in terms of material removal [17], which is particularly limiting for biological tissue removal, rendering ultrafast lasers uncompetitive compared to mechanical techniques for many applications [9, 18]. There is great interest in increasing the ablation rate and decreasing the pulse energy thresholds, and, in turn, laser complexity.

Surgical potential of the laser was recognized immediately following its invention [19]. Within a year after the demonstration of the first laser, an ophthalmic application has been shown, in which a detached human retina was restored [20]. Since then, it has become a widely used procedure. The most distinctive feature of a laser system is its wavelength, because materials have wavelength-dependent absorption and scattering, which are quantitative measures of how deep a laser beam may penetrate into the material and deviate from its straight trajectory, respectively. In addition to wavelength dependence, an equally important attribute is the type of energy delivery, such as continuous or pulsed deliveries. Pulse duration together with the power density (W/cm^2) directly affects the chemical

and mechanical interactions occurring inside the material upon given an incident beam. These interactions are mainly photochemical, thermal, plasma induced, photoablation and multiphoton absorption [21]. While other medical applications of lasers in Continuous Wave (CW) regime such as Laser Interstitial Thermal Therapy (LITT); or in quasi CW and nanosecond to microsecond pulsed regime such as urological applications have proliferated, medical operations in which tissue is removed precisely with a laser are limited mostly to ophthalmology. This is in part due to the difficulty of preventing collateral damage to surrounding tissue during irradiation. This issue is resolved, in principle, by ablation using femtosecond pulses with low average power, typically at low (Hz or kHz) repetition rates [6]. However, this method suffers from a very low rate of ablation. While this is tolerable in ophthalmology due to the small volumes needed to be ablated [21], it renders most tissue removal applications of lasers, including hard tissue ablation uncompetitive compared to mechanical removal techniques [18]. A straightforward way to increase the removal rate is to increase the laser repetition rate. However, the average power is also increased, resulting in significant collateral tissue damage due to accumulated heat effects.

Lasers may have many advantages especially in neurosurgery, since they can be used for precise tissue processing, vaporization and coagulation. As opposed to the interventions aimed on liver tumors, wherein temperature rise in the adjacent healthy tissues might be tolerated, minimal thermal damage to adjacent tissues is a primary goal in most of the neurosurgical operations and eye surgeries. A more recent area of research is the plasma mediated ablation and photodisruption, which is achieved by ultra-short laser pulses with extremely high peak intensity. This process leads to nonlinear absorption in the material, which then leads to ionization of the atoms and the molecules at the focal spot and results in plasma formation. In order to induce optical breakdown in solids, power densities more than 10^{11} W/cm² in fluids, 10^{14} W/cm² are needed [21–24]. Being above the power density threshold yields very well defined removal of tissue with no evidence of thermal and mechanical damage. The local electric field determines if the optical breakdown is achieved or not. For precise tissue removal, upon illuminating the focal spot with picoseconds pulses, typical threshold intensity

of optical breakdown is in the order of 10^{11} W/cm², which corresponds to 10^7 V/cm. This value is approximately equal to intra-molecular Coulomb electric fields, which is the required condition for ionization formation of plasma. If laser illumination at the focus continues, within few picoseconds very large free electron density is obtained, which has the essential role in plasma ionization. For different pulse duration intervals, the cause of plasma formation differs. For example, if the pulse duration lies within the nanoseconds regime, thermionic emissions cause plasma formation. In contrast, for lasers operating in femtosecond - picosecond regime, multi-photon absorption is responsible for plasma formation. Upon the formation of plasma, the free electrons cause an avalanche effect and accelerated electron collides with the others and ionizes them. Exceeding optical breakdown intensity threshold is an important phenomenon because, even inside a weakly absorbing medium, the induced plasma makes it possible to remove the material. With some approximations, plasma absorption coefficient is given by the formula:

$$\alpha_{pl} = \frac{v_{ei} w_{pl}^2}{nc w^2} \quad (1.1)$$

where, v_{ei} is the mean collision rate of free electrons and ions, n is the index of refraction, c is the speed of light, w is the wave frequency and w_{pl} is the plasma frequency. It is seen that, the plasma absorption coefficient α_{pl} is enhanced in the near infra-red region of spectrum. Also, it is a nonlinear function of electron density, $\alpha_{pl} \propto N^2$. As an example in Ref. [21], by increasing the fluence from 3 J/cm² to 23 J/cm², α_{pl} increases from 0.1 cm⁻¹ to 100 cm⁻¹. Docchio *et al.* investigated the plasma lifetime in water for several pulse durations and observed that plasma luminescence follows a similar time trajectory with the pulse itself with a delay and widening in the temporal distribution upon reaching the necessary intensity [25]. Besides, as the electron density increases more, laser photons are scattered more by the plasma, which can be thought as saturation. So, there is a critical electron density at which the net amount of energy is not converted more to plasma energy, rather reaches on the tissue surface. This critical energy density is obtained when plasma frequency is equal to the incident waves frequency.

$$N_{crit} = \frac{\epsilon_0 m_e}{e^2} w^2 \quad (1.2)$$

where, m_e is the electron mass, e is the electron charge and ϵ_0 is the vacuum

permittivity. In the visible range this electron density becomes in the order of 10^{20} cm^{-3} . The threshold energy is proportional to the square root of exposure time per single pulse ($E_{th} \sim \sqrt{\tau}$). Therefore, intensity threshold is also reduced for picoseconds pulses and is in the order of 1.5 TW/cm^2 .

With the help of the plasma mediated ablation, if the proper laser parameters are achieved thermal diffusion becomes too slow to dissipate the energy during this plasma lifetime [8, 11]. If this happens, the thermal energy is confined to the focal zone and no thermal effect is seen in the adjacent tissue. However, if the intensity is too high, then a phenomenon called photodisruption occurs. Due to this effect, mechanical shockwaves start to radiate, which has an undesired effect especially on corneal ablations [26].

Even though the tissue examples are used in previous paragraphs, the physics behind the plasma mediated ablation is similar for other materials. Considering the effect of a single ultra-fast pulse on material, ablation with femto-second pulses has several advantages compared to longer pulse lengths. First, for a given fluence (J/cm^2), higher temperatures and pressures are obtained as compared to ablation with ns pulses, since the laser energy is delivered before significant thermal conduction time. Second, there are not any other secondary interactions between the laser pulse and the ablated material. Higher photon densities also result in a larger kinetic energy for plume and particles ejected from the surface due to the Coulomb explosion [27, 28]. Shortly, keeping the pulse energy constant, as pulse duration reduces, Intensity becomes greater than binding energy of the molecules followed by a rapid ejection.

Fiber delivery of continuous laser energy for thermal therapies is widely being used for ablation of tumors. Especially, in order to ablate bigger tumors, this method is well established. Since the ablation of a tissue is a thermal process and the thermal heating is related with absorption, the delivery of CW light energy to the tumor tissue results in heating. Besides, Magnetic Resonance Imaging (MRI) is sometimes preferred to guide the fibers to the tumor tissue inside the liver or brain. In that case, MR thermometry is used to measure the change in the temperature in real-time. This mechanism provides a visual feedback to the

operator to track down the ablation process both qualitatively and quantitatively [29]. However, if the pulse width is decreased in the order of sub-picoseconds, which is required for more precise and non-thermal tissue processing, required peak energy to form the plasma at the focal point becomes too high. Due to this fact, high intensity pulses cannot be delivered with silica fibers, since they will burn out. In their work, Wahrburg *et.al.* showed that it is possible to deliver the pulsed light energy to the ablation site inside the brain. However, they could not use fibers. Instead of fiber delivery, they used a stereotactic probe with which the high pulse energy is delivered through a hollow waveguide. The probe diameter was 5.5 mm and can only follow a straight trajectory up to 100 mm, into the brain [30,31]. Because of this situation, collateral mechanical damage may be hazardous. To ablate deep seated brain tumors, surgeon needs to get at the tumor site very carefully, without damaging the healthy tissue. In such a situation, MRI is the perfect tool since it gives real time visual feedback and discriminate the tumor from its surrounding healthy tissue. Besides, in terms of fiber delivery, the diameter of the probe can be reduced to sub-milimeter range.

In this thesis, a new regime of laser-material interactions is introduced. All the major results of this thesis form the basis of a research article in Ref. [32]. During ablation, heat energy within the ablated volume is carried away from the system. This effect forms the basis of ablation cooling, which is routinely used as a minimal mass-requiring approach to thermal protection during atmospheric re-entry of rockets since 1950s [33]. Unlike ablation cooling for rockets, laser ablation is not continuous, but only takes place during and shortly after a laser pulse is incident. For the laser parameters used to date, ablation cooling has been negligible as a cooling mechanism in comparison to heat conduction (diffusion), which is continuously occurring. In this thesis, it is shown that the ablation rate can be increased by around three orders of magnitude and thereby exploit ablation cooling. This is a new regime of laser-material interactions with several interrelated advantages: At sufficiently high repetition rates, most of the residual heat deposited by each pulse will not have yet diffused out of the volume to be ablated by the time the next pulse arrives. Thus, each pulse targets an already hot material, which lowers the ablation threshold with major side benefits, such

as minimizing plasma shielding, reducing shock wave and cavitation bubble formation [8, 23], self-focusing (for transparent targets) [10], as well as drastically simplifying the required laser technology.

Since the laser technology required to demonstrate ablation cooling did not exist, special femtosecond fibre lasers [34–37] developed in our laboratory have been utilized during the experiments. Ablation cooling kicks in above a certain repetition rate, which depends on the thermal conductivity of the target material. Continuous trains of energetic pulses at such high repetition rates correspond to prohibitively average powers, in addition to the fact that the speed with which the laser beam can be repositioned over a target is limited. As a remedy, burst-mode operation has been implemented, which was first demonstrated by R. Marjoribanks, et al. [38]. In burst mode, the laser produces groups of high-repetition-rate pulses, which are, in turn, repeated with a lower frequency. The duty cycle of pulsation can be adjusted to set the average power. Indeed, burst-mode material processing already has substantial benefits [38–40], but the possibility of ablation cooling has not been recognized. This is likely to be related to the commonly held view that shielding effects preclude efficient ablation at high repetition rates [41].

In this thesis, the physics of ablation-cooled regime is highlighted through a toy analytical model that can be solved exactly. Moreover, numerical simulations based on parabolic one step (single temperature model) and parabolic two step (two temperature model) radiation models are established. The toy model makes two main predictions, which are confirmed by numerical simulations of the heat diffusion equation, as well as experiments described below: (i) Increasing the repetition rate at constant pulse energy significantly reduces heating of surrounding regions. (ii) However, the repetition rate should not be increased at constant energy, as shielding effects will prevent efficient ablation [41]. The trick is to exploit a scaling property that the toy model predicts and full simulations confirm: The ablation rate can be maintained by increasing the repetition rate and the number of pulses by a certain factor, while decreasing the pulse energy by the same factor.

Experimental proof of the ablation cooling effect is presented by measuring

the temperature of a target material and of the ablated particles, simultaneously. The laser beam is focused onto and ablates the surface of a thermoelectric module. This causes a temperature difference between the laser-targeted top surface and the bottom surface, which generates a voltage difference by the Seebeck effect. A portion of the particles ejected from the surface during ablation stick to a microscope cover-slip, which is held ~ 1 mm above the target. A second thermoelectric module is used to similarly monitor the temperature of the cover-slip. The measured temperatures of the target and the glass cover-slip confirm that the target heats less and the cover-slip heats more in the ablation-cooled regime, compared to the traditional regime.

Experiments on a broad range of materials have been performed and the results are given to demonstrate the universal validity of two main predictions of the toy model. Copper and silicon were chosen as examples to metal and semiconductor targets, respectively, because their ablation rates with ultrafast pulses are well documented. Total volumes of material ablated by a single burst as a function of burst energy are presented. At low repetition rates of 1 MHz and 25 MHz, the results are similar. The benefits of ablation cooling become appreciable once the repetition rate is increased to 108 MHz. If the repetition rate is further increased, efficiency drops at high pulse energies. This is a consequence of the expected shielding effect. The solution is to decrease the pulse energy, increase the number of pulses in each burst and the intra-burst repetition rates, e.g., from 25 pulses per burst at 108 MHz to 100 pulses per burst at 432 MHz, and finally to 800 pulses (with 32 times lower energy) per burst at 3464 MHz. With proper scaling down of the pulse energy, the higher repetition rates result in even slightly higher total ablation compared to the performance recorded at 108 MHz, indicating that the shielding effects are completely overcome. The same scaling trend holds for both targets, even though Si and Cu have entirely different optical and physical characteristics, highlighting the universality of the ablation cooling effect. These results prove the prediction of decreasing pulse energy with increasing repetition rate and are presented in this thesis.

As a straightforward consequence of the higher ablation efficiency and energy conservation, laser-deposited energy is expected to be better confined to the laser

spot and any undesired thermal effects to the surrounding region should be reduced substantially in the ablation cooling regime. This effect is most important for and most easily demonstrated through processing of temperature-sensitive materials, particularly biological tissue. To this end, we have performed systematic comparisons between burst-mode (appreciable ablation cooling) and uniform-mode (negligible ablation cooling) processing with identical laser, focusing and scanning systems. This way, it was possible to minimize experimental uncertainties and to ensure that all parameters, except the temporal sequence of the pulses, could be kept exactly the same.

Piezoelectric lead zirconate titanate (PZT) ceramics have wide-ranging applications, including ultrasonic sensor arrays [42] or miniature motors, for which the material has to be cut at a high degree of precision. Laser cutting of PZT to arbitrary shapes is possible, but can cause irreversible deterioration of piezoelectricity due to heating. Both the burst-mode (ablation-cooling regime) and the uniform-mode (traditional regime) were used to cut 1 mm-diameter circular sections of PZT and characterized their electromechanical coupling coefficient to ascertain how well the inherent piezoelectricity of the material is preserved. The cutting time was reduced by a factor of 9 for burst mode and resulted in 2 times higher coupling coefficient.

Tissue removal may well be regarded as the ultimate test of suppression of thermal effects since only a few degrees of temperature rise can lead to degradation. Numerous hard tissue experiments were conducted on human dentine to illustrate the benefits of ablation cooling and to contrast burst and uniform modes. Virtually identical samples were processed using both uniform and burst-mode pulses. At low average powers, both the traditional regime and the ablation-cooled regime provide excellent results, as expected. However, the latter achieves more than 4 times higher ablation, despite using 25 times smaller pulse energies. Likewise, using 170 times smaller pulse energy yields 2 times more ablation. More dramatically, increasing the processing speed by a factor of 25 with a corresponding increase in power, ablation-cooled regime achieves excellent results, while the uniform mode causes excessive carbonization. Since every laser, focusing and

scanning parameters were otherwise identical, the results conclusively demonstrate that thermal effects are greatly reduced as a result of ablation cooling. The ablation rate presented here of $3.0 \text{ mm}^3/\text{min}$ is similar to those of nanosecond Er:YAG lasers used in dentistry [9] and 5 times higher than the highest values reported using ultrafast lasers [9], even though 150 times smaller pulse energies presented in this study.

There are numerous applications for soft tissue ablation [6, 10, 23] particularly targeting the brain [43], where the extreme precision afforded by a laser would be of paramount importance. Comparisons on the effectiveness of ablation cooling in selective tissue removal from freshly harvested whole rat brains is given. When the average power is low, as expected, both regimes avoid thermal side effects, yielding damage-free ablation. However, ablation-cooled regime has a clear advantage in terms of thermal effects already at moderate powers: While low-repetition-rate ablation causes a wide heat-affected zone with damaged neighbouring cells, devascularisation and prominent tissue loss, there is no significant heat damage in the ablation-cooled regime. The corresponding ablation rate of $0.75 \text{ mm}^3/\text{min}$ is 8 times higher than the use of $165\text{-}\mu\text{J}$, 180-fs pulses, with which a 0.55-mm^3 section of brain tissue was removed in 360 s [11], even though 55 times lower pulse energies is reported in this study. With ablation-cooling, at a much higher power of 2.7 W, virtually thermal-damage-free results are obtained at a record-high ablation rate of $1.5 \text{ mm}^3/\text{min}$.

Chapter 2

MATHEMATICAL MODEL and NUMERICAL SIMULATIONS

In this chapter, an intuitive analytical toy model which basically helps to understand the phenomenon through a basic perspective, in terms of energy delivered and energy removed from the system is going to be explained together with numerical one dimensional parabolic one step and two step radiation models and simulations.

2.1 Toy Model

The physics of ablation-cooled ultrafast material processing can be highlighted through a toy model that can be solved exactly. We assume that each pulse in a train of N pulses gives rise to an instantaneous fixed temperature rise of ΔT , which is roughly proportional to pulse energy, E_p . So, immediately after the first pulse, the surface temperature is $T_{1+} = T_0 + \Delta T$, where ablation has not yet been considered yet. Then, the material initially cools with a

$$\frac{1}{\sqrt{\tau_0 + t}} \tag{2.1}$$

dependence on time delay after arrival of a pulse [44], where τ_0 is a characteristic time scale chosen to avoid a singularity at $t = 0$. Without loss of generality, the cooling of the surface after the arrival of the first pulse can be expressed as,

$$T(t) = T_0 + \Delta T \sqrt{\frac{\tau_0}{(\tau_0 + t)}} \quad (2.2)$$

Momentarily before the second pulse arrives, the surface temperature is

$$T_{2-} = T_0 + \Delta T \sqrt{\frac{\tau_0}{(\tau_0 + \tau_R)}} \quad (2.3)$$

where, τ_R is inverse of the repetition rate, *i.e.* repetition period. The second pulse results in an increase of the surface temperature by ΔT , so immediately afterwards,

$$T_{2+} = T_0 + \Delta T \sqrt{\frac{\tau_0}{(\tau_0 + \tau_R)}} + \Delta T \quad (2.4)$$

Then, the surface starts to cool again, but since the material below the surface is no longer at T_0 , but approximately at $T_0 + \Delta T \sqrt{\frac{\tau_0}{(\tau_0 + \tau_R)}}$, the subsequent cooling is going to correspond to thermal relaxation for a temperature difference of ΔT , meaning the decay will have the following form,

$$T(t) = T_0 + \Delta T \sqrt{\frac{\tau_0}{(\tau_0 + \tau_R)}} + \Delta T \sqrt{\frac{\tau_0}{(\tau_0 + t)}} \quad (2.5)$$

Similarly, one can calculate the surface temperature immediately before and after the third pulse, or more generally, after the n^{th} pulse,

$$T_n = T_{n-1} + \Delta T \sqrt{\frac{\tau_0}{(\tau_0 + \tau_R)}} = T_{n-1} + \delta T \quad (2.6)$$

where, $\delta T \equiv \Delta T \sqrt{\frac{\tau_0}{\tau_0 + \tau_R}}$ is the small net increase in target temperature by single pulse and is used to simplify the notation. Then, after the n^{th} pulse,

$$T_n = T_0 + (n - 1)\delta T + \Delta T \quad (2.7)$$

Now, assume that ablation takes place above a critical value if and when $T_n > T_c$. Here, it is also assumed that the absorption of the material is high enough, such that all the absorption energy (prior to diffusion) is located at the surface. This is a good assumption for metals, for which the absorption depth is typically less than even the wavelength of the laser. Furthermore, the amount of ablation per pulse is also quite small and comparable to the absorption depth, which is given in Table 4.1. Therefore, it is reasonable to assume that one such layer of material is ablated when $T_n > T_c$ and most of the energy contained within that chunk of material is carried away. Then the new surface starts cooling from an initial value of T_c . The inherent assumption here is that ablation process does take finite amount of time, during which the immediate neighbouring point has a chance to heat up to T_c , but of course not any higher, since it would also be ablated otherwise and the new surface starts cooling from this point. In other words, the amount of material being ablated may be underestimated by this assumption, but is reasonable to consider, given its relative simplicity. Thus, temperature will have the profile of,

$$T_n \propto T_c \sqrt{\frac{\tau_0}{(\tau_0 + \tau_R)}} \quad (2.8)$$

Since the previous pulse was able to increase above the critical temperature, the next one is also guaranteed, as well. In fact, every pulse from this point onwards has an identical effect. Two simple sketches are given in Figs. 2.1 and 2.2.

Then, what matters is to find after which pulse (if ever), the ablation takes place for the first time and each subsequent pulse is then guaranteed to cause ablation and to first order, ablating the same amount of material. Since each pulse increases the surface temperature by δT , the critical temperature is going to be reached by the m^{th} pulse, where $(T_0 + (m - 1)\delta T + \Delta T) > T_c$, *i.e.* $m \geq 1 + \frac{T_c - T_0 - \Delta T}{\delta T}$, where m is actually the largest integer not greater than m . For

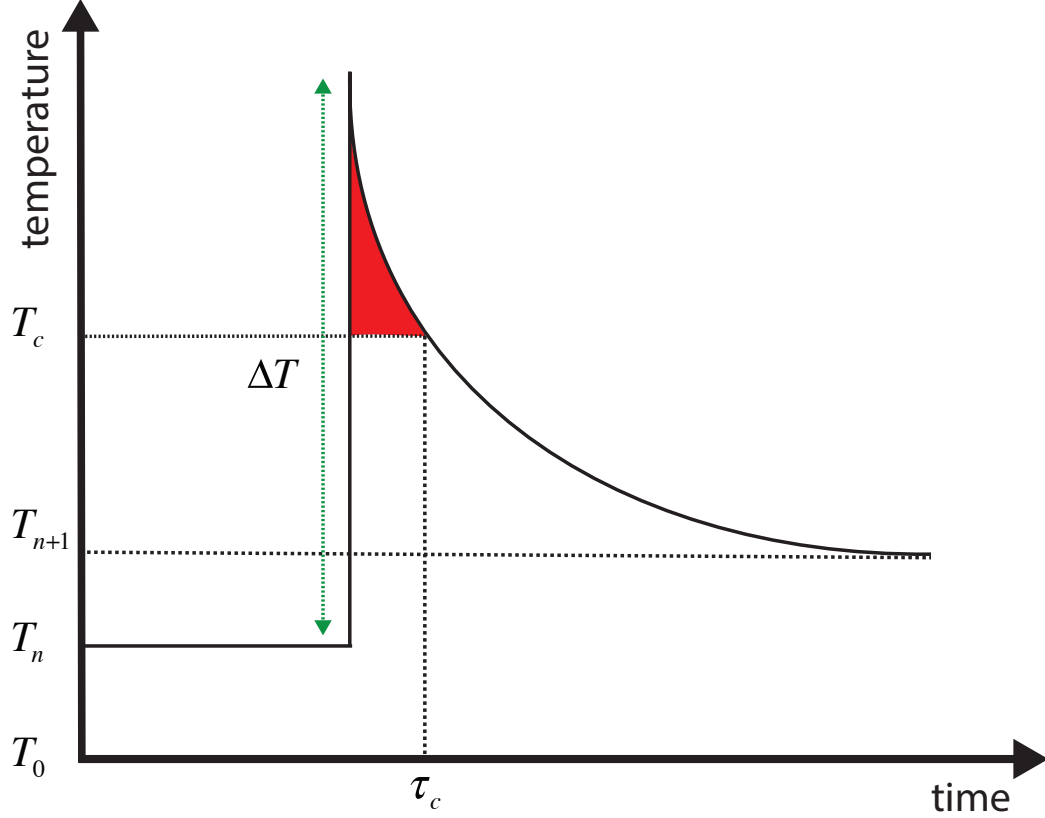


Figure 2.1: A simple schematic of temperature elevation above critical value due to single pulse heating. The area of painted region gives a proportional value to the energy removed from the material

large numbers of pulses (of interest in this work), this subtle difference can safely be ignored. The total ablated mass is given by, $(N - m)\beta E_p$, where β is a proportionality factor that is related to the heat capacity, density, as well as other physical properties of the target material. Inserting in the value of m , ablated volume can be written as,

$$V_{ablated} = \beta \left(N - \frac{T_c - T_0 - \Delta T + \delta T}{\delta T} u(T_c - T_0 - \Delta T) \right) E_p u(N - m) \quad (2.9)$$

where $u(x)$ is the unit step function. The first step function distinguishes between the individual pulses above and below the ablation threshold and the second step function ensures that ablation values are not negative, but zero, if the critical

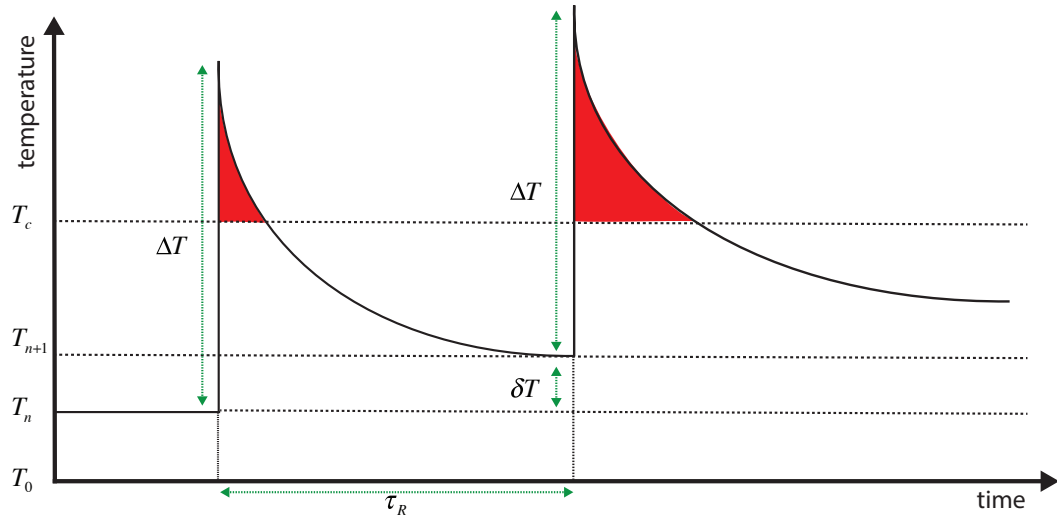


Figure 2.2: A simple schematic of the temperature elevation above critical value due to multiple pulses. The area of painted regions gives a proportional value to the energy removed from the material

temperature is not reached before the pulse train is over). The second term on the right is non-zero only for sub-threshold pulses and refers to the number of (ideally few) pulses that are required to increase the surface temperature step by step until the ablation threshold is exceeded with the energy of the pulse, but these preparatory pulses do not cause ablation themselves. In the limit of low repetition rates, $\delta T \rightarrow 0$ and the second term diverges, which means that no ablation can start if the individual pulses do not exceed the threshold in this limit, as expected.

2.1.1 Claim 1: Reduced heating of the target

In the ablation-cooling regime, amount of ablation is significantly more than for traditional regime, corresponding to low repetition rates (for given pulse energy). Since a large portion of the incident energy is carried out of the system through ablation, the heating of the bulk of the material is significantly reduced. The amount of absorbed laser energy that diffuses as heat to the bulk of the target material can be estimated. Total heat diffusion is, to first order, proportional to the quantity of the material and the amount of cooling that occurs between two subsequent pulses. If ablation is occurring, temperature immediately after a pulse is T_c and right before the arrival of the next pulse it is $T_0 + (T_c - T_0)\sqrt{\frac{\tau_0}{\tau_0 + \tau_R}}$. Therefore, amount of heat diffusion per pulse is,

$$E_{diff} = \alpha \left(T_c - (T_c - T_0)\sqrt{\frac{\tau_0}{\tau_0 + \tau_R}} - T_0 \right) E_p \quad (2.10)$$

where, α is related to the heat capacity of the target material. Let's first calculate the case for which individual pulses exceed the ablation threshold. Then, for N pulses,

$$E_{diff} = \alpha(T_c - T_0) \left(1 - \sqrt{\frac{\tau_0}{\tau_0 + \tau_R}} \right) N E_p \quad (2.11)$$

The traditional regime corresponds to individual pulses exceeding the ablation threshold and applied at low repetition rates, such that $\tau_R \gg \tau_0$. Then, total heating of the target is obtained as,

$$E_{diff} = \alpha(T_c - T_0) N E_p \quad (2.12)$$

and the limit of ultra-high repetition rates, as stipulated by the ablation-cooled regime is calculated as,

$$E_{diff} = \alpha(T_c - T_0) \frac{\tau_R}{2\tau_0} N E_p \quad (2.13)$$

which converges to zero heating in the limit of infinite repetition rate, but of course, other physical factors come into play that render this toy model invalid before that limit is approached. The variation of heating as a function of the repetition rate is given in Fig. 2.3.

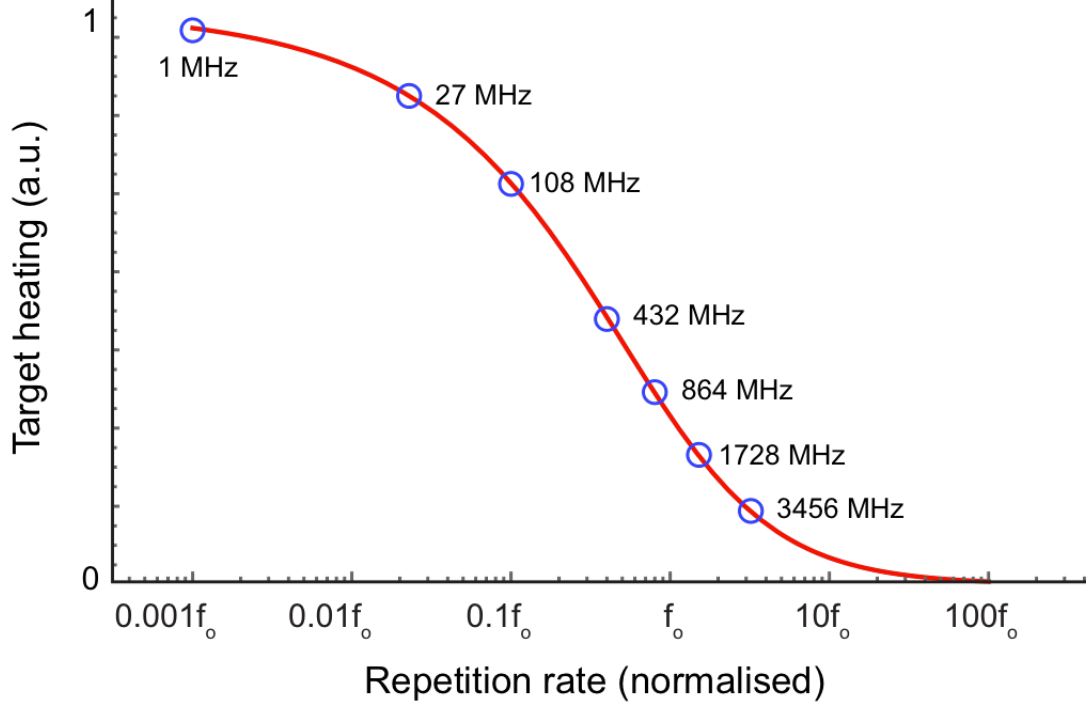


Figure 2.3: Generic dependence of thermal energy diffusing into the bulk (solid red line) as a function of repetition rate according to the toy model. The repetition rate is normalized to the characteristic repetition, which is $f_0 = 1/\tau_0$. The experimentally investigated repetition rates for silicon are shown as blue circles to provide context.

In the simple analysis above, effects such as plasma shielding were not considered. As recognized in the literature before, it is clearly undesirable to increase the repetition rate, while using pulse energies that exceed the ablation threshold. The trick here is to simultaneously scale down the pulse energy to values much below this threshold, which will be discussed in following sub-section.

Now, let's calculate the amount of heating of the target for this case. Ablation starts after the m^{th} pulse. Heat that diffuses once the ablation is initiated will be given by the expression above, replacing N with $(N - m)$. For the first group of pulses that will not cause ablation, but will step-by-step build up the surface

temperature, the temperature immediately after the n^{th} pulse and immediately before the next pulse is given by $T_0 + n\delta T + \Delta T < T_c$ and $T_0 + (n + 1)\delta T$, such that,

$$E_{diff} = \alpha(\Delta T - \delta T)mE_p \quad (2.14)$$

Putting these two results together, for a general pulse train composed of sub-threshold pulses, total heating of the target is calculated as,

$$E_{diff} = \alpha(T_c - T_0) \left(1 - \sqrt{\frac{\tau_0}{\tau_0 + \tau_R}} \right) (N - m)E_p + \alpha(\Delta T - \delta T)mE_p \quad (2.15)$$

The first term on the right corresponds to the heating caused by the pulses after ablation has started and the second term corresponds to the heating caused by the initial pulses preceding ablation. This result reduces to that of the traditional regime when each pulse exceeds ablation threshold ($m = 0$) and low repetition rate ($\tau_R \gg \tau_0$). As expected, it vanishes as $\tau_R \rightarrow 0$. In the limit of low repetition rate and pulse energies below threshold, $E_{diff} = N\alpha\Delta TE_p$, which physically means that all the absorbed energy goes into heating the target material.

2.1.2 Claim 2: Scaling down of pulse energy with repetition rate

A major benefit of the ablation-cooling regime is that required pulse energies can be scaled down by large factors by simultaneously increasing the repetition rate. This scaling is well-enough motivated by the laser technology: It is generally not difficult at all to generate a large number of low-energy pulses that constitute a highly energetic burst. In contrast, it is incomparably more difficult to generate a single pulse of equivalent energy. A second motivation arises from desire to be deeper into the ablation-cooling regime, which stipulates extremely high repetition rates for target materials with high thermal conductivity. As will be shown in this section, both of these motivations converge to a simple approximate scaling law.

When increasing the repetition rate, as it is well known, plasma (and particulate) shielding effects will render ablation highly inefficient. Simultaneously decreasing the pulse energy alleviates this effect, since the density (therefore reflectivity) of the plasma (or cloud of particulates) depends on the pulse energy. Let's take Eqn. 2.9, and simplify it by focusing on the case of direct interest here, namely when individual pulses do not exceed the ablation threshold. Let's assume that the pulse train is long enough to initiate ablation long before the pulse train is finished ($m \ll N$), which allows the unit step functions to be dropped,

$$V_{ablated} = \beta \left(N - \frac{T_c - T_0 - \Delta T + \delta T}{\delta T} \right) E_p \quad (2.16)$$

By assuming that the dominant absorption is linear, $\Delta T = \zeta E_p$. This is not true for transparent targets, which rely on multi-photon absorption, but it is a good enough approximation for the purpose here. In addition, a generalization is relatively straightforward and in even that case, once ablation starts and plasma is formed, linear absorption arises. Recalling the definition of δT from Eqn. 2.6,

$$V_{ablated} = \beta \left[N - \frac{T_c - T_0 - \zeta E_p + \zeta E_p (1 + \frac{\tau_R}{\tau_0})^{-1/2}}{\zeta E_p (1 + \frac{\tau_R}{\tau_0})^{-1/2}} \right] E_p \quad (2.17)$$

After simple scaling of pulse energy, repetition period and total number of pulses ($E_p \rightarrow E_p/\eta_1$, $\tau_R \rightarrow \tau_R/\eta_2$, $N \rightarrow N\eta_3$), the amount of ablation is given by,

$$V_{ablated} = \beta \left[N\eta_3 - \frac{(T_c - T_0)\eta_1/\zeta E_p + \left((1 + \frac{\tau_R}{\tau_0\eta_2})^{-1/2} - 1 \right)}{(1 + \frac{\tau_R}{\tau_0\eta_2})^{-1/2}} \right] \frac{E_p}{\eta_1} \quad (2.18)$$

$$V_{ablated} = \beta E_p \left[\frac{N\eta_3}{\eta_1} + \frac{1 - \left(1 + \frac{\tau_R}{\tau_0\eta_2} \right)^{1/2}}{\eta_1} - \frac{(T_c - T_0)}{\zeta E_p} \left(1 + \frac{\tau_R}{\tau_0\eta_2} \right)^{1/2} \right] \quad (2.19)$$

The dominant term is the first one, which clearly requires $\eta_1 = \eta_2 \equiv \eta$ o preserve amount of ablation. The second term relates to number of non-ablation-contributing pulses, which should be kept small for efficient ablation. Inserting in this condition, last equation becomes,

$$V_{ablated} = \beta E_p \left[N + \frac{1 - \left(1 + \frac{\tau_R}{\tau_0\eta_2} \right)^{1/2}}{\eta} - \frac{(T_c - T_0)}{\zeta E_p} \left(1 + \frac{\tau_R}{\tau_0\eta_2} \right)^{1/2} \right] \quad (2.20)$$

The second term on the right is always negative, but it is reduced by η , which means that either ablation remains the same or even improves. In addition, this term is always small compared to N in the ablation-cooling regime. Therefore, we focus on the last term, which can, in general, be very large enough to even prevent ablation, if pulse energy is too small. This is another expression of the need for $m \ll N$. Approaching the ablation-cooling regime, $\tau_R > \tau_0$ still, and Eqn. 2.20 gives approximately,

$$V_{ablated} = \beta E_p \left[N - \sqrt{\frac{\tau_R}{\tau_0 \eta_2}} \left(\frac{1}{\eta^2} - \frac{(T_c - T_0)}{\zeta E_p} \right) \right] \quad (2.21)$$

In the other extreme of deep into the ablation-cooling regime, $\tau_R \ll \tau_0$, Eqn. 2.20 gives,

$$V_{ablated} = \beta E_p \left[N - \frac{\tau_R}{2\tau_0 \eta \eta_2} - \frac{(T_c - T_0)}{\zeta E_p} \left(1 + \frac{\tau_R}{2\tau_0 \eta_2} \right) \right] \quad (2.22)$$

In both cases, ablation either remains approximately the same or improves with $\eta_2 > 1$. Therefore, a reasonable choice is to select $\eta_2 = \eta$, since it is desirable to scale up the repetition rate for the purpose of reducing thermal effects, independently of the ablation amount under consideration here. Thus, the scaling law is obtained, which highlights: As the repetition rate and number of pulses is increased by a certain factor and the pulse energy is reduced by the same factor, total amount of ablation remains approximately the same. This phenomenon is depicted in Figs. 2.4 and 2.5, where, detailed information on the parameters is given in Appendix B.

The toy model is too simplistic to yield quantitatively accurate predictions, yet, it gives a simple understanding considering the energy in/energy out formulation. It is intended only to provide intuition for the main claims of ablation cooling regime. It is a quasi-zero dimensional model in that it only describes the surface point, which is moving as material is ablated. The two main predictions of the toy model can be summarized as: (i) much lower heating around the focal point and (ii) ablation threshold can be scaled down by increasing the repetition rate. However, numerical solutions of the heat diffusion equation can explain the physics in much detail, which will be covered in the next two sections.

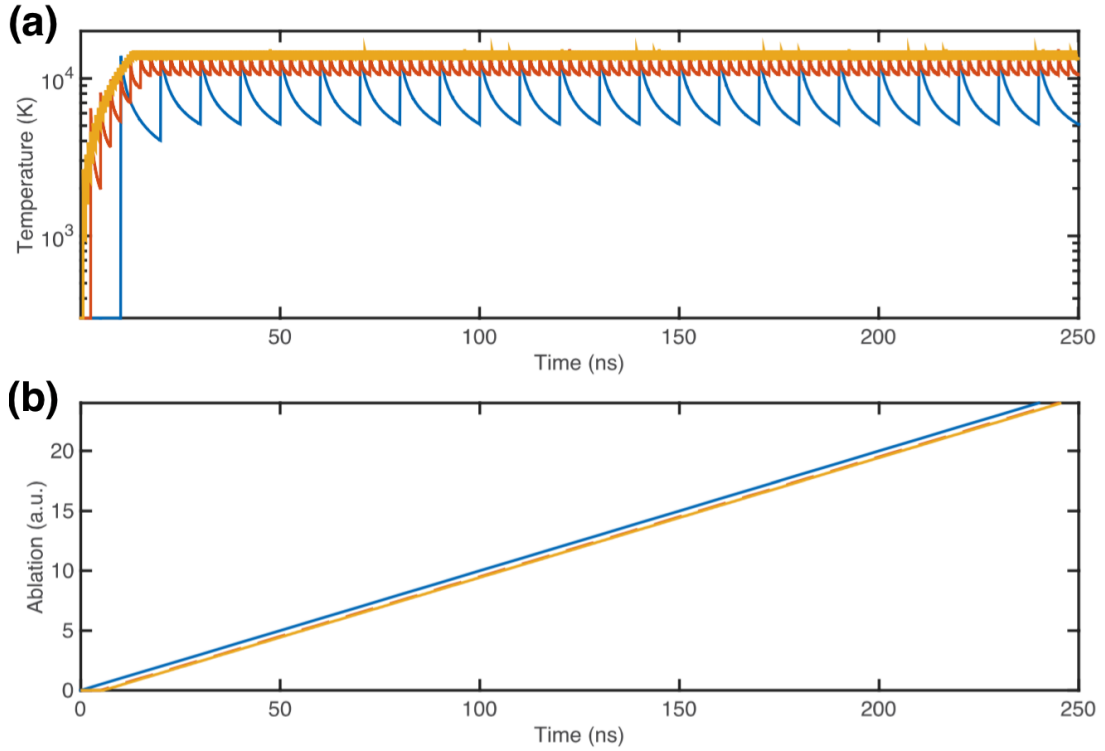


Figure 2.4: Scaling of ablation amount with pulse energy and repetition rate, based on the toy model: (a) The analytic solution of the surface temperature, and (b) amount of ablated material based on toy model is plotted for $N = 25$ pulses at a repetition rate of 100 MHz (blue line), $N = 100$ pulses at a repetition rate of 400 MHz (red line) and $N = 400$ pulses at a repetition rate of 1600 MHz (orange line). The pulse energies are scaled down with increasing number of pulses, such that the total energy is the same for each case. Parameters are: $T_c = 15000K$, $T_0 = 300K$, $\tau_R/\tau_0 = 5$, $\Delta T = 50000K/\eta$, where $\eta = 1, 4, 16$ for 100 MHz, 400 MHz, 1600 MHz, respectively.

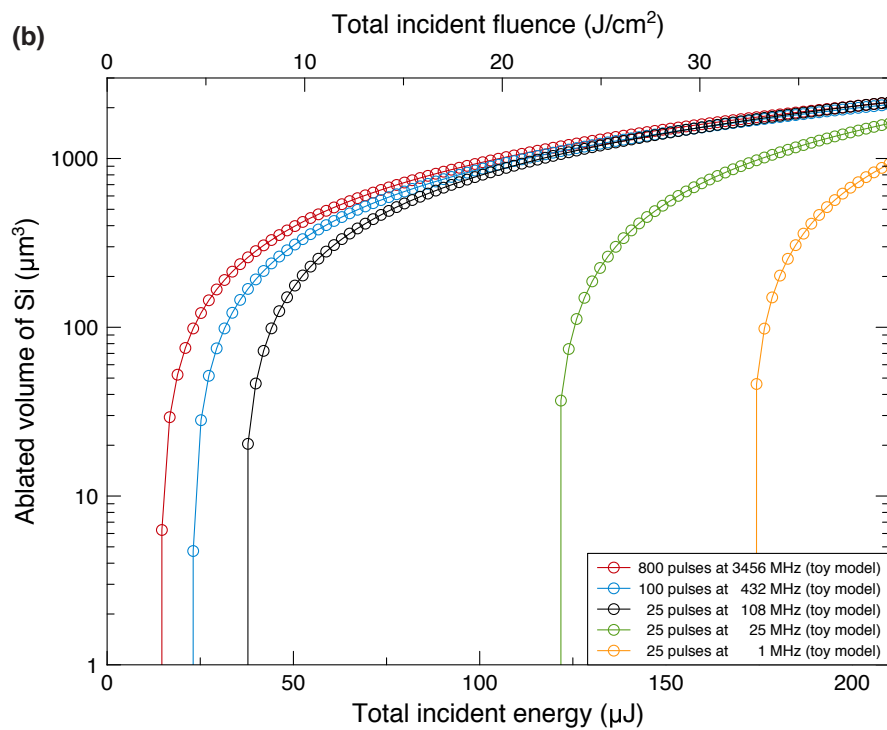
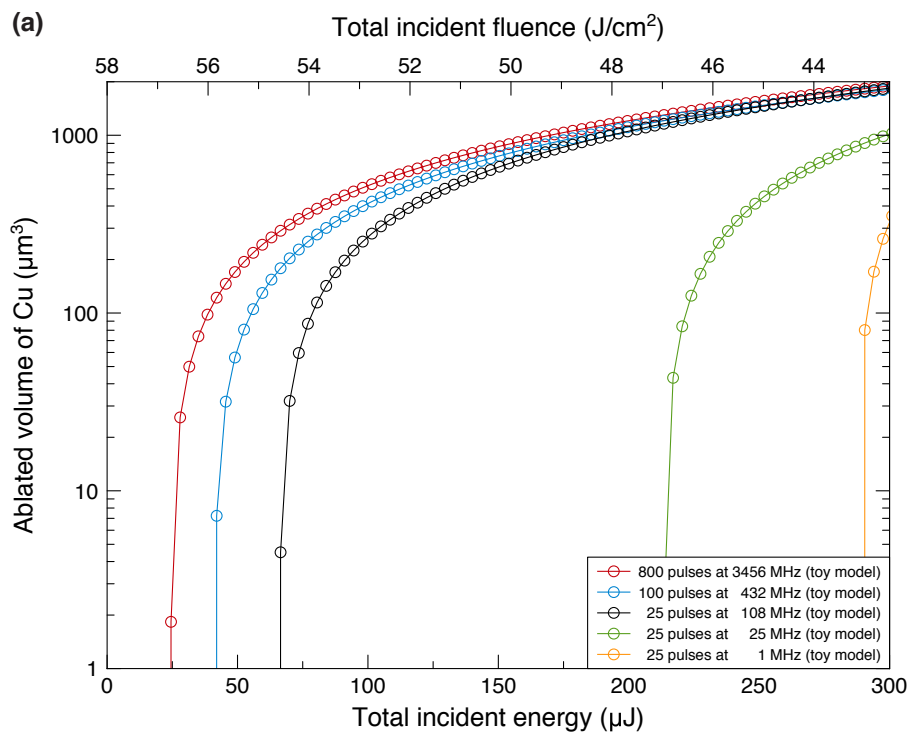


Figure 2.5: Predictions of toy model with the calculations for 1 MHz, 25 MHz, 108 MHz, 432 MHz and 3456 MHz.

2.2 Numerical Simulations Based on Single Temperature Model

In order to show the qualitative nature of this process and to validate the predictions of our Toy Model, laser-material interaction was modelled by a parabolic one-step radiation model [45], assuming constant thermo-physical and optical properties. Moreover, the ratio of laser spot size to optical penetration depth was kept in the order of 100. In this limit, a one-dimensional model could be used to simulate the physical phenomena, which reduces the computation time. Under these conditions, the energy equation can be written as:

$$\rho C_p \frac{\partial T}{\partial t} = k \frac{\partial^2 T}{\partial z^2} + S \quad (2.23)$$

where z is the direction perpendicular to the surface, ρ is the material density, C_p is the specific heat of the target material, k is the thermal conductivity, and S is the laser heating term defined as:

$$S = (1 - R)\alpha I_0 e^{-\alpha z} \quad (2.24)$$

where $(1 - R)$ is the surface transmissivity, α is the material absorption coefficient, I_0 is the laser intensity at the surface. In this simplified model, material ablation was modeled using critical point phase separation (CPPS) [46], meaning that material removal occurs instantly once the temperature of the material exceeds a separation temperature (T_c). Assuming the energy loss through the free surface of the material is much smaller compared to the thermal diffusion into the material, the thermal boundary condition on the surface of the material becomes no-heat flux. Considering the simulation domain is large enough, the thermal boundary condition at far deep of the material becomes constant, which is at room temperature T_0 . Finite difference method was implemented with central differencing in spatial direction and forward differencing in time to solve this model. The finite difference formula for an interior node can be written as:

$$T_i^{k+1} = T_i^k + \frac{D\Delta t}{(\Delta z)^2}(T_{i+1}^k - 2T_i^k + T_{i-1}^k) + \frac{S}{(\rho C_p)\Delta t} \quad (2.25)$$

where,

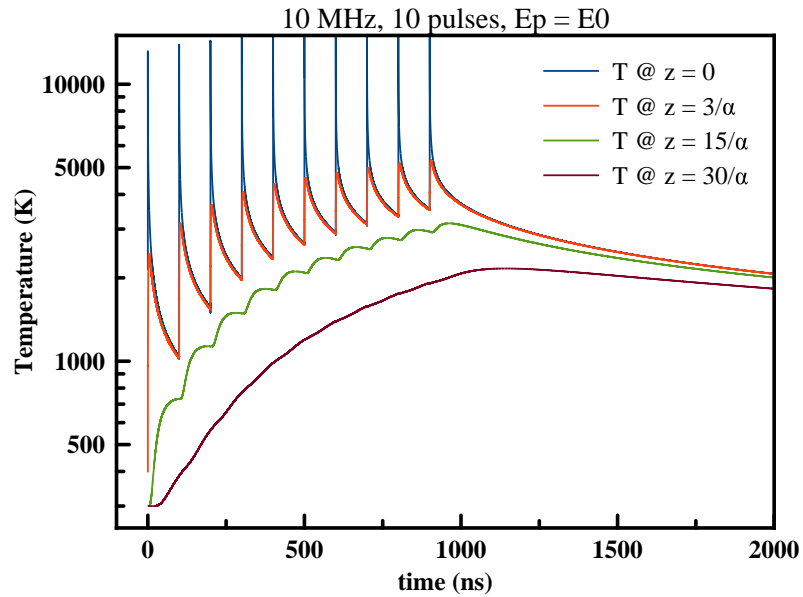
$$D = \frac{k}{\rho C_p} \quad (2.26)$$

is the thermal diffusivity, Δt is the time step and Δz is the grid spacing. Superscript k and subscript i denote time and space, respectively. To model CPPS, the ablated nodes were removed from the computational domain, and the origin was moved from zero to a new ablated depth. The no-flux thermal boundary condition was also specified on the new surface. The simulation parameters were defined as:

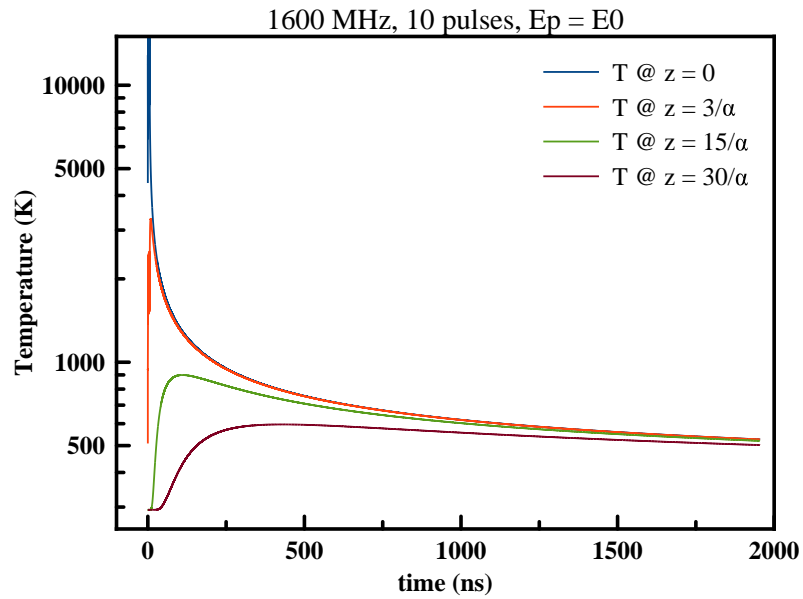
- $D = 1.15E - 4 \left(m^2/s \right)$
- $\alpha I_0 = 0.2 \left(MW/\mu m^2 \right)$
- $\rho C_p = 1.3 \left(MJ/m^3 K \right)$
- *spatial simulation domain* = $330/\alpha$
- $T_c/T_0 = 50$
- $(1 - R) = 0.75$
- $1/(\alpha^2 D) = 1 \text{ (ns)}$
- $\tau_0 = 1/(\alpha^2 D)$
- $\tau_{pulse} = t_{pulse}/(\alpha^2 D) = 1E - 3$

The simulation domain was divided into 20000 nodes. Two sets of simulations were performed with pulse-to-pulse where, the numerical parameters correspond to the case of silicon.

Numerical simulations on parabolic one-step radiation model confirm "Toy Model"s two main predictions: (i) Heating of surrounding regions is significantly reduced when the repetition rate is increased for constant pulse energy (Fig. 2.6 and 2.7). (ii) Increasing the repetition rate and the number of pulses within the burst allows decreasing of the pulse energy without reduction in amount of ablation (Fig. 2.8).



(a) Temperature rise due to application of 10 laser pulses at 10 MHz



(b) Temperature rise due to application of 10 laser pulses at 1600 MHz

Figure 2.6: Surface and sub-surface heating during ablation with (a) laser pulses at low repetition rate and (b) laser pulses at high repetition rate. Please note that per pulse energies, so, the total delivered energy, are exactly the same

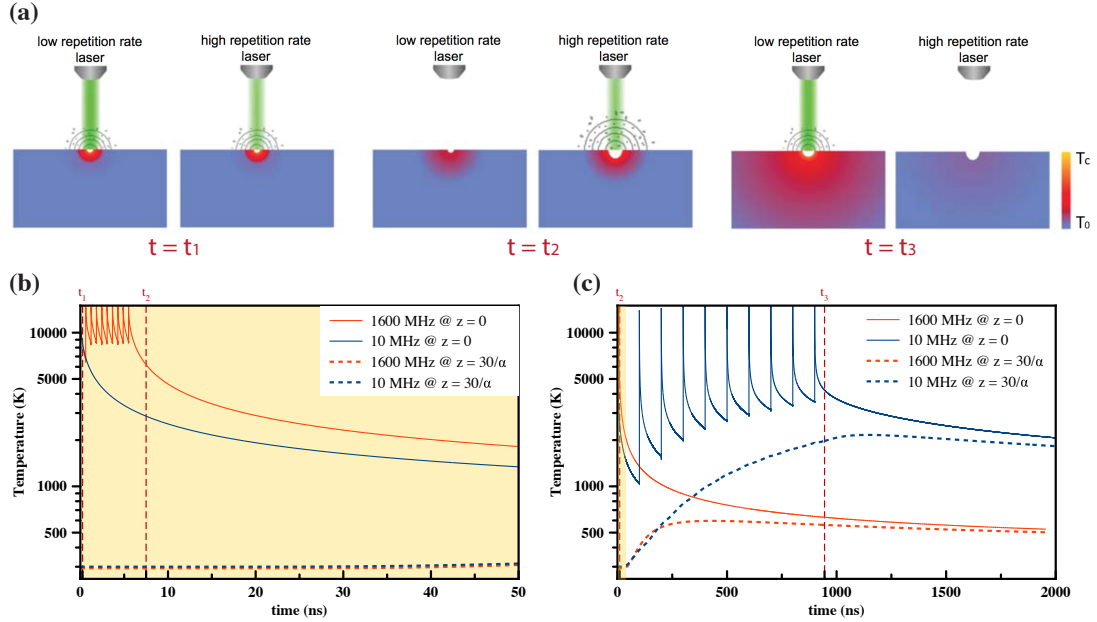


Figure 2.7: (a) Schematic representation of the ablation process for low (negligible ablation cooling) and high (significant ablation cooling) repetition rates, respectively: Temperature profiles are illustrated (left) for $t = t_1$, which is shortly after the arrival of the first pulse for both cases; (middle) for $t = t_2$, which is shortly after (before) the arrival of the last (second) pulse for the high-repetition-rate (low-repetition-rate) laser; (right) for $t = t_3$, which is shortly after the arrival of the last pulse for the low-repetition-rate laser. The colouration of the target material is based on simulation results shown in (b), according to the colour bar indicated therein and at the indicated time intervals of $t = t_1$, $t = t_2$, and $t = t_3$. (b) Calculated evolution of the temperatures at the surface (solid lines) and below (at a depth of 30 times the optical penetration depth) the surface (dotted lines) for repetition rates of 10 MHz (black lines) and 1600 MHz (blue lines). The pulse energies and number of pulses are the same for both cases. The higher repetition rate results in significantly lower temperatures below the surface due to ablation cooling. (c) Expanded view of the shaded section of the plot in (b)

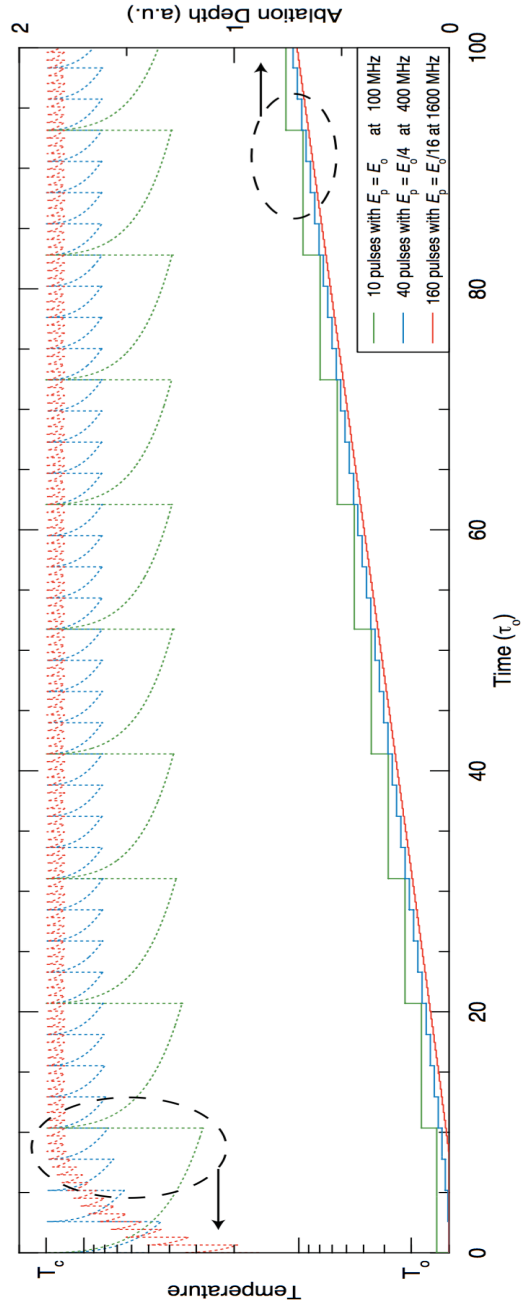


Figure 2.8: Calculated evolution of the surface temperature (dashed lines) and amount of ablated material (solid lines) for repetition rates of 100 MHz (green lines), 400 MHz (blue lines) and 1600 MHz (red lines). The ablation rate remains approximately the same when the product of pulse energy and repetition rate is maintained. The spikes in surface temperatures precisely indicate the arrival of pulses, which are not shown explicitly for clarity.

2.3 Numerical Simulations Based on Two Temperature Model

While the single-temperature model is highly effective its clarity and ease of qualitative interpretation, it is well known that interaction of ultrashort pulses with matter is not accurately modeled due to the far-from-equilibrium thermodynamic conditions created. A much more accurate description is provided by the so-called Two Temperature Model (TTM) [39,45]. This parabolic two-step radiation model is extensively used to model ultrashort pulse-material interactions. Since the basic principles of ablation cooling rely on the non-equilibrium conditions being maintained between subsequent pulses (namely, the differences arising from dynamics typically on a time scale of >100 ps), we did not expect to observe any qualitative differences as a result of using the TTM. The ratio of laser spot size to optical penetration depth was kept in the order of 100. In this limit, a one-dimensional model can be used to simulate the physical phenomena, which reduces the computation time substantially. Under these conditions, the governing equations for TTM model can be written as [45]:

$$C_e \frac{\partial T_e}{\partial t} = \frac{\partial}{\partial z} \left(k_e \frac{\partial T_e}{\partial z} \right) - G(T_e - T_L) + S \quad (2.27)$$

$$C_L \frac{\partial T_L}{\partial t} = G(T_e - T_L) \quad (2.28)$$

where T_e is the electron temperature, T_L is the lattice temperature, z is the direction perpendicular to the surface, ρ is the material density, C_e is the specific heat capacity of the electrons, C_L is the specific heat capacity of the lattice, k_e is the thermal conductivity of the electrons, G is the electron-phonon coupling parameter, and S is the laser heating term defined as:

$$S = (1 - R)\alpha I_0 e^{-\alpha z} \quad (2.29)$$

where $(1 - R)$ is the surface transmissivity, α is the material absorption coefficient, and I_0 is the laser intensity at the surface.

Various implementations of TTM have been considered before with varying

levels of complexity. One relatively simple approach is to model material ablation using critical point phase separation (CPPS) [46], meaning that material removal occurs instantly once the temperature of the material exceeds a separation temperature (T_{sep}). Assuming the energy loss through the free surface of the material due to convection is much smaller compared to the thermal diffusion into the material and loss due to ablation, the thermal boundary condition on the surface of the material becomes no-heat flux. Considering the simulation domain is large enough, the thermal boundary condition at far deep of the material becomes constant, which is at room temperature T_0 . Strictly speaking, the thermo-physical properties C_e , C_L and k_e have functional dependence on temperature. Moreover, the electron-phonon coupling parameter (G), surface transmissivity ($1 - R$), and the material absorption coefficient (α) are also functions of temperature [39, 47–49]. T_{sep} can be expressed as $T_{critical}(\rho_0/\rho_{critical})^{2/3}$ [39]. In order to predict the amount of ablated material quantitatively, a reliable data for all the aforementioned parameters as a function of temperature is required for a given metal. Unfortunately, this has proven to be quite difficult, as most references do not provide a complete set of parameters assumed. In particular, we were unable to set such a set for Cu. Since the main objective of the present study is to prove the principle of ablation cooling, we have based on the TTM on the commonly used approximations for nickel, for which reliable and consistent set of parameters could be found. Here, the thermo-physical parameters are approximated as [45]:

$$C_e = \gamma T_e \tag{2.30}$$

$$k_e = k_{e0} \frac{T_e}{T_L} \tag{2.31}$$

where γ is a constant with the unit of $\text{J}/\text{m}^3\text{K}^2$ and k_{e0} is the electron thermal conductivity at room temperature. C_L , G , $(1 - R)$ and α were taken as constant. Due to the large variance of the data for $T_{critical}$, ρ_0 and $\rho_{critical}$ [50], T_{sep} was taken as 15000 K.

Finite difference method was implemented with central differencing in spatial direction and forward differencing in time to solve this model. The finite difference

formula for an interior node can be written as:

$$T_{e,i}^{k+1} = T_{e,i}^k + \frac{\Delta t}{\gamma T_{e,i}^k} \left[\frac{k_{e,i+1/2}^k}{(\Delta z)^2} (T_{e,i+1}^k - T_{e,i}^k) - \frac{k_{e,i-1/2}^k}{(\Delta z)^2} (T_{e,i}^k - T_{e,i-1}^k) - G(T_{e,i+1}^k - T_{L,i}^k) + S \right] \quad (2.32)$$

$$T_{L,i}^{k+1} = T_{L,i}^k + G(T_{e,i}^k - T_{L,i}^k) \quad (2.33)$$

where Δt is the time step and Δz is the grid spacing. Superscript k and subscript i denote time and space, respectively. The electron thermal conductivity is expressed at the mid-point of the nodes as:

$$k_{e,i+1/2}^k = \frac{k_{e0}}{2} \left(\frac{T_{e,i+1}^k}{T_{L,i+1}^k} + \frac{T_{e,i}^k}{T_{L,i}^k} \right) \quad (2.34)$$

$$k_{e,i-1/2}^k = \frac{k_{e0}}{2} \left(\frac{T_{e,i}^k}{T_{L,i}^k} + \frac{T_{e,i-1}^k}{T_{L,i-1}^k} \right) \quad (2.35)$$

To model CPPS, the ablated nodes were removed from the computational domain, and the origin was moved from zero to a new ablated depth. The no-flux thermal boundary condition was also specified on the new surface. The simulation parameters were defined as [48]:

- $\gamma = 1065 J/m^3 K^2$
- $\alpha = 6.277 \times 10^7 1/m$
- $I_o = 0.2 MW/\mu m^2$
- $C_L = 3.68 \times 10^6 J/m^3 K$
- $k_{eo} = 91 W/mK$
- $T_o = 300 K$

- $R = 0.73$
- $t_{pulse} = 1ps$
- $G = 3.6 \times 10^{17}W/m^3K$

The simulation domain was divided into 20000 nodes. The time step was set to $t_{pulse} / 200$. Here, two sets of simulations is presented corresponding to the same physics as explained in previous section, but for the case of Ni and using real units.

The first set of simulations is intended to demonstrate the reduced heating surrounding regions in the case of ablation cooling. To this end, ablation was contrasted with 10 MHz and 1.6 GHz repetition rates with same pulse energy, corresponding to case of negligible and strong ablation cooling, respectively. The same conditions are simulated both using the single-temperature model (STM) and the TTM for comparison. For STM, the simulation parameters are given as:

- $\alpha = 6.277 \times 10^7 1/m$
- $I_o = 0.023MW/\mu m^2$
- $\rho \times C_p = 4 \times 10^6 J/m^3K$
- $k = 91W/mK$
- $R = 0.73$
- $t_{pulse} = 1ps$

It is seen clearly from the evolution of the temperature at the surface that in the case of 1.6 GHz repetition rate pulses, there is not enough time between the pulses for the surface to cool down. In fact, both the STM and TTM predict approximately an order of magnitude higher minimum surface temperature for 1.6 GHz pulses compared to 10 MHz pulses (Fig. 2.9). The use of 10 MHz pulses also results in significantly higher temperature below the surface compared to 1.6

GHz; e.g., 5 μm below the surface, 10 MHz pulses result in 200 K higher maximum temperature than 1.6 GHz. Under the same conditions, TTM qualitatively predicts the same outcome; quantitatively, the predicted maximum temperature is 300 K higher for 10 MHz than for 1.6 GHz (Fig. 2.10). These results are consistent with the main predictions of the toy model.

The second set of simulations is intended to demonstrate the scaling of the individual pulse energy with repetition rate and number of pulses. We contrast ablation of Ni using total of 10 pulses at 100 MHz repetition rate, 40 pulses at 400 MHz repetition rate and 160 pulses at 1.6 GHz repetition rate using STM (Fig. 2.11) and TTM (Fig. 2.12). The pulse energies are correspondingly scaled down; going from 100 MHz to 400 MHz, the pulse energy is reduced by a factor of 4 and similarly, going from 400 MHz to 1.6 GHz, the pulse energy is again reduced by a factor of 4. Therefore, in all three cases, the total energy delivered at a given point in time, e.g., after 100 ns, is the same. Comparing the results, we see that the surface temperatures cools down more for lower repetition rates, but this is made up for by the higher pulse energy of the next pulse coming in. Overall, the average minimum surface temperature is reduces substantially going from 1.6 GHz to 400 MHz and to 100 MHz, also as expected.

Furthermore, the total amount of material ablation is to first order the same during the scaling up of the repetition rate with simultaneous reduction of individual pulse energies and in fact, in this case, it is even higher by a factor of ~ 2 for 400 MHz than for 100 MHz and also higher by a factor of ~ 2 for 1.6 GHz than for 400 MHz. This conclusion depends on the material and pulse parameters and the more general conclusion is that the ablation efficiency is approximately constant under this scaling.

While the TTM results presented here would vary quantitatively according to various formulations of the TTM in the literature or if the assumed parameters were changed. However, the principle advantages of ablation cooling appear to be robust and in agreement with the simpler approaches of the STM, the basic predictions of the analytic model and most importantly, the experimental results.

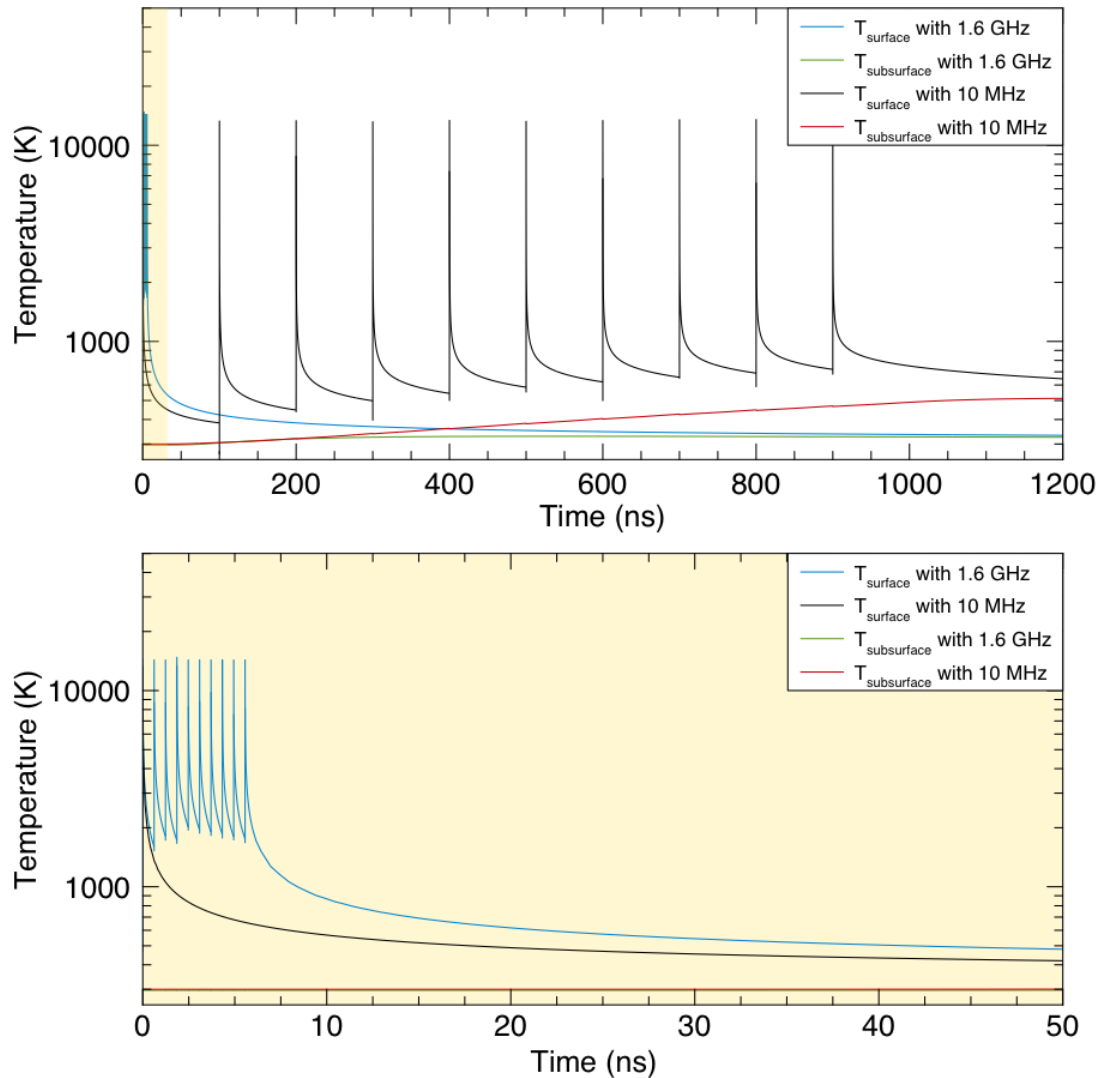


Figure 2.9: Simulations showing the effect of ablation cooling for Ni based on STM: Calculated evolution of the surface temperature, and $5 \mu\text{m}$ below the surface, for repetition rates of 10 MHz and 1600 MHz. The results are qualitatively similar to the results of the STM shown above. The spikes in surface temperatures precisely indicate the arrival of pulses, which are not shown explicitly for clarity. The results are qualitatively similar to the results of the TTM shown below.

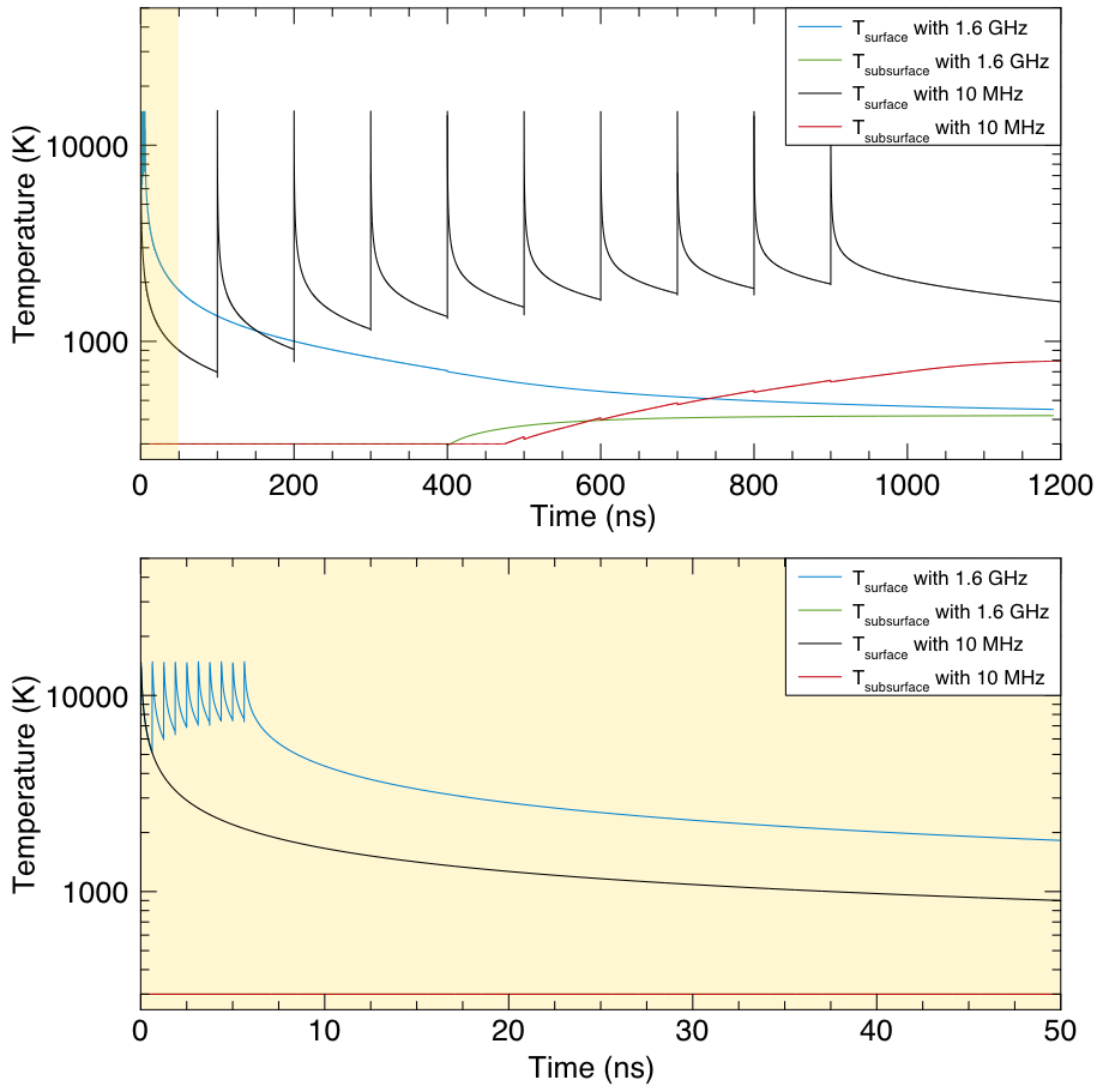


Figure 2.10: Simulations showing the effect of ablation cooling for Ni based on TTM: Calculated evolution of the surface temperature, and 5 μm below the surface, for repetition rates of 10 MHz and 1600 MHz. The results are qualitatively similar to the results of the STM shown above.

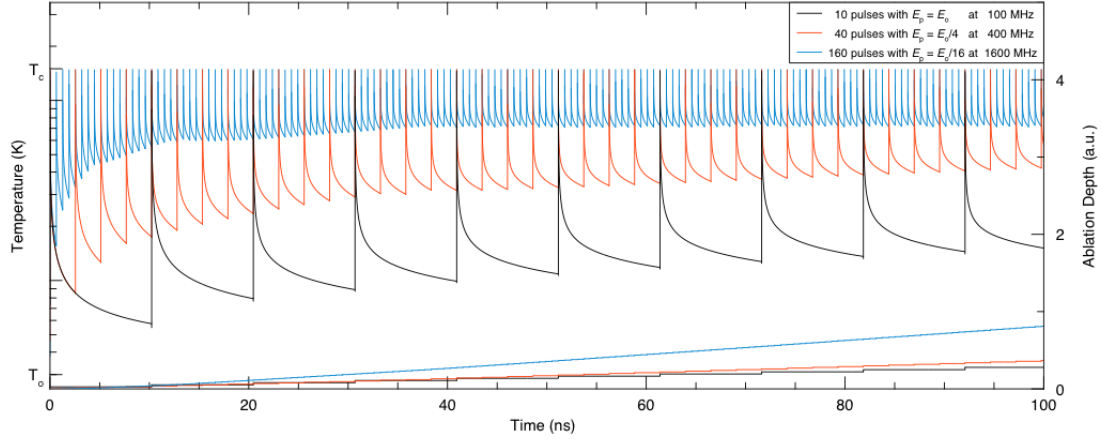


Figure 2.11: Simulations for Ni based on STM: Calculated evolution of the surface temperature (dashed lines) and amount of ablated material (solid lines) for repetition rates of 100 MHz (green lines), 400 MHz (blue lines) and 1600 MHz (red lines). The ablation rate slightly increases when the product of pulse energy and repetition rate is maintained. The predictions are in excellent qualitative agreement with those of the TTM shown below.

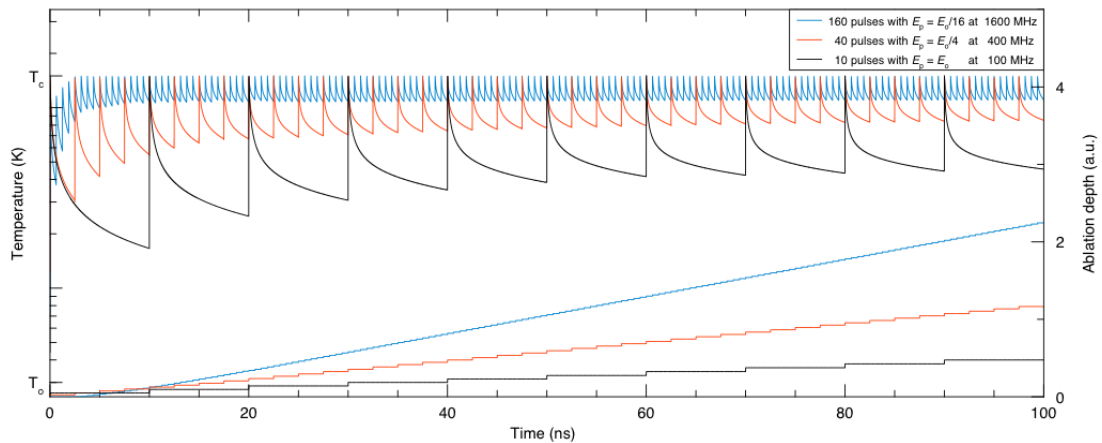


Figure 2.12: Simulations for Ni based on TTM: Calculated evolution of the surface temperature (dashed lines) and amount of ablated material (solid lines) for repetition rates of 100 MHz (green lines), 400 MHz (blue lines) and 1600 MHz (red lines). The ablation rate slightly increases when the product of pulse energy and repetition rate is maintained. The predictions are in excellent qualitative agreement with those of the STM shown above.

Chapter 3

EVIDENCE of ABLATION COOLING

In order to provide a direct proof of the ablation cooling effect, an experimental setup was designed to measure the temperature of a target material and of the ablated particles, simultaneously. Measuring the temperature from a local point mostly rely on measurement methods that are sensitive to change in the property of material due to heating. For contact measurements, thermocouples and thermistors are commonly used. They are available with diameters as small as tens of micrometers, thus can be utilized to measure temperature from a very small area. Measurement of highly localized temperature from much smaller spots is also possible with lasers and mostly based on a method called thermo-reflectance [51–54].

In order to discriminate and comment on the effect of ablation cooling between highly repetitive laser pulses applied as bursts and uniformly separated laser pulses applied at lower repetition rates (Fig. 2.6 and Fig. 2.7.c.), temperature should be measured locally by placing thermocouples exactly at a same distance below the surface for each operating mode. In addition to the technically difficult placement and targeting accuracy, application of the same amount of thermal paste onto both thermocouples may cause variations in the measurements. Although thermo-reflectance based temperature measurement with lasers

give very precise and accurate results exactly from the region of interest, in the case of material ablation, it cannot be used directly to measure temperature at the surface because of plasma. It is also hard to measure the temperature below surface by thermo-reflectance because of accuracy and the need for a smart triggering system. A simple way to surpass these limitations is to directly ablate the thermocouple itself.

Thermoelectric modules are commonly used to cool down or heat up the material that they are attached, due to Peltier effect, which is basically conversion of applied current to heat. The opposite effect is on the other hand called Seebeck effect where the heat is converted directly into electricity. As the laser ablates the thermoelectric module, the temperature is thus can be measured as voltage. Here, successful use of ablating a target material is being reported, which exhibits strong Seebeck effect. To a reasonably good approximation, thermoelectric voltage difference is linearly proportional to the induced temperature. Furthermore, the purpose of the following experiments is to establish the role of the ablation cooling effect and the conclusion drawn are robust against small deviations from linear response of the thermoelectric modules.

The setup is described in Fig. 3.1.a. , where a picture of the setup is presented in Fig. 3.1.b. The laser beam is focused onto the surface of a thermoelectric module, and is used to ablate it. As a result of the residual heating, a temperature difference is formed between the laser-targeted top surface and the bottom surface, which leads to a measurable voltage difference. Two identical 4 cm \times 4 cm thermoelectric modules (TEC1-12706, Thermonamic, Jiangxi, China) were used during the experiments. The one was used as the substrate and the other one was attached to a microscope coverslip. As the ejected material is being removed from the surface, they attach to the coverslip and heat it up, thus causing a voltage difference on second module too. The modules were connected to two channels of an audio analyzer (UPV Audio Analyzer, Rohde and Schwarz DC-250 kHz, Munich, Germany) to measure voltage changes during processing. The substrate thermoelectric module was illuminated and raster scanned by 800 fs pulses from a custom built burst mode laser system [55, 56], with a modified oscillator that is capable of producing seed signal up to 3.46 GHz as it is explained in Appendix

A.1. Effects of two operating modes on heating were compared:

- Burst Mode with ablation cooling: 1.73 GHz intra-burst repetition rate, 50 pulsed burst (30 ns burst duration) with 200 kHz burst repetition rate, 3 μJ /pulse energy constituting 30 W P_{avg} .
- Uniform Mode with negligible ablation cooling: 10 MHz, uniformly separated pulses with 3 μJ /pulse energy constituting 30 W P_{avg} .

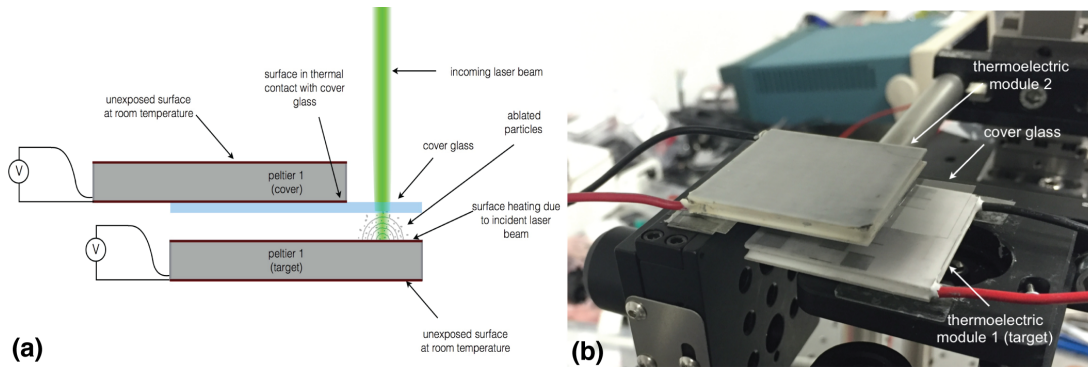


Figure 3.1: Experimental setup and temperature measurement to evidence ablation cooling. (a) Thermoelectric module placement and direction of laser illumination. (b) Picture of the actual setup.

The reason for using a laser with higher average power than used throughout the rest of this thesis was the intention to create conditions for heating of the bulk of the target even in ablation mode, so that temperature changes could be measured. Otherwise, given the small volume of the target being processed by the laser and only the average temperature of the substrate was measured, maintaining the accuracy measurement becomes extremely challenging. 5 mm x 5 mm square regions were scanned only once for each mode with a line separation of 12.5 μm , where, the spot diameter was measured to be 26 μm . In order to apply exactly the same number of bursts, *i.e.* pulses onto a single spot (50 % overlapping bursts - approximately 100 pulses/spot), scan speed was adjusted to be 2 m/s. Having done so, the total processing time was calculated to be 1.2 s. In all comparisons, two identical regions adjacent to each other and symmetrically positioned with respect to the thermoelectric modules were processed, one with

the burst mode and another with the uniform, in order to make the comparison as fair and as accurate as possible.

The results of the experiments are presented in Fig. 3.2.a. These show, unambiguously, that the target material heats less and the coverslip heats more when 1.7 GHz repetition rate pulses are used, as opposed to 10 MHz pulses, even though all other parameters are kept as constant as possible. These include average power and processing time, which means that the total energy delivered is exactly the same in both cases. Therefore, a straightforward argument based on energy conservation illustrates that the reduction in temperature rise for the target material and the corresponding increase in temperature of the coverslip is explained by the increased amount of energy being carried away in the form of ablated particles. Several facts need to be checked to ensure the accuracy of the measurements and validity of the conclusions drawn above. All the experiments were repeated several times to ensure that variations in the measured results obtained under nominally identical conditions were negligible. Similar experiments were repeated without the presence of the coverslip above and it was always found that the burst mode resulted in lower target temperatures, which is the expected result of the ablation cooling mechanism. This verification experiments show that the temperature measurements of the targets are not affected by the presence of the coverslip (Fig. 3.2.b.).

Fig. 3.2 reveals that substrate heating is lower with laser applied in burst mode than uniformly repeated pulses at 170 times lower repetition rate. On the other hand, coverslip temperature is higher in burst mode since more energy is carried away from the surface as compared to uniform mode. In other words, application of bursts including highly repetitive pulses creates an ablation cooling regime and the substrate remains colder. The result here is also in agreement with numerical simulation results as depicted in Fig. 2.7.b and c.

Another factor that must be ruled out is whether the accumulation of accumulated particles on the coverslip increases linear absorption of the incoming laser light, which can lead to artificially higher temperature on the coverslip during burst-mode processing (which leads to more material being ablated). However,

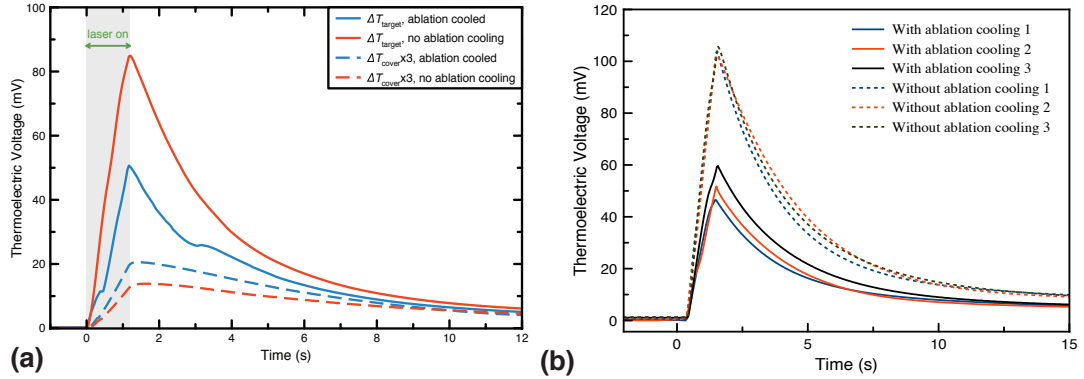


Figure 3.2: Measured thermoelectric voltages induced on Thermoelectric Modules. (a) Measured thermoelectric voltages induced on Thermoelectric Module 1 (target material, solid lines) and the Thermoelectric Module 2 (attached to the coverslip that collects some of the ablated particles, dashed lines) for laser processing with significant ablation cooling (blue lines) and with negligible ablation cooling (red lines). (b) Measurements of thermoelectric voltage induced due to temperature rise in the target material during laser processing with and without ablation cooling, implemented with burst and uniform modes, respectively. The results consistently show that the target material heats substantially less with ablation cooling than without ablation cooling, even though the total laser energy incident is the same.

this was ruled out in a straightforward manner by measuring the change in linear absorption of the coverslips after processing. The linear absorption was found not to increase more than 1%, from which one can rule out this effect. Furthermore, the experiment was repeated with the target thermoelectric module removed, such that the laser light passes through the pre-exposed and partially debris-covered coverslip (Fig. 3.3). Measurements were made on a fresh sample (black trace) and samples, which have been partially covered with ablated material using the burst mode (blue trace) and the uniform mode (red trace). The results are virtually identical, which proves that heating of the coverslip due to linear absorption is negligible in all of these experiments.

Based on this set of experiments, we have verified the validity of our three major conclusions that provide direct evidence of ablation cooling: (i) The bulk of the target material heats less and (ii) more heat energy is carried away from the target material, when using high repetition rate pulses provided by the burst mode of operation, than lower repetition rate pulses provided by the uniform mode of

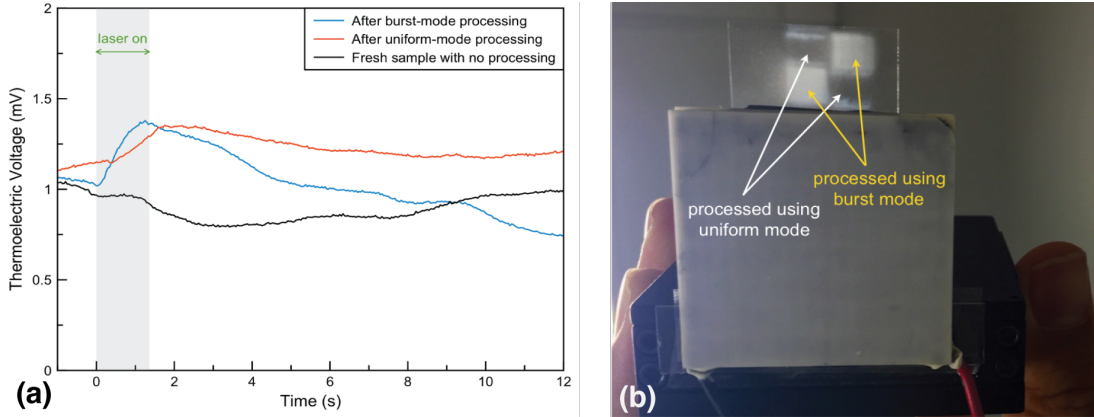


Figure 3.3: Transparency test. (a) Measurements of temperature in thermoelectric module 2 (connected to coverslip), when the same laser processing procedure is applied without a target material below. Any heating is due to absorption of the laser beam by the coverslip. Measurements made on a fresh sample (black trace) and samples which have been partially covered with ablated material using the burst mode (blue trace) and the uniform mode (red trace) are virtually identical. (b) Picture of coverslip, which was processed using burst mode and uniform mode, shows the vast difference in deposited material and consequently the difference in ablation efficiency.

operation. (iii) Burst mode operation, exploiting ablation cooling, results in much higher material ablation than uniform mode, even though the total number of pulses delivered and the energy and pulse duration of the individual pulses are identical. This is also seen by the difference in the coated material on the coverslips (Fig. 3.3.b).

Lastly, in order to check the influence of linear absorption of the material does not alter this picture in any significant way, the substrate module was painted with black board-marker and same steps were followed as mentioned above. The thermoelectric module surfaces are quite smooth and white, resulting in substantial portion of the incident light being reflected and scattered. Naturally, the use of ultrafast pulses largely eliminates dependency on linear absorption characteristics of a target material, but a simple verification was deemed feasible. The amount of ablated material is much higher, once again, for the burst mode than the uniform mode, even though the same total number of pulses has been delivered and the individual pulses have identical width and energies (Fig.

3.4.a.). The measured temperature rise follows the expected behavior, namely, burst mode results in significantly less heating of the bulk compared to uniform mode (Fig. 3.4.b.). Shortly, the application of burst mode removed all the paint, whereas, caused less heating on substrate. On the other hand, uniform mode left some paint on the target and also heated the substrate more.

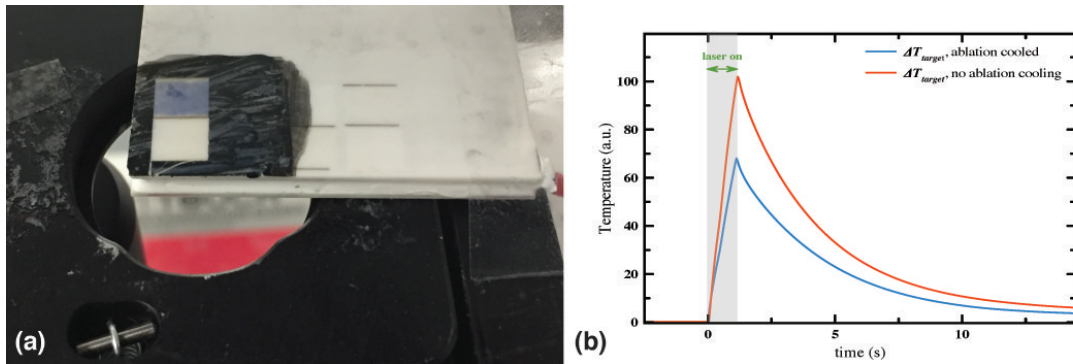


Figure 3.4: Burst and uniform mode application on black painted thermoelectric module. (a) Image of painted thermoelectric module after processing. Some paint remains after application of uniform mode whereas, burst mode removes all the paint (clear zone). (b) Temporal evolution of thermoelectric voltage change of the painted substrate with and without ablation cooling, implemented with burst (blue line) and uniform (red line) modes, respectively.

Chapter 4

COPPER, SILICON and PZT CERAMIC PROCESSING

For experiments on copper and silicon samples, an in-house developed Yb-doped fibre burst mode laser amplifier system was used, where the system has an adjustable in-burst repetition rate, starting from 108 MHz and can be increased by factor of 2, to 216 MHz, 432 MHz, 864 MHz, 1728 MHz and 3456 MHz. The system is optimized for high burst energies and low burst repetition rate. The all-fibre amplifier system is seeded by an all-normal dispersion laser oscillator, which generates a mode-locked signal at a repetition rate of 108 MHz as the seed source. The signal from the oscillator is passed through the cascaded repetition rate multiplier before seeding six stages of core-pumped fibre pre-amplifiers, a three-stage double clad (DC) fiber power amplifier, supported by synchronized pulse picking and pulsed-pumping electronics. The system details can be found in Appendix A.1.

The PZT experiments were conducted with the same system (see Appendix A.3) that was utilized in hard tissue experiments.

4.1 Cu and Si Ablation Efficiency Experiments

Polished Cu and single side polished Si samples were placed onto an extension holder, which includes screws to adjust the surface tilt and attached to a 3D manual stage with 10 mm movement capability in each direction and 10 μm resolution. The scan pattern was programmed with SamLight software (SCAPS GmbH, Deisenhofen, Germany). The patterns consisted of raster scans for each energy level covering a region of 250 μm by 250 μm , constituting of 50 ablation spots, which were repeated 20 times for each particular repetition rate and number of pulses in the study to ensure proper statistics. A simple schematic of the scan pattern is illustrated in Fig.4.1. All measured ablation values correspond to averages of the obtained results to reduce variation. Standard deviations are indicated as error bars in Fig.4.2. Only scans for one particular repetition rate were made for each sample. The scan speed was adjusted (33 mm/s) in order to have single burst shot per spot and the centre of each spot is separated by 33 μm , which ensures that there is no overlapping even with large crater diameters obtained at high energies. Each burst consisted of particular number of pulses. Movement of the spot during each burst is absolutely negligible compared to the spot size (about 8 nm during each burst), so all pulses within each burst are effectively incident at the same spot.

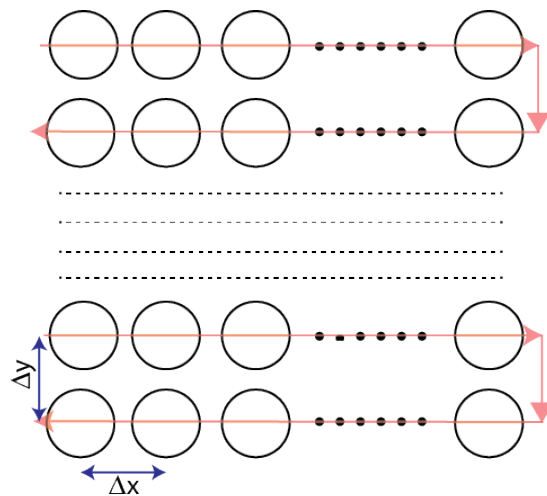


Figure 4.1: Raster scan pattern

Prior to ablation, surfaces of 5 mm thick Cu samples with 2.5 cm diameter

were grinded and polished. The grinding was performed on a rotating platform. During the grinding process, few drops of water were poured on the grinding paper a few times. The rotation speed was gradually decreased and the direction of rotation was altered. Then, the grinding paper was switched with a finer one. The last grinding operation was performed with grinding paper of ISO/FEPA grit designation of p2000 and the first one with p240. The rest were between these two extremes. After grinding operation, the samples were then transferred to polishing platform. During first polishing, 6- μ m diamond solution was sprayed on polishing cloth and the platform was rotated at 150, 100 and 50 rpm both counter clockwise and clockwise. Then, another polishing cloth was inserted and 1- μ m diamond solution was sprayed and the same polishing operation was repeated. Then, the samples were rinsed under water and dried out with pressured air. The Si samples were already single side polished with 500- μ m thickness. After polishing the Cu samples had optical surface quality with roughness in the \sim 30 nm range.

The sample to be ablated was placed on the holder and the tilt was adjusted with a compass in order to have the same tilt with the galvo scanner head (Scan-cube14, Scanlab AG, Munich, Germany). The beam incoming to the scanner head was expanded in order to fill 14 mm aperture. The beam is then focused with an f-theta lens with 5 cm focal distance, which was attached to the scanner. To drive the scanner, a SCAPS USC 1 board was used, which is controlled with SAMLight software (SCAPS GmbH, Deisenhofen, Germany). For each repetition rate and number of pulses in burst, amplified spontaneous emission rate (ASE) was measured in order to obtain the net amount of power available for processing. The loss due to mirrors, beam expander and the galvo scanner on material processing part was calculated as 85 %. The spot diameter was estimated to be 26 μ m by looking at the crater diameters, using both the traditional knife-edge method and a modern beam profiler (BP209-IR, Thorlabs, Inc, Newton, NJ, USA). Just before patterned ablation, the laser system was set to 25 pulsed-burst operation and the sample was moved in z-axis in order to estimate the focal distance. The energy was then reduced gradually with the half wave plate (HWP) before the

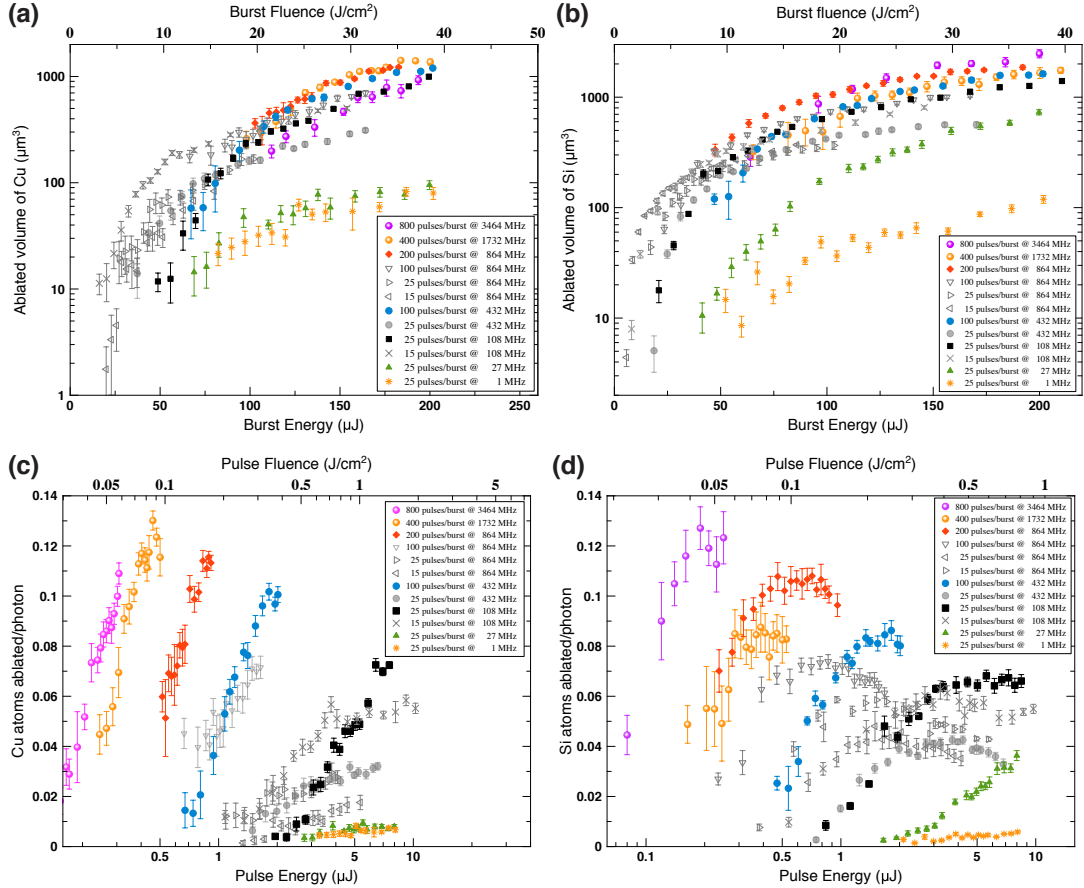


Figure 4.2: Scaling down of pulse energy with increasing repetition rate. Volume of (a) Cu and (b) Si ablated by a single burst of pulses as a function of burst energy and burst fluence for different intra-burst repetition rates. Ablation efficiency in terms of number of atoms of (c) Cu and (d) Si ablated per incident photon as a function of pulse energy and pulse fluence for different repetition rates. Full symbols highlight inverse scaling of pulse energy with repetition rate.

grating compressor, while a dummy raster scan was ongoing, until a weakly illuminated plasma on the surface was observed. The z position on the stage was recorded and raster scans below and above this value were performed. The surfaces were also viewed under custom-built standard light microscope integrated to the processing system to estimate the exact position of the focal point.

After ablation, the surfaces were cleaned with acetone and optical tissue. The samples were analyzed and data stacks were obtained with a laser scanning microscope (VK-100x, Keyence Corp., Itasca, IL, USA) using a 50X objective. The

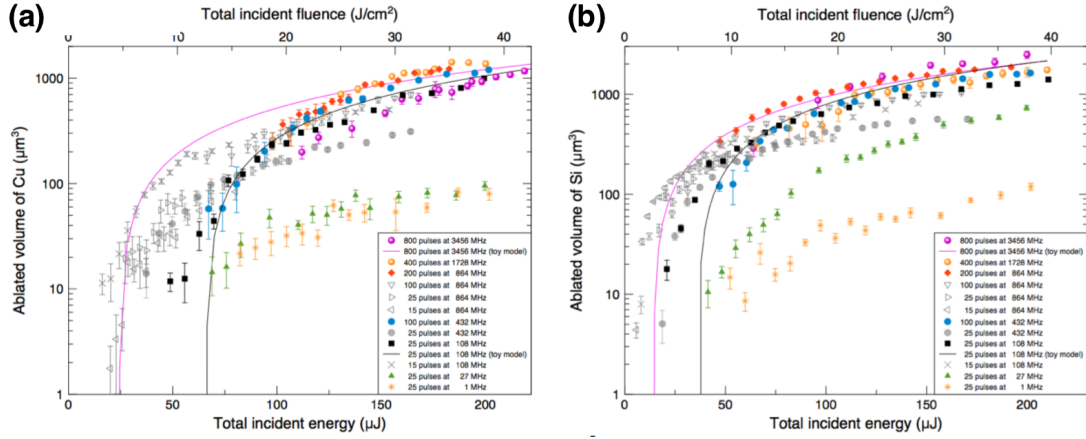


Figure 4.3: Scaling down of pulse energy with increasing repetition rate including the toy model. Volume of (a) Cu and (b) Si ablated by a single burst of pulses as a function of burst energy and burst fluence for different intra-burst repetition rates.

data was then analyzed with microscopes analysis software. For depth and width measurements, 10 spots were chosen and the average and the standard deviation were calculated. For volume data, averaging was done over 20 spots.

Total volumes of material ablated by a single burst as a function of burst energy are shown in Fig. 4.2.a for Cu and Fig. 4.2.b for Si. In terms of seeing the physics, it is more informative to look at Fig. 4.2.c and Fig. 4.2.d, depicting the absolute efficiency of the ablation process, namely number of atoms ablated per incident photon as a function of pulse energy. At low repetition rates of 1 MHz and 25 MHz, the results are similar. The benefits of ablation cooling become appreciable once the repetition rate is increased to 108 MHz. If the repetition rate is further increased, efficiency drops at high pulse energies. This is a consequence of the expected shielding effect. The solution is to decrease the pulse energy, increase the number of pulses in each burst and the intra-burst repetition rates, e.g., from 25 pulses per burst at 108 MHz to 100 pulses per burst at 432 MHz, and finally to 400 pulses (with 16 times lower energy) per burst at 1728 MHz, or, similarly to 800 pulses per burst at 3464 MHz with 32 times lower energy per pulse. With proper scaling down of the pulse energy, the higher repetition rates result in even slightly higher total ablation compared to the performance recorded at 108 MHz, indicating that the shielding effects are completely overcome. The

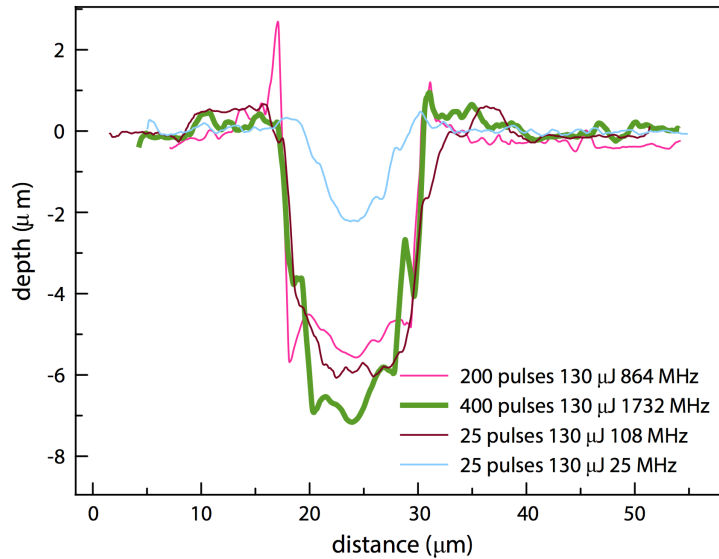


Figure 4.4: Representative crater depth profiles obtained at various repetition rate and pulse combinations after a single burst.

same scaling trend holds for both targets, even though Si and Cu have entirely different optical and physical characteristics, highlighting the universality of the ablation cooling effect. These results prove the prediction of decreasing pulse energy with increasing repetition rate (Fig. 2.8). In addition, Fig. 4.2. a. and b. is re-plotted including the toy model, where the details of the parameter set used in order to plot toy model results is explained in Appendix B.

The available literature on material processing has been combed through to provide comparison to previous publications for ultrafast ablation of Cu and Si targets. The results are presented in Table 4.1 and 4.2. It should be emphasized that many of the extracted parameters are not exact, since not all references provide the parameters with full clarity and in some cases, data had to be read off from figures. Therefore, the comparisons should be considered correct within an error margin. This level of uncertainty does not affect the main conclusions drawn, as the differences between the results of this work and the comparisons in literature are typically in the order-of-magnitude range.

Both from the basic physics and from an operational perspective, the main merit factor is the ablation efficiency, namely how much material is ablated given

pulse energy (or number of photons). From a physics perspective, the amount of material should correspond to the volume of material ablated when a crater is formed by the laser pulses, and ablated volume information has been used to plot Fig. 4.2. However, this is seldom reported in publications, instead depth of the crater is provided. Experimentally, however, both volumes and depths of the craters has been measured. For comparison to previous results, crater depth information was used in Table 4.1 and 4.2. Therefore, ablation efficiency is defined as depth of ablation caused by each pulse per incident pulse fluence, which has naturally also has units of volume per energy. These two definitions of ablation efficiency, based on volume and depth, respectively, are equivalent to each other within a geometric factor (order of 3), depending on the shape of the craters and this choice does not influence the conclusion to be drawn. Furthermore, exactly the same metrics have been compared, whenever a comparison is made.

In Table 4.1 and 4.2, the incident pulse energy and ablation efficiency are highlighted as parameters of direct importance with red colour. These results show that ablation cooling always achieves highest ablation efficiencies, even though the necessary pulse energies are orders of magnitude smaller. One should note that the differences are so great that the conclusions we draw are completely robust against factors of roughly 2 of uncertainty in ability to ascertain them from the referenced publications due to occasionally unclear usage of terminology, such as different definitions of spot size.

For a direct comparison, it is more instructive and physically meaningful to compare ablation efficiencies obtained with the ablation cooling approach to those obtained with isolated (or very low repetition rate pulses) at same pulse fluences. Most directly comparable values for Cu are highlighted with blue colour in Table 4.1. Comparison for Si is more difficult, since results presented here have been obtained at a wavelength of 1040 nm, whereas most of the comparisons in Table 4.2 are for 800 nm. Silicon is largely transparent at 1040 nm (absorption coefficient of 10 cm^{-1}), requiring nonlinear absorption to initiate ablation, whereas it is 100 times more strongly absorbing at 800 nm (absorption coefficient of 1000 cm^{-1}). Nevertheless, ablation efficiencies in the ablation-cooling regime are seemed to be

consistently higher by a significant margin. A more direct comparison is available with respect to a burst-mode laser [57]. Unfortunately, the spot size is not directly specified and while the ablated volume (and roughly, depth) per pulse can be ascertained from the available information, the ablation efficiency cannot be calculated.

(Intra-Burst) Repetition Rate	Wavelength (nm)	Number of pulses per burst	Burst Repetition Rate	Incident Pulse Energy (μJ)	Incident Burst Energy (μJ)	Pulse Duration (ps)	Spot Diameter (μm)	Pulse Fluence (J/cm^2)	Burst Fluence (J/cm^2)	Peak Intensity (TW/cm^2)	Ablation Rate (nm of depth per pulse)	Ablation Rate (μm of depth per burst)	Ablation efficiency	Reference
3456 MHz	1040	800	1 kHz	0.27	218	1	26	0.04	32	0.04	9.5	7.6	24	this work
3456 MHz	1040	800	1 kHz	0.27	193	1	26	0.04	29	0.04	8.5	6.8	24	this work
3456 MHz	1040	800	1 kHz	0.17	135	1	26	0.02	20	0.02	5.0	6.8	20	this work
1728 MHz	1040	400	1 kHz	0.5	198	1	26	0.07	29	0.07	17.5	7.0	24	this work
1728 MHz	1040	400	1 kHz	0.3	139	1	26	0.05	21	0.05	13	5.1	25	this work
864 MHz	1040	200	1 kHz	0.9	182	1	26	0.17	34	0.2	32.5	6.5	19	this work
432 MHz	1040	100	1 kHz	1.4	140	1	26	0.26	26	0.3	57	5.7	22	this work
108 MHz	1040	25	1 kHz	5.9	147	1	26	1.1	28	1.1	247	6.2	22	this work
670 kHz	1030	1	N/A	30	N/A	0.80	17	13	N/A	16.5	29	N/A	0.22	Ancona et al.
670 kHz	1030	1	N/A	50	N/A	0.80	17	22	N/A	27.5	50	N/A	0.23	Ancona et al.
670 kHz	1030	1	N/A	70	N/A	0.80	17	31	N/A	38.6	67	N/A	0.22	Ancona et al.
20 Hz	800	1	N/A	400	N/A	0.07	50	20	N/A	291	350	N/A	1.7	Hashed et al.
20 Hz	800	1	N/A	1.4	N/A	0.07	50	0.07	N/A	1.0	9	N/A	0.01	Hashed et al.
20 Hz	800	1	N/A	3.4	N/A	0.07	50	0.17	N/A	2.5	0.02	N/A	0.01	Hashed et al.
20 Hz	800	1	N/A	5.1	N/A	0.07	50	0.26	N/A	3.7	0.03	N/A	0.01	Hashed et al.
20 Hz	800	1	N/A	21	N/A	0.07	50	1.1	N/A	15.3	25	N/A	2.3	Hashed et al.
50 MHz	1064	5	100 kHz	3.0	15.0	10	20	1.0	28	0.10	27	137	2.9	Hu et al.
50 MHz	1064	5	100 kHz	4.7	24	10	20	1.5	13	0.15	41	207	2.8	Hu et al.
50 MHz	1064	5	10 kHz	11	53	10	20	3.3	22	0.33	153	764	4.6	Hu et al.
10 Hz-1 kHz	800	1	N/A	13	N/A	0.10	40	1.0	N/A	10.4	30	N/A	2.9	Byskov et al.
10 Hz-1 kHz	800	1	N/A	19	N/A	0.10	40	1.5	N/A	15.1	48	N/A	3.2	Byskov et al.
10 Hz-1 kHz	800	1	N/A	147	N/A	0.10	40	12	N/A	117.0	410	N/A	3.5	Byskov et al.

Table 4.1: Comparison of Cu processing results from this work and previous publications.

(Intra-Burst) Repetition Rate	Wavelength (nm)	Number of pulses per burst	Burst Repetition Rate	Incident Pulse Energy (μJ)	Incident Burst Energy (μJ)	Pulse Duration (ps)	Spot Diameter (μm)	Pulse Fluence (J/cm^2)	Burst Fluence (J/cm^2)	Peak Intensity (TW/cm^2)	Ablation Rate (nm of depth per pulse)	Ablation Rate (μm of depth per burst)	Ablation efficiency ($\mu\text{m}^3/\text{J}$)	Reference
3456 MHz	1040	800	1 kHz	0.2	200	1	26	0.05	38	47	11	9.0	24	this work
3456 MHz	1040	800	1 kHz	0.2	150	1	26	0.04	28	35	11	8.5	30	this work
1728 MHz	1040	400	1 kHz	0.5	200	1	26	0.09	37	93	22	8.8	24	this work
1728 MHz	1040	400	1 kHz	0.4	145	1	26	0.07	27	68	20	7.9	29	this work
864 MHz	1040	200	1 kHz	0.9	180	1	26	0.17	34	0.17	40	7.9	23	this work
864 MHz	1040	200	1 kHz	0.6	120	1	26	0.11	23	0.11	34	6.9	30	this work
432 MHz	1040	100	1 kHz	1.4	140	1	26	0.26	26	0.26	71	7.1	27	this work
108 MHz	1040	25	1 kHz	5.9	147	1	26	1.1	28	1.11	215	5.4	19	this work
50 MHz	1064	8	1 kHz	5.0	40	10	unknown	N/A	N/A	N/A	58	0.47	8.2	Knappe et.al.
10 Hz	800	1	N/A	18	N/A	0.13	60	0.64	N/A	4.9	18	N/A	2.8	Bones et.al.
1 kHz	800	1	N/A	17	N/A	83	2	0.54	N/A	6.5	15	N/A	2.7	Hwang et.al.
1 kHz	800	1	N/A	0.32	N/A	0.08	2	10	N/A	121	890	N/A	8.9	Hwang et.al.
1 kHz	800	1	N/A	0.23	N/A	0.15	7.5	0.52	N/A	3.5	30	N/A	5.8	Crawford et.al.
1 kHz	800	1	N/A	0.73	N/A	0.15	7.5	1.7	N/A	11	70	N/A	4.2	Crawford et.al.
1 kHz	800	1	N/A	2.2	N/A	0.15	7.5	4.9	N/A	33	570	N/A	12	Crawford et.al.

Table 4.2: Comparison of Si processing results from this work and previous publications.

4.2 Cu and Si Micro-Machining with Uniformly Distributed and Bursts of Pulses

The systematic ablation experiments summarized in Fig. 4.2 were focused on making accurate comparisons between different laser operating regimes as fairly as possible. In order to minimize the effect of practical issues, there was applied only a single burst incident at any spot, making shallow holes, which also avoids complications such as effects of the walls when the depth gets larger than the spot size. In this section, an extensive set of experiments is being provided in which large pieces of material are cut or removed out with the laser. Therefore, they are highly representative of certain applications. In actual industrial usage, great effort is made to optimize any single of these processes, which have practical aspects that depend on many features, such as scanning sequence, speed, precise power of the laser, in some cases chemical and/or mechanical pre- and/or post-treatment of the surface, among others. No such effort has been made here as the focus is on the physics of the ablation cooling process, but as with all other experiments in this study, burst and uniform modes of operation are compared under completely fair conditions, keeping all other parameters of the laser and process constant.

The first type of micromachining experiments that were performed involved removing out a circular section of the material with the trepanning technique and removing out a volume via scanning over concentric circular hatches with multiple passes. The samples used in the experiments were 20- μm and 150- μm thick copper sheets and 450- μm thick single-side-polished Si wafers.

In laser trepanning, the laser spot is scanned over the same circular path over and over until the section is removed. During the trepanning experiments, only 20- μm thick copper foils were used in order to prevent any undesirable complications due to thickness of the material, such as formation of conical grooves [58,59], which arise because, as laser beam is being scanned continuously, the groove diameter shrinks, which leads to reduction of peak intensity at the focal point.

First set of trepanning experiments aimed to assess the time it takes, *i.e.* the number of laser passes, to remove the circular section with a diameter of $500\ \mu\text{m}$. The samples were placed onto the sample holder, where there was a hole with 1 inch diameter in the middle. An IR sensor was placed under the hole in order to record the drill time. To minimize the error, 10 trials were done for each laser mode. During the experiments, the scan speed was fixed at $10\ \text{mm/s}$, determined by $1\ \text{kHz}$ burst repetition frequency, in order to have $50\ \%$ overlapping spots, where, each spot was hit by a single burst. Under these conditions, the scanning time required for a single complete circular pass is 0.15 seconds. The average power on sample ($120\ \text{mW}$), hence, the burst energies were kept identical. For uniformly separated pulses at $27\ \text{kHz}$, this corresponds to same energy of a single burst applied in $1\ \text{ms}$ ($1\ \text{kHz}$ burst repetition rate). The overall image of the thin foil after trepanning operation can be found in Fig. 4.5. The details of the operating modes and the corresponding energies is as follows:

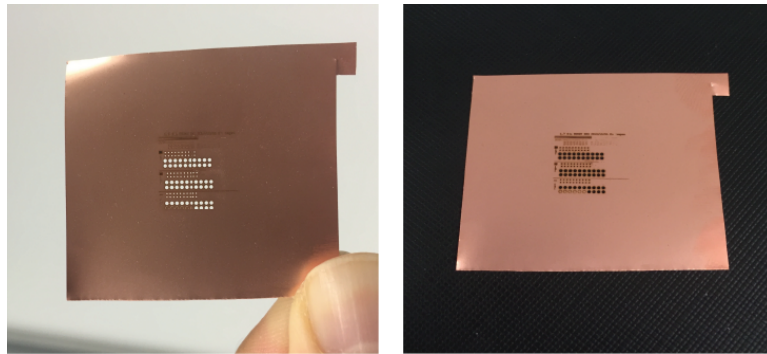


Figure 4.5: Photographs of the $20\ \mu\text{m}$ -thick copper foil after a series of trepanning operations with laser processing, including 60 zones with $150\text{-}\mu\text{m}$ diameter and 60 zones with $500\text{-}\mu\text{m}$ diameter.

- $1.73\ \text{GHz}$ intra-burst repetition rate, 400 pulsed burst with $1\ \text{kHz}$ burst repetition rate, $300\ \text{nJ/pulse}$ energy constituting $120\ \mu\text{J/burst}$ energy.
- $432\ \text{MHz}$ intra-burst repetition rate, 100 pulsed burst with $1\ \text{kHz}$ burst repetition rate, $1.2\ \mu\text{J/pulse}$ energy constituting $120\ \mu\text{J/burst}$ energy.
- $1.73\ \text{GHz}$ intra-burst repetition rate, 25 pulsed burst with $1\ \text{kHz}$ burst repetition rate, $4.85\ \mu\text{J/pulse}$ energy constituting $120\ \mu\text{J/burst}$ energy.

- 432 MHz intra-burst repetition rate, 25 pulsed burst with 1 kHz burst repetition rate, 4.85 μJ /pulse energy constituting 120 μJ /burst energy.
- 108 MHz intra-burst repetition rate, 25 pulsed burst with 1 kHz burst repetition rate, 4.85 μJ /pulse energy constituting 120 μJ /burst energy.
- 27 MHz intra-burst repetition rate, 25 pulsed burst with 1 kHz burst repetition rate, 4.85 μJ /pulse energy constituting 120 μJ /burst energy.
- 1 MHz intra-burst repetition rate, 25 pulsed burst with 1 kHz burst repetition rate, 4.85 μJ /pulse energy constituting 120 μJ /burst energy.
- 27 kHz uniformly separated pulses with 4.85 μJ /pulse energy.

The close-up microscope images after ablation together with the average total number of passes to drill vs laser operating mode is depicted in Fig. 4.6. Note that absolutely no chemical or mechanical cleaning was made. As it is clearly seen from Fig. 4.6. a-d, highly repetitive pulses applied as bursts, which effectively exploit ablation cooling, resulted in clear edges. In contrast uniformly repeated pulses at a slower repetition rate resulted in carbonization. In addition, most of the circular pieces did not come off just after processing with low repetition rates and they had to be plucked gently. It should be noted that the results presented here do not imply that good edge qualities cannot be obtained with uniform mode, but that this requires much higher energies. The trepanning time for each mode is presented in Fig. 4.6.e, which is in agreement with Fig. 4.2.a. The pulse energy was kept at the highest level possible, for which this comparative study could be made. As the chart clearly indicates, comparison of second and last bars reveal that with the help of ablation cooling, the 1728-MHz burst mode completes 3 times faster than the 27-kHz uniform mode, even though its pulse energy is less by factor of exactly 16.

In second set of trepanning experiments edge qualities were analyzed using a scanning electron microscope (SEM). However, since the uniform mode was barely able to make a full cut, for these experiments, the average power and pulse energy was increased by a factor of 2, such that both modes provide acceptable-quality cuts. Except the pulse energy and average power levels, all other scanning

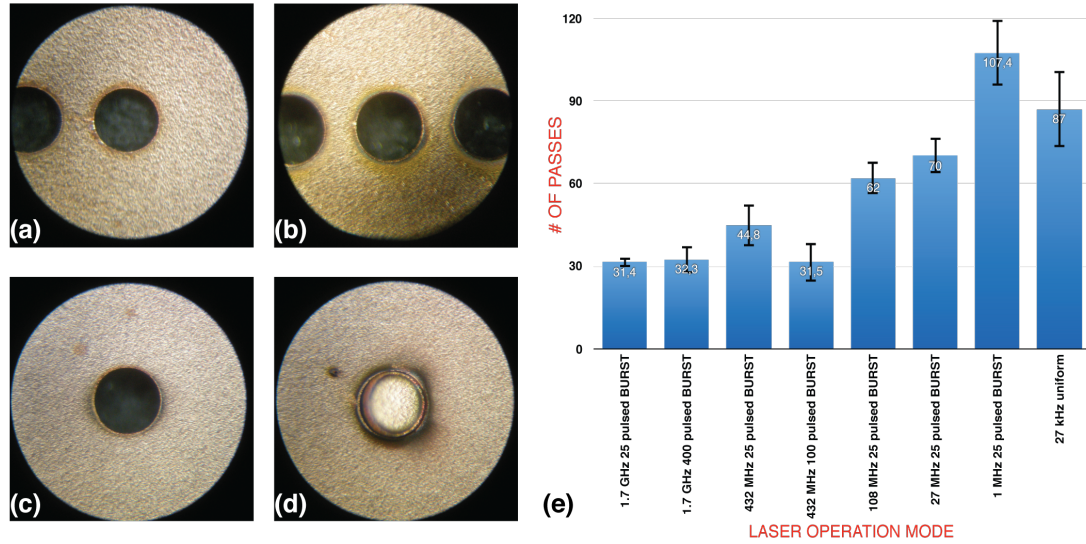


Figure 4.6: Microscope images of $20\ \mu\text{m}$ thick copper foil after trepanning together with the bar chart representing number of passes required vs. laser mode. (a) 400 pulsed burst at 1.73 GHz intra-burst repetition rate. (b) 100 pulsed burst at 432 MHz intra-burst repetition rate. (c) 25 pulsed burst at 27 MHz intra-burst repetition rate. (d) 27 kHz uniform repetition rate. (e) Number of passes required for drilling vs. laser operation mode. Each trepanning pass takes 0.15 seconds with 10 mm/s scanning speed in order to have 50 % overlapping spots. The error bars reflect the standard deviation of 10 trials for each mode.

parameters were kept identical with the first set of trepanning experiments. Using $20\text{-}\mu\text{m}$ copper foils, circular cuts with diameters of $150\ \mu\text{m}$ and $500\ \mu\text{m}$ were obtained. The details of the operating modes and the corresponding energies is as follows:

- 1.73 GHz intra-burst repetition rate, 400 pulsed burst with 1 kHz burst repetition rate, 600 nJ/pulse energy constituting $240\ \mu\text{J}/\text{burst}$ energy ($240\ \text{mW P}_{\text{avg}}$).
- 27 kHz uniformly separated pulses with $9.7\ \mu\text{J}/\text{pulse}$ energy ($240\ \text{mW P}_{\text{avg}}$).

The results are depicted in Fig. 4.7. Under identical conditions, burst mode appeared to cause cleaner edges than the uniform mode, with 16 times lower per pulse energies.

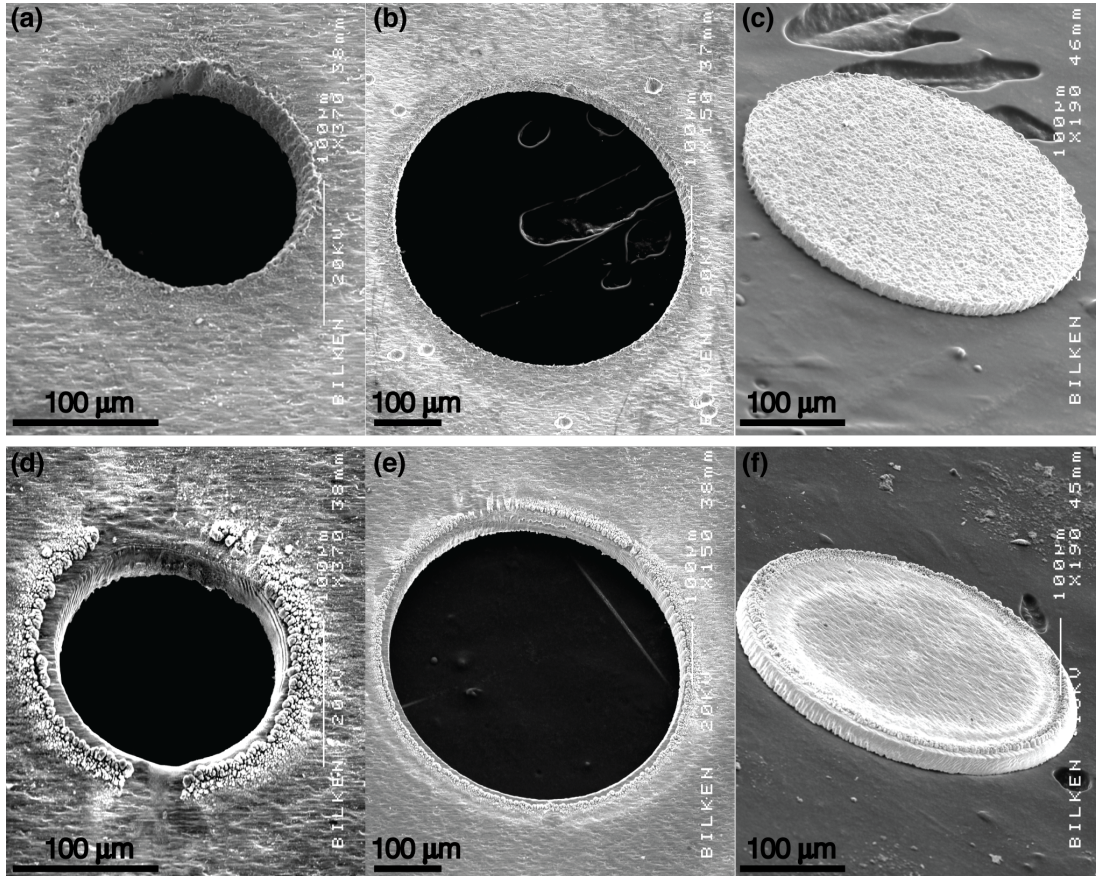


Figure 4.7: SEM images of thin copper foils after trepanning with 400-pulsed bursts at 1.73 GHz pulse repetition rate, 1 kHz burst repetition rate, 600-nJ pulse energy and 240 mW of average power on sample (burst mode) and corresponding uniformly repeated pulses at 27 kHz, 9.7- μ J pulse energy and 240 mW of average power (uniform mode). The scan speed was 10 mm/s in order to maintain 50 % overlap between bursts: (a) 150- μ m diameter circle removed with burst mode. (b) 500- μ m circle removed with burst mode. (c) The 20- μ m thick and 500- μ m wide foil piece, which was removed in (b). (d) 150- μ m diameter circle removed with uniform mode. (e) 500- μ m circle removed with uniform mode. (f) The 20- μ m thick and 500- μ m wide foil piece removed with uniform mode in (e).

In the third set of experiments, with an aim to remove out a volume of material, an alternative cutting procedure, which is better suited to thicker samples, was used: The laser spot was scanned over a very tightly wound spiral hatch with spiral arm separation of $12.5 \mu\text{m}$, which is half of the diameter of the focused laser spot. Together with 10 mm/s scan speed, 50% overlapping spots were obtained in angle, ϕ and radius, r . The experiments were performed on $150 \mu\text{m}$ thick copper samples as well as $450 \mu\text{m}$ thick single-side-polished silicon wafers. The diameter of the cylindrical volume was $500 \mu\text{m}$ in both cases.

The SEM images of the holes drilled with uniform and burst modes for copper are shown in Fig. 4.8. The SEM images of the holes drilled with burst mode for Si are represented in Fig. 4.9 and with uniform mode in Fig. 4.10. The edge quality of the holes for copper sample is quite similar for both laser-operating modes, even though energy per pulse was 16 times lower than it was in uniform mode. The difference between uniform and burst modes is much more dramatic in the case of Si target. Using uniform mode operation, extremely strong SiO_2 formation has been observed during processing, which is directly related to heating of the sample and the fact that the experiments were conducted in ambient atmosphere. In contrast, processing the Si sample with burst mode yielded a through hole with sharp edges, even though the pulse energy was 16 times lower. This critical experimental observation is another independent and strong, albeit indirect, evidence that processing at high repetition rates and thus exploiting ablation cooling not only makes the ablation process much more efficient, even when using drastically reduced individual pulse energies, but also reduces heating of the sample very substantially.

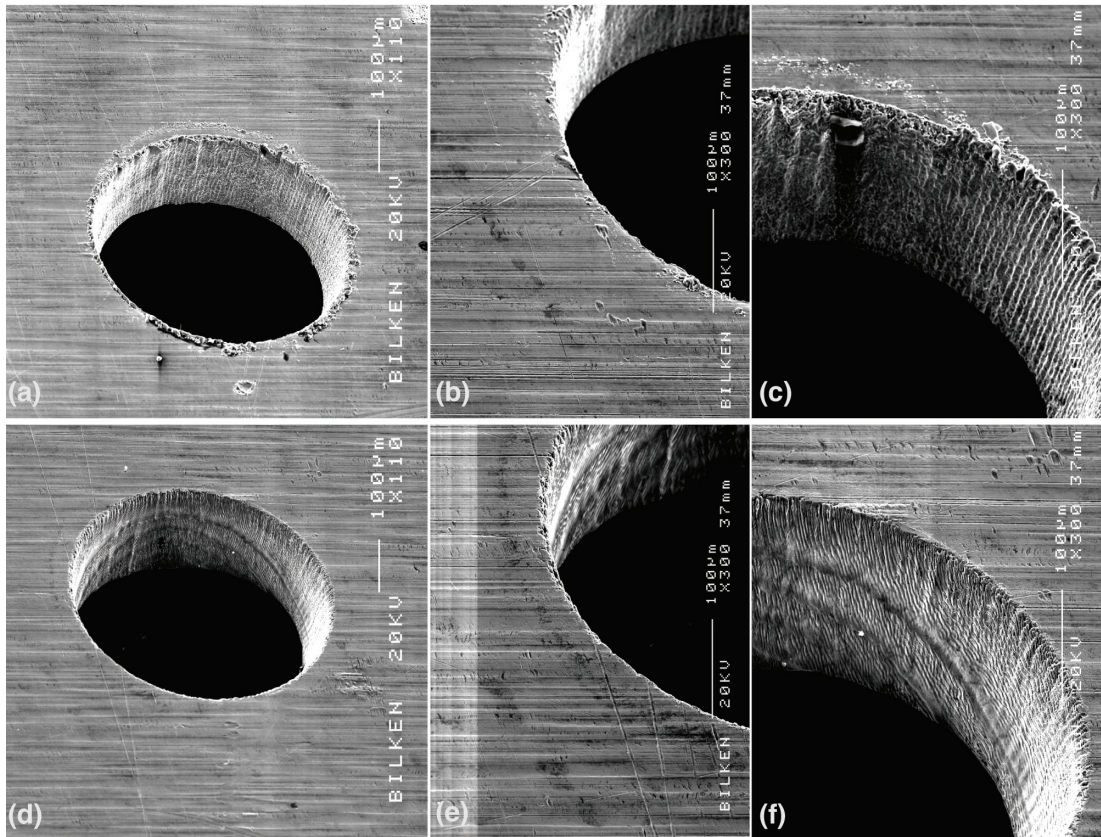


Figure 4.8: SEM images of 150- μm thick copper sheets after a scan following a very tightly wound spiral pattern (12.5- μm separation between each spiral arm) with 400 pulsed bursts at 1.73 GHz pulse repetition rate, 1-kHz burst repetition rate, 600 nJ of pulse energy and 240 mW of average power on sample (burst mode) and corresponding uniformly repeated pulses at 27 kHz, 9.7 μJ of pulse energy and 240 mW of average power (uniform mode). The scan speed is 10 mm/s in order to maintain 50% overlap between bursts. (a) Burst-mode processed hole with 500- μm diameter. (b), (c) Magnified edges of (a). (d) Uniform-mode processed hole with 500- μm diameter. (e), (f) Magnified edges of (d).

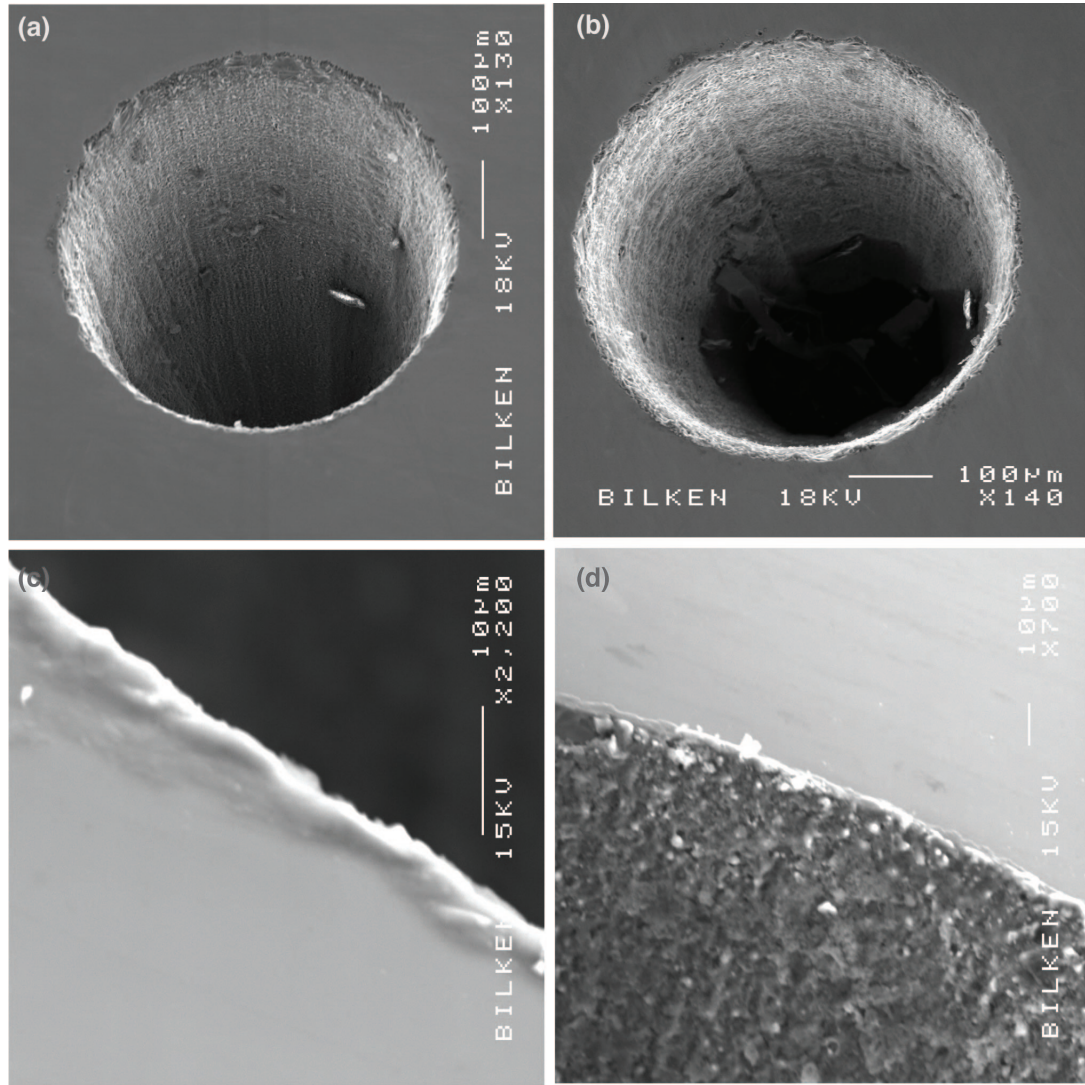


Figure 4.9: Drilling holes through 450- μm thick silicon wafer with burst mode: SEM images of holes formed by scans following a very tightly wound spiral pattern (12.5 μm separation between each spiral arm) with bursts of 400 pulses at 1.73 GHz intra-burst repetition rate, 1 kHz burst repetition rate, pulse energy of 600 nJ, and 240 mW of average power incident on sample. The scan speed was set to 10 mm/s in order to achieve 50% overlap between bursts. (a), (b) Two 500- μm through holes created using the burst mode. (c), (d) Magnified view of edges.

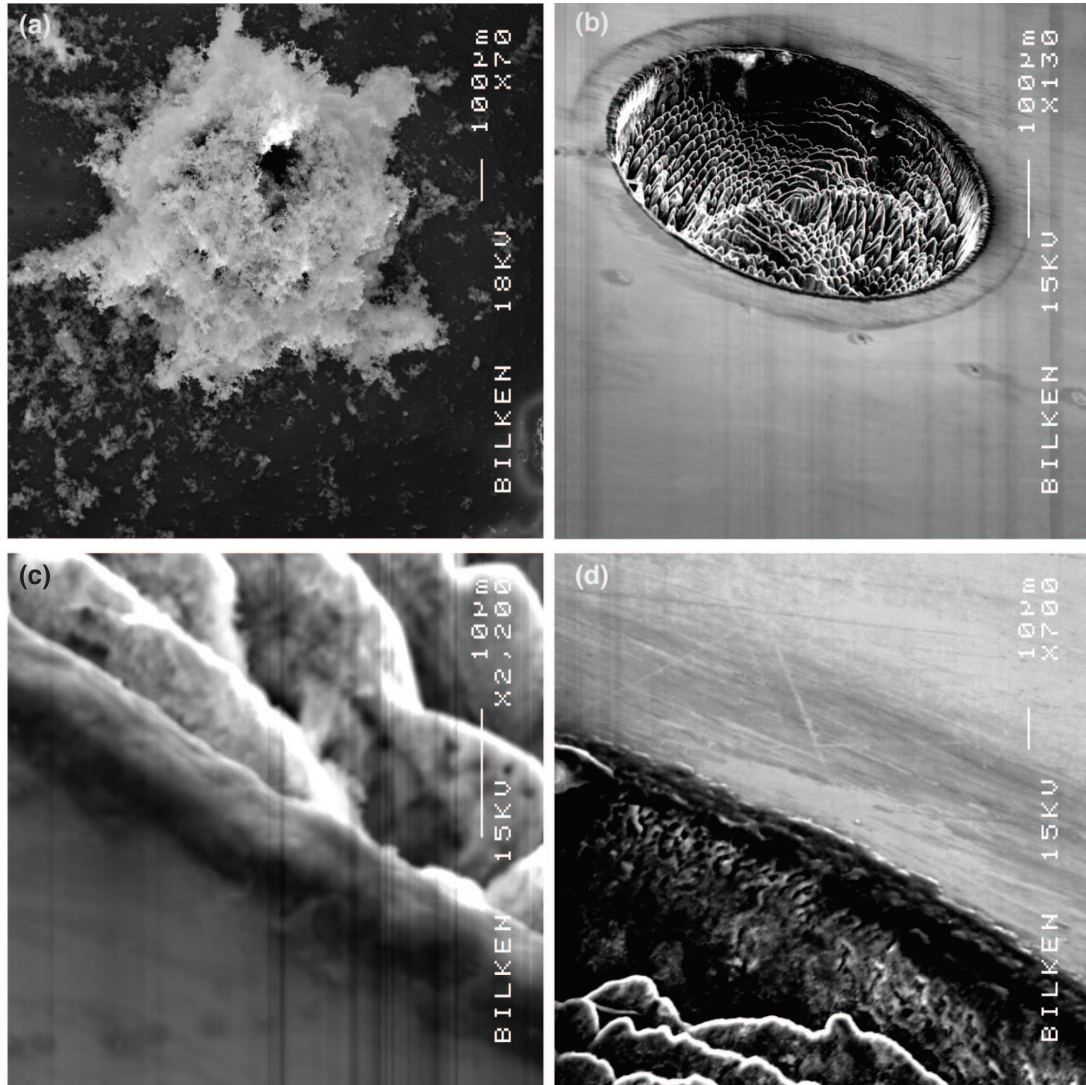


Figure 4.10: SEM images of 450- μm thick silicon wafers using uniform mode operation, tracing over concentric circles ($12.5\ \mu\text{m}$ separation between each circle) using $9.6\text{-}\mu\text{J}$ pulses at 25 kHz and 240 mW of average power. The scan speed was 10 mm/s. (a) Extensive SiO₂ formation is observed after processing. (b) Image taken from the same region, after the sample was chemically cleaned to remove the SiO₂ formation. (c), (d) Magnified edges of (b).

4.3 PZT Processing

Piezoelectric PbZrTiO_3 , lead zirconate titanate (PZT) ceramics have wide-ranging applications, including ultrasonic sensor arrays [42], miniature motors [60] and high-frequency ultrasonic imaging (20- 200 MHz) [61]. They also have high effective electromechanical coupling coefficient k_{33} . k_{33} is defined as the square root of ratio of mechanical energy stored to electrical energy applied, which is an indicator of the effectiveness with which a piezoelectric material converts electrical energy into mechanical energy or converts mechanical energy into electrical energy. The first subscript to k denotes the direction along which the electric signal is applied; the second denotes the direction along which the mechanical energy is applied or extracted. Cutting of piezoelectric ceramics for high-frequency imaging has been problematic because of the fine pitch (sub-50 μm) and very narrow kerf (sub-10 μm) required. Both wire and semi-conductor dicing saws are currently employed to cut basic transducer components from plates of raw material; however, these techniques have limitations such as a large kerf width, a simple pattern and a low product rate due to the breakage of the finished rods by directly contacting the diamond saw, especially for the highly brittle piezoelectric ceramics. In order to overcome these drawbacks, attempts have been made to employ laser micromachining, as a new promising technique, for cutting piezoelectric transducer materials [62,63], but can cause irreversible deterioration of piezoelectricity due to heating. PZT was chosen as a target to demonstrate effectiveness of ablation-cooled material removal, since it is straightforward to determine extend of thermal damage by characterizing the coupling coefficient as well as having technological relevance.

As target, PZT ceramic sheets of industry type 5A (T017-A4E-602, Piezo System, Inc, Wobum, WA, USA), which are 191 μm thick were used. Electromechanical coupling coefficient of k_{33} prior to cutting is specified to be 0.72 and used as a relative indicator of performance degradation due to laser cutting. The beam was focused on the targets with a 20x high-power focusing objective with a focal length of 10 mm. The spot size in the focal plane is measured to be 10 μm . The laser and the processing setup is the same as those used in hard-tissue processing

experiments (Appendix A.3). Burst-mode and uniform-mode has been applied to cut 1 mm-diameter circular sections of PZT and their electromechanical coupling coefficient was characterized to ascertain how well the inherent piezoelectricity of the material is preserved. The trepanning time was reduced by a factor of 9 for burst mode and resulted in 2 times higher coupling coefficient. The results are summarized in Table 4.3, which shows conclusively that burst-mode with 500 MHz intra-burst repetition rate results in better preservation of the coupling coefficient. All parameters of the laser, focusing and scanning were kept the same to ensure a fair comparison. No attempts were made to optimize the cutting process through adjustment of laser parameters in this work.

Processing Mode	Average power (mW)	Number of pulses per burst	(Burst) Repetition Rate	Incident Pulse Energy (μJ)	Incident Burst Energy (μJ)	Pulse Duration (ps)	Spot Diameter (μm)	Pulse Fluence (J/cm^2)	Burst Fluence (J/cm^2)	Peak Intensity (TW/cm^2)	Sample Rotation Speed ($25^\circ/\text{s}$)	Cutting Time (min)	Measured Coupling Coefficient, k_{33}
Burst mode	500	25	1 kHz	20	500	1	25	3.20	80	3	22	4.03	0.38
Uniform mode	500	1	25 kHz	20	20	1	25	3.20	3	3	20	32.2	0.18
Burst mode	500	50	1 kHz	10	500	1	25	2.04	102	2	40	5.24	0.30
Uniform mode	500	1	25 kHz	10	10	1	25	2.04	2	2	34	41.9	0.15

Table 4.3: Comparison of results on cutting PZT ceramic into 1 mm-diameter circular sections.

Chapter 5

SOFT and HARD TISSUE ABLATION

As a straightforward consequence of the higher ablation efficiency and energy conservation, laser-deposited energy is expected to be better confined to the laser spot and any undesired thermal effects to the surrounding region should be reduced substantially in the ablation cooling regime (Figs. 2.6 and 2.7). This effect is most important for and most easily demonstrated through processing of temperature-sensitive materials, particularly biological tissue.

Tissue removal may well be regarded as the ultimate test of suppression of thermal effects since only a few degrees of temperature rise can lead to degradation. In order to assess the thermal damage, several experiments on human tooth and rat brain samples were accomplished with burst and uniform modes. During the burst mode vs. uniform mode comparison experiments, all parameters of the laser, focusing, scanning speed and processing time were kept the same to ensure a fair comparison in addition to the per pulse energy, so as average power. Additionally, in order to show the effectiveness of the burst mode just after the processing, other sets of experiments were done on agar hydrogel blocks.

In this chapter, systematic comparisons between burst-mode (appreciable ablation cooling) and uniform-mode (negligible ablation cooling) processing with identical laser, focusing and scanning systems will be explained. This way, it was possible to minimize experimental uncertainties and to ensure that all parameters, except the temporal sequence of the pulses, could be kept exactly the same.

5.1 Agar Gel and Soft Tissue Ablation

During soft tissue experiments, two separate custom built fiber lasers were used. The first system is able to produce bursts of pulses with pulse duration of 300 fs and intra-burst repetition rate of 22.3 MHz, whereas, can also be operated in uniform mode. The details of the first system is given in Appendix. A.2. The second one is able to produce bursts of pulses with pulse duration of 1 ps and variable intra-burst repetition rate between 1 MHz and 3.5 GHz and can also be operated in uniform mode. The details of the second system is given in Appendix. A.1. On the other hand, for agar hydrogel processing, only the 22.3 MHz - 300 fs system was utilized.

In order to assess damage due to laser ablation, tissues were stained with hematoxylin & eosin and DAPI following fixation, tissue preparation and paraffin embedding procedures. Hematoxylin & Eosin staining is a well known technique to examine histological and morphological changes of tissue. In many studies [64–66] it is also used for determining tissue damage. Some other studies directly indicate thermal damage due to laser ablation by h&e staining [11, 67]. Excluding enzymatic reactions, dead live cell determination is mostly based on cell membrane permeability; however, tissue fixation causes all cells to have an increased permeability. Loss in intact nuclear shape indicates cell damage [68]. DAPI is a fluorescent stain, which can penetrate through cell membrane and attach directly to DNA [69]. If the cell membrane is damaged and loses its intact form after ablation, the disintegrated nucleus and DNA reside in the extracellular matrix, which is seen as diffused light under fluorescent microscope.

5.1.1 Experiments with 300 fs system

The scanner focuses the beam with an f-theta objective, which ensures a constant spot size within a plane. The spot diameter is estimated to be $\sim 8 \mu\text{m}$, which is confirmed by directly observing craters formed after a raster scan on the surface of a copper plate via reflection microscope and independently by the knife-edge method. The target sample is positioned on a manual 3D stage, which allows translation by 10 cm in 3 axes.

The samples used in the experiments are agar (Agar No: 1, LabM) hydrogel blocks (2 g of agar per 100 ml of distilled water) and freshly harvested rat brain tissues, which were processed within an hour after dissection. In these experiments, we tested the effect of two operating modes, *i.e.*, 200 kHz uniform repetition rate mode, and 4 pulsed-burst mode with burst repetition rate of 50 kHz and intra-burst pulse repetition rate of 22.3 MHz. Hydrogel is preferred especially to compare two operating modes because it is easy to mold to a flat surface, easy to characterize under light microscopy and is a naturally derived hydrogel polymer that has similar molecular properties to extracellular fluid in biological tissues [70]. In all of the mode comparison experiments, the pulse duration, delivered fluence and average power are all kept constant.

For the hydrogel experiments to ensure that the focal plane coincides with the target surface, calibration lines were processed at a speed of 5 mm/s prior to ablation. The optimum focal point was determined by maximizing the brightness of the plasma generated on the surface. The scan speeds were adjusted to 125 mm/s such that approximately 8 pulses for uniform mode and 2 bursts (4 pulses/burst) for burst mode were incident per focal spot. Fig. 5.1.a. shows the light microscope image of the hydrogel lesions, created at different individual pulse energy values and compared for burst and uniform repetition rate modes.

For the tissue experiments, following extraction, the brains were sliced parallel to the coronal plane and the slice to be used was immediately placed on the processing platform. The pulse energy was set to $3 \mu\text{J}$ at an average power of 600 mW in the experiments. Raster scans were performed over an area of 1 mm x 1

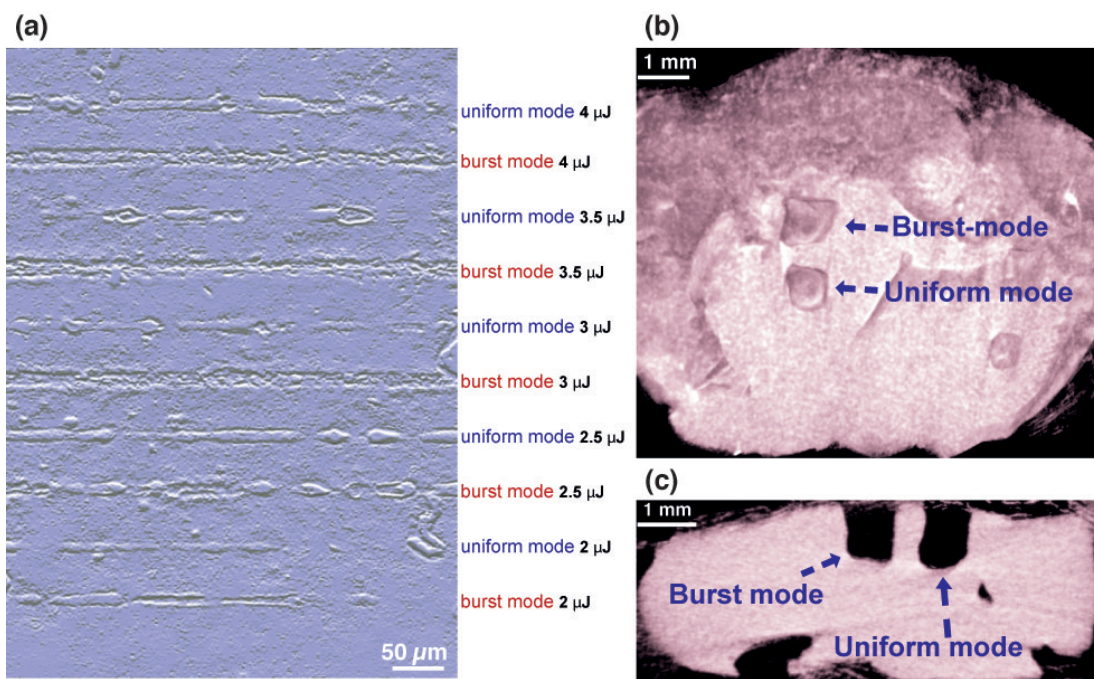


Figure 5.1: (a) Microscope image of hydrogel block, raster-scanned with 200-kHz uniform repetition rate and 4-pulsed burst mode at the indicated pulse energies. Micro CT images of the processed rat brain tissue sample: (b) Top view of the coronal slice where four excisions made in (1) 4 pulsed-burst mode and (2) 200-kHz uniform repetition rate. (c) Sagittal view of the excisions in (b).

mm with line separation of $2.5 \mu\text{m}$ and scan speed of 250 mm/s and with 80% duty cycle to avoid excessive heating. The raster scan was then repeated 50 times with total exposure time of 80 s. During the experiment, NaCl solution was sprayed regularly on the samples to prevent the tissue from drying. At the beginning of the experiment and in between consecutive raster passes, the optimum focal spot was readjusted to match the surface based on brightness of the generated plasma. After irradiation, the samples were preserved in 4% paraformaldehyde solution, and then examined with a micro-CT scanner (Skyscan 1172, Bruker in BIOMATEN METU). Micro-CT analysis was made with 60 kV and $160 \mu\text{A}$ with 0.5 mm Al filter and at a resolution of $12 \mu\text{m}/\text{pixel}$. Fig. 5.1(b) and (c) show the images of processed tissue. Histological analyses were also made on several samples. Following fixation, and tissue preparation, the samples were embedded into paraffin blocks and then cut into $5 \mu\text{m}$ slices in sagittal plane, perpendicular to tissue surface. Then, slices were examined under light microscopy (Leica, DM 5000 B) following a standard hematoxylin & eosin staining procedure.

For hydrogel experiments, it is seen that, at pulse energies exceeding $2.5 \mu\text{J}$, the lesions formed by burst-mode operation are continuous and uniform, whereas the lesions formed by uniform repetition rate mode are not (Fig. 5.1.a.). Given that the pulse duration, delivered fluence and average power are all identical, these results demonstrate that the cumulative effect of the pulses in a burst leads to increased ablation effectiveness. Using uniform repetition rate pulses, even at $4\text{-}5 \mu\text{J}$ per pulse, the cuts are not continuous. Utilizing higher pulse energies results in localized melting of the hydrogel sample due to correspondingly higher average power, in addition to precluding delivery through fiber. Reducing the repetition is naturally a possibility, but also reduces the processing speed.

The depth of the lesions on brain tissue were measured to be $\sim 1200 \mu\text{m}$ and $\sim 1100 \mu\text{m}$ for 4-pulsed burst and 200 kHz uniform repetition rate modes, respectively. Our results indicate that it is possible to ablate $\sim 1 \text{ mm}^3$ of tissue within 80 s ($0.75 \text{ mm}^3/\text{min}$) without any apparent heat damage to surrounding tissue. In contrast, earlier reports with solid state lasers utilized much higher energies and lower repetition rates. Using $165\text{-}\mu\text{J}$, 180-fs pulses at 100 Hz, 0.55-mm^3 section of bovine brain was ablated in 360 s ($0.09 \text{ mm}^3/\text{min}$) [11]. No clear

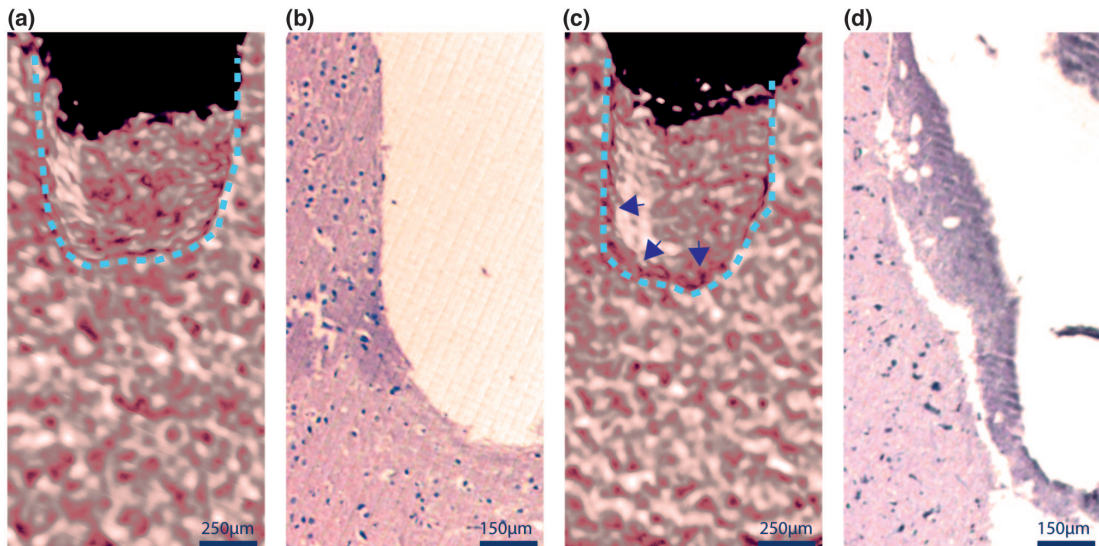


Figure 5.2: (a) Color and contrast enhanced sagittal view of 4-pulsed burst ablation region from 3D volumetric reconstruction of Micro CT data. Dashed lines represent the edges of processed region. (b) Light microscopy image of 4-pulsed burst ablation region after histological preparation. (c) Color and contrast enhanced sagittal view of 200 kHz ablation region from 3D volumetric reconstruction of Micro CT data. Dashed lines represent the edges of processed region. Arrows show the thermal damage zone. (d) Light microscopy image of 200 kHz ablation region after histological preparation.

difference is observed between uniform repetition rate and burst-mode operation during multiple-pass processing of rat brain tissue. This is likely due to the fact that ablation process halts after several scans over a given point and is re-initiated after re-adjustment of the focal plane, which was done manually in our experiments. The ablation speed can likely be improved substantially with an automated focusing system.

Even if the ablation depths are quite similar for both 4-pulsed burst mode and 200 kHz uniform repetition rate mode (Fig. 5.1.c.), histological analysis reveals that there exists tremendous amount of heat affected zone for 200 kHz mode ablation, as compared to 4-pulsed burst mode. 4-pulsed burst application has minimized collateral damage to the tissue. On the other hand, 200 kHz application damaged cells. Also devascularization can be seen in Fig. 5.2.d. Very little amount of tissue damage is observed in 4-pulsed burst application, which is localized to a specific area as seen in Fig. 5.2.b. This might be due to the ablation

scheme and improper focus adjustment. However, there is a prominent tissue loss and damage under 200 kHz application site. Fig. 5.2a. and c. shows the zoomed in side views of ablation craters of 3D reconstructed volumetric images of the regions processed with 4-pulsed burst and 200 kHz modes, respectively. The dashed lines show the edges of the ablation. The images were enhanced in terms of contrast, brightness and saturation in order to emphasize on the tonality difference between normal tissue and thermal damage region in Fig. 5.2.c. The darker color in between the dashed lines and the arrows represents the heat affected zone and is in good agreement with the histological cross section of Fig. 5.2.d. This contrast might be due to 1-2% x-ray attenuation difference between normal tissue and the tissue with edema [71].

The histological differences between the two operating modes are due to repetition rate differences and interaction regime of the laser pulses with the tissue, as reflected in different ablation efficiencies. During experiments for both modes of operations, the scan speed was adjusted so that four pulses were delivered per spot. This corresponds to delivery of that four pulses in 200 ns and an idle period of 20 μ s for burst mode and in 20 μ s with the period of 5 μ s for 200 kHz uniform repetition rate mode. The thermal relaxation time of biological tissues for 100 μ m spot diameter and with linear absorption coefficient of 1000 cm^{-1} is in the order of 100 μ s for a pulse duration of 1 μ s [72]. However, in our case, the interaction regime is totally different, therefore, linear absorption has very little effect on ablation, whereas, absorbed energy density is expected to be trapped in a much more shallower region [73]. Besides, during a burst, incoming pulse is expected to be delivered on denser plasma at a higher temperature because of 50 ns time separation between consecutive pulses, which will increase the efficacy of that pulse and cause quasi-continuous material ejection. On the other hand, for 200 kHz uniform repetition rate mode, since the separation between pulses is 5 μ s, the effect of the incoming pulse will be much less and the residual heat caused by the previous pulse would already be transferred to the deeper regions. In other words, incoming pulse spends most of its energy to re-heating of the surface rather than delivering it to the plasma. Considering these, the relaxation time could be between 5 μ s and 20 μ s.

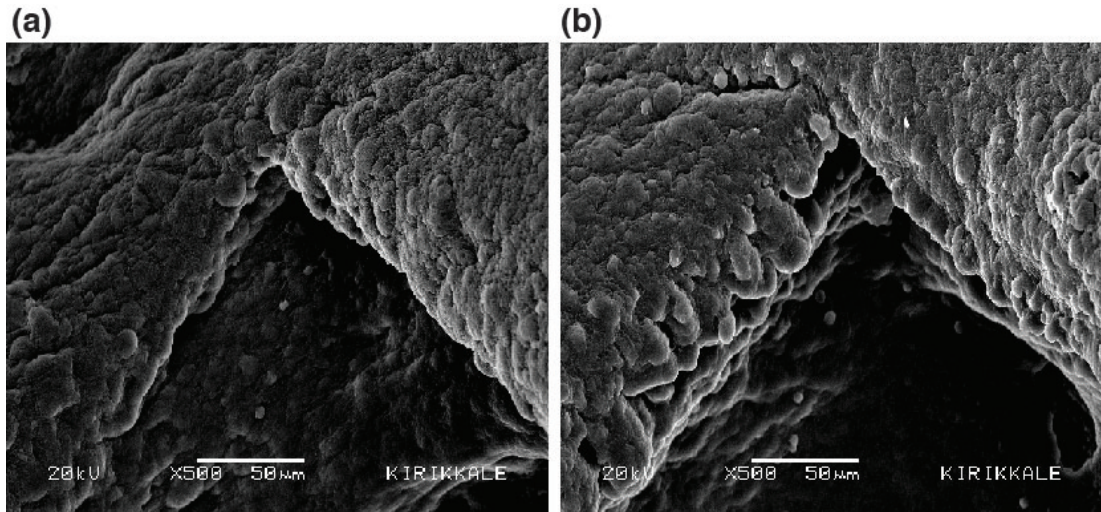


Figure 5.3: SEM images of the edges. (a) Lesion ablated with 4 pulsed-burst mode. (b) Lesion ablated with 200 kHz uniform mode.

The other laser-processed samples that were not prepared for histological analyses were prepared for SEM imaging following a routine fixation - dehydration - coating procedures. SEM images of the ablated lesions with both 4 pulsed-burst mode and 200 kHz uniform mode are given in Fig. 5.3.a. and b. respectively, where ablation with burst mode results in slightly smoother edges.

5.1.2 Experiments with 1 ps system

In order to test the effectiveness of ablation cooled laser material ablation on soft tissue, a number of experiments were performed on rat brain tissue, in addition to the burst-uniform mode comparison experiment described in previous section above. The laser system, which is described in detail in Appendix A.1 has been operated for the experiments in this section. In these experiments, 1 ps-long pulses were focused to a spot of 24- μm diameter. At the repetition rate multiplier stage, the coupler output producing 432 MHz repetition has been fed through the first devoted preamplifier just after the repetition rate multiplier. At the scanning end, the galvo-scanner was programmed to process a square region with 1 mm \times 1mm dimensions. Several raster patterns consisting of parallel lines was scanned 100 times each at 270 mm/s velocity and 12.5 μm line separation. With these parameters, 50 % overlap between ablation spots was assured. The total scanning time for overall processing was thus 30 seconds, where this process resulted in ~ 2 mm³/min of ablation speed. The burst mode parameters were as follows:

- 432 MHz intra-burst repetition rate, 7 pulsed burst with 27 kHz burst repetition rate, ~ 15 μJ /pulse energy equivalent to 100 μJ /burst energy and 2.7 W average power.

After irradiation, the samples were preserved in 4% paraformaldehyde solution. Following fixation, and tissue preparation, the tissue samples were embedded into paraffin blocks and then cut into 8 μm slices in sagittal plane, perpendicular to tissue surface. Several slices were obtained and half of them were followed up by standard hematoxylin & eosin staining procedure, where the other half has been processed with a standard DAPI staining procedure.

The histology results were analysed using light and fluorescent microscopy. Light and fluorescent microscopy images of a cross-section of the ablated region obtained after H&E and DAPI staining (separate samples) are shown in Fig. 5.4.a and b, respectively. Heat affected regions have darker purple colour, which is limited within 5 μm of the side edges and 10-15 μm of the bottom edge (along

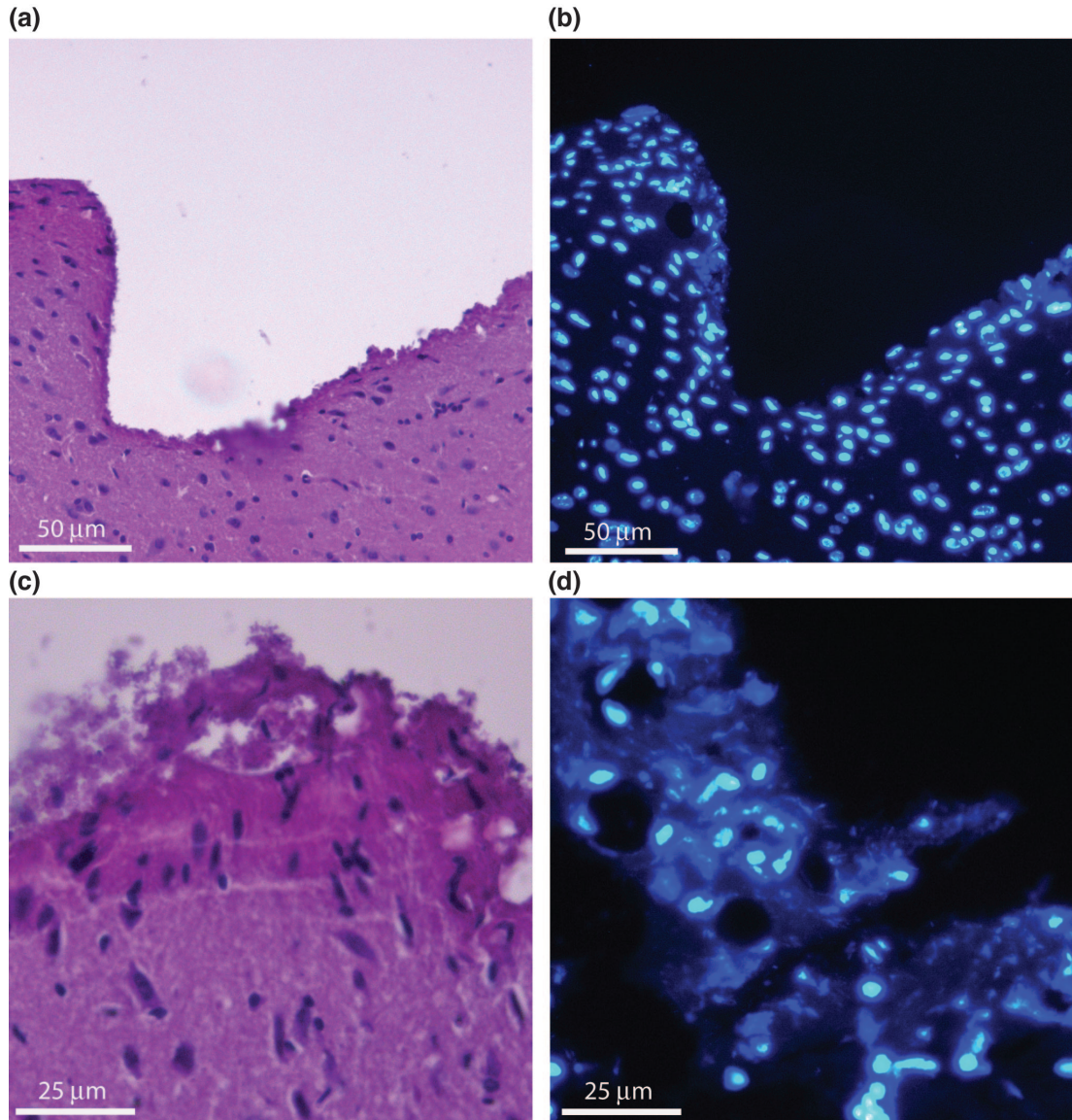


Figure 5.4: Histology results of the regions ablated with intra-burst repetition rate of 432 MHz with 7 pulses per burst, burst repetition rate of 27 kHz and average power of 2.7 W. (a) Light microscope image of H&E stained ablated region. (b) Fluorescent microscope image of DAPI stained ablated region, obtained from another sample. (c) Light microscope image of H&E stained ablated region, where scanning has been momentarily stopped to intentionally cause a heat-affected zone. (d) Fluorescent microscope image of the DAPI-stained ablated region, where scanning has been momentarily stopped to intentionally cause a heat-affected zone, obtained from another sample.

the direction of beam propagation). The nuclei (particles in black) seem to be intact and in place. As mentioned above, intact nuclei appear as blue elliptical regions, whereas deformed nuclei and DNA diffused to the extracellular matrix are seen as lighter blue regions covering a larger area than that of a single nucleus. As a control experiment, designed to highlight the effectiveness of this method to label heat affected areas, we have intentionally halted laser scanning briefly at the corner of the ablation zone during the experiment, therefore intentionally causing thermal damage. Indeed, the stained slices obtained from those regions, which are shown in Fig. 5.4.c and d clearly indicate this. The darker upper regions in the former and diffused blue light region in the latter are easily observable and correlate with thermal damage.

5.2 Hard Tissue (Dentine) Ablation

Hard tissue experiments were conducted on human dentine to illustrate the benefits of ablation cooling and to contrast the effects of burst and uniform modes, such as collateral damage and speed of ablation. Samples were first cut with a diamond saw in order to have at least one flat surface. The flat surface was aligned to be perpendicular to the incoming beam and observed under CCD camera for proper positioning. Two separate custom built burst mode fiber lasers were utilized during the experiments. The details of the first setup is given in Appendix. A.3. By utilizing this system, the tissues were processed at 500-MHz intra-burst repetition-rate with 1 kHz burst repetition rate by applying 1 ps pulses together with its corresponding uniform mode. The samples were fixed on the 3-axis motorized and computer controlled stage and the beam was focused with 10x objective. Second system's details are given in Appendix. A.1. By utilizing this system, the tissues were processed at 1.73-GHz intra-burst repetition-rate with 1 kHz and 25 KHz burst repetition rates by applying 1 ps pulses together with their corresponding uniform modes. Although the operating principles of the second system is similar to the first one, it is the upgraded version. Besides, instead of moving the sample with motorized 3D stage, the beam was scanned with 2D galvo-scanner, thus enable for faster scanning.

5.2.1 Experiments at 500 MHz repetition rate

Two operation modes were used during the ablation processes: (i) 25 kHz pulses with uniform repetition rate and (ii) 25 pulses separated by 2 ns comprising each burst (500 MHz intra-burst repetition rate), for which the burst repetition period was 1 ms (1 kHz). The average power was kept around 450 mW for both modes. For each mode of the system, the motorized stage was driven at speeds of 0.1 mm/s and 0.5 mm/s, raster scanning a region of 1 mm x 1 mm. The distance between two lines was 10 μ m and the ablation pattern was repeated two times. The number of bursts per spot was 100 ($v=0.1$ mm/s) and 20 ($v=0.5$ mm/s) respectively, which corresponds to 2500 and 500 pulses per spot. Saline solution

was sprayed regularly on the surface during the scanning process and plasma spark was observed continuously and used for manual re-alignment of the focus. All parameters of the laser, focusing and scanning were kept the same to ensure a fair comparison. Virtually identical samples were processed using both uniform and burst-mode pulses. While the uniform mode resulted in excessive carbonization (Fig. 5.5.c. - d.) to the extent that it was not possible to characterize the depth of the ablated zone accurately, the burst mode achieved clean removal of approximately 1 mm x 1 mm x 0.4 mm section (Fig. 5.5.a. - b.). Since the total amount of energy delivered to the sample was exactly the same (same laser power, spot size and processing time), the carbonization with the uniform and lack of it with the burst modes proves that thermal effects to the rest of the target material are greatly reduced in the ablation cooling regime.

Corresponding 3D volumetric images of the processed regions (Fig. 5.5.a. and b.), acquired from laser scanning microscope (LSM) is presented in Fig. 5.6. LSM-acquired-high-resolution images showing the edge quality is given in Fig. 5.7 and SEM images are presented in Fig. 5.8. In three of them, the sharp edges and the extracted volume is clearly observable. Supplementary figures obtained from an OCT (Optical Coherence Tomography) system (930 nm Callisto Spectral Domain OCT, Thorlabs, Newton, NJ, USA) are presented in Figs. 5.9 - 5.11. The sharp edges of the ablation zone are also clear in OCT surface profile (Fig. 5.9) and B-scan results (Fig. 5.10). Due to carbonization after processing with 25 kHz uniform mode, darker ring is observed in Fig. 5.11. b., which is due to the high absorption of OCT probe beam at HAZ (Heat Affected Zone).

The use of burst-mode pulses has led to formation of deep and cleanly drilled sections with no apparent heat-related damage with an average depth of ~ 350 μm . In contrast, the uniform-mode has resulted in significant carbonisation. SEM and LSM images allow quantification of the results, which show that the ablation depth is approximately the same for both scanning speeds. This suggests that the ablation rate was limited by the scanning speed, rather than laser processing, which motivated the follow-up study described in the next section, involving galvo scanners. The LSM images also reveal that the edge quality of the holes is excellent. The small cracks and chips seen in the SEM imaging formed during

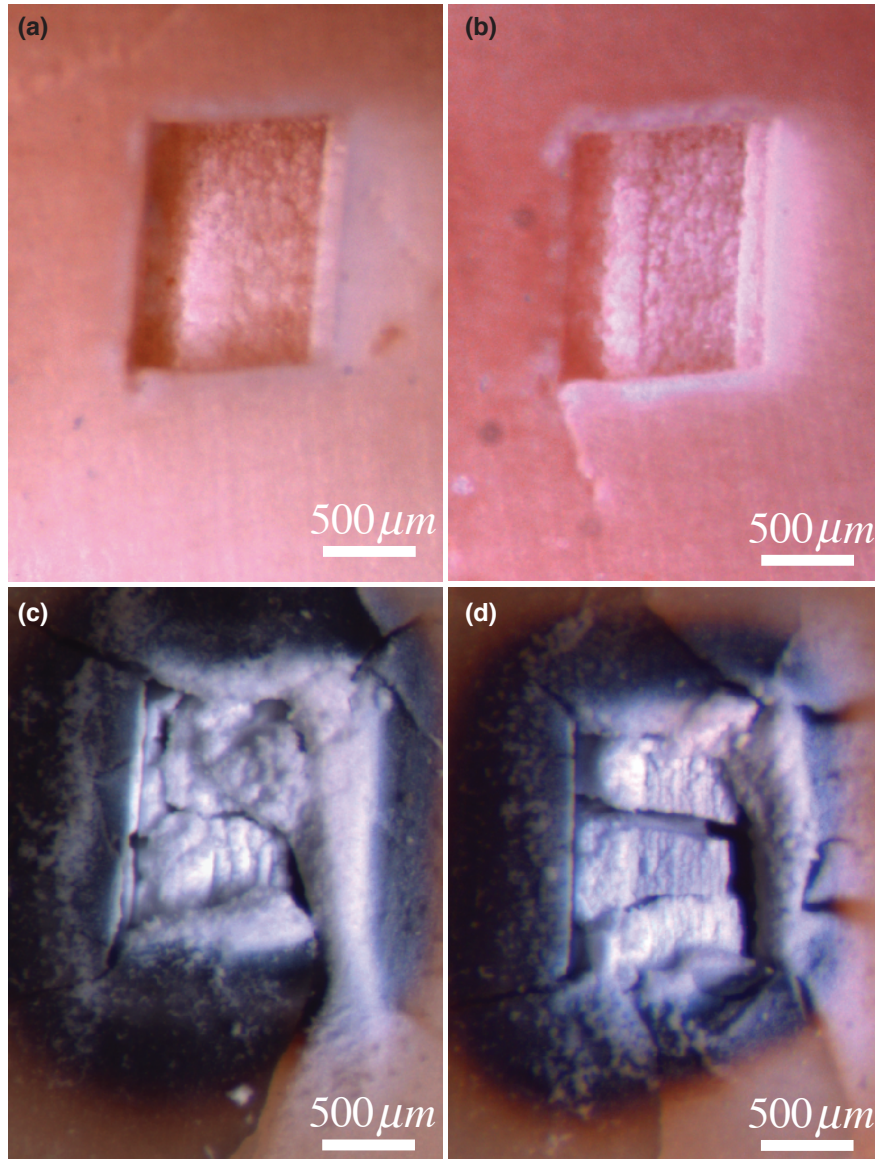


Figure 5.5: Comparison of burst-mode and uniform-mode ultrafast laser processing based on light microscopy: Laser ablation results for human dentine obtained while keeping all laser parameters (including peak and average power, spot size and total exposure) fixed except for mode of operation, (a) 500 MHz burst mode with scan velocity of 0.1 mm/s, (b) 500 MHz burst mode with scan velocity of 0.5 mm/s, (c) 25 kHz uniform mode with scan velocity of 0.1 mm/s, (d) 25 kHz uniform mode with scan velocity of 0.5 mm/s.

the vacuum process and were not present on the samples originally.

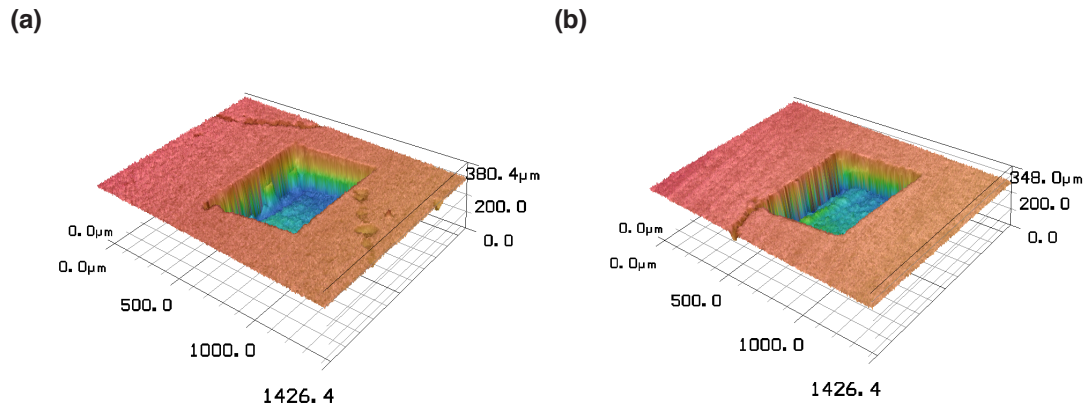


Figure 5.6: 3D depth profile obtained with Laser Scanning Microscope: (a) 500 MHz burst mode with scan velocity of 0.1 mm/s, (b) 500 MHz burst mode with scan velocity of 0.5 mm/s.

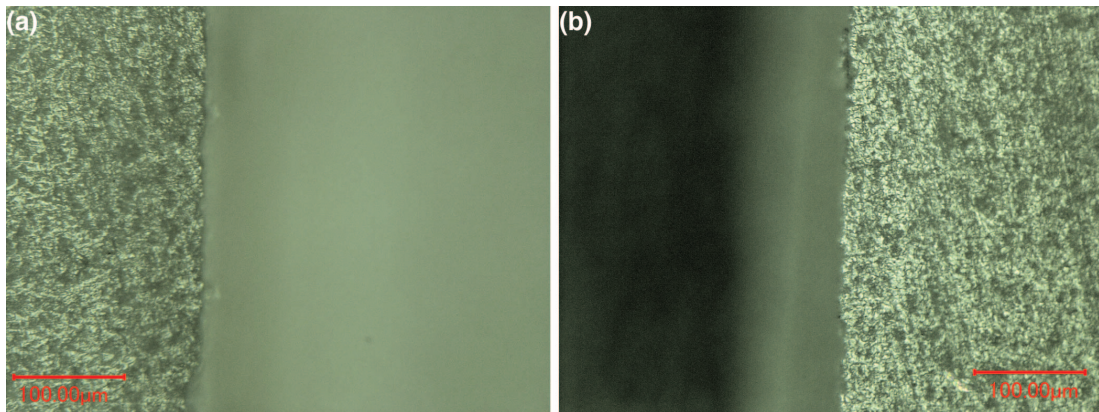


Figure 5.7: LSM-acquired high-resolution image showing the excellent edge equality of the same holes obtained at scan speeds of (a) 0.1 mm/s and (b) 0.5 mm/s.

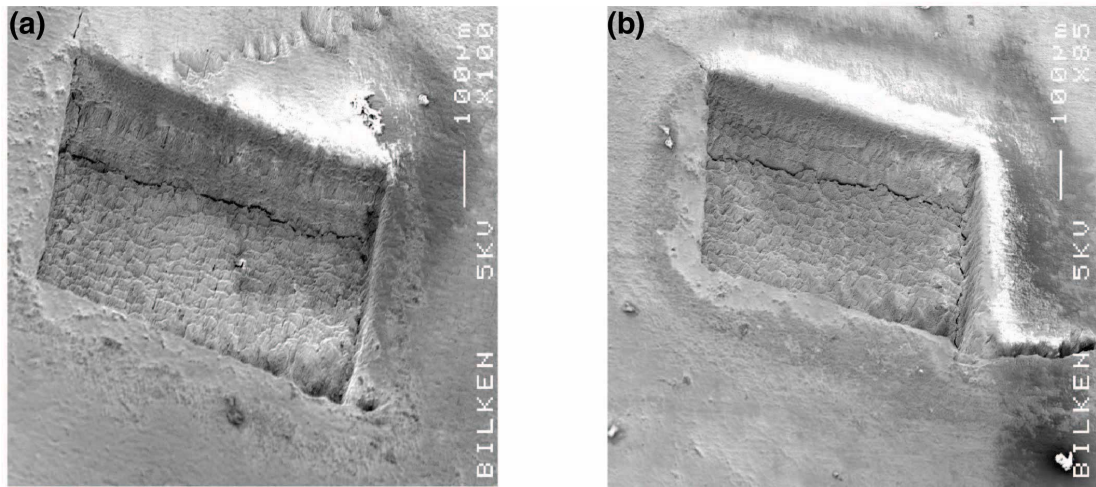


Figure 5.8: Scanning Electron Microscope images of ablated lesions of human tooth processed with (a) 25 pulsed 500 MHz burst mode with burst period of 1 ms and at a scanning velocity of 0.1 mm/s and (b) 25 pulsed 500 MHz burst mode with burst period of 1 ms and at a scanning velocity of 0.5 mm/s. It should be noted that cracks at the edges are due to vacuum procedure during SEM imaging, and the bright zones are due to the excess charge accumulation on tooth sample.

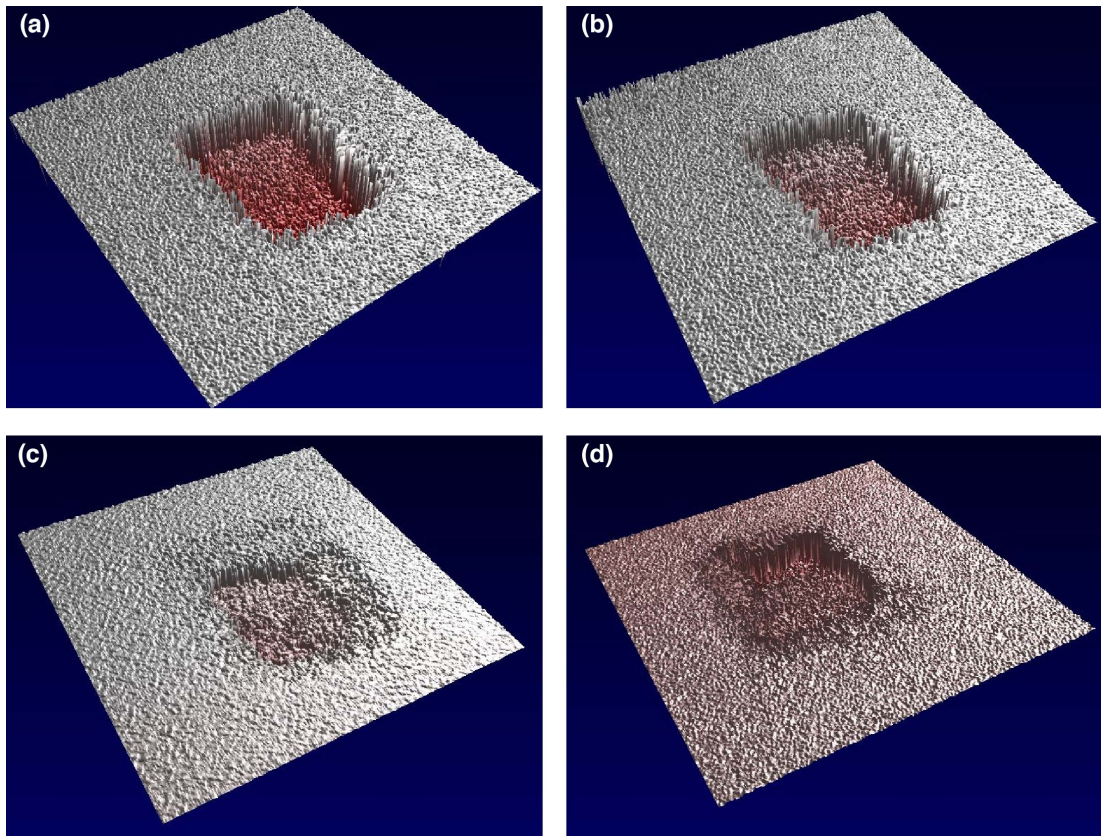


Figure 5.9: Surface profile of tooth samples, after ablation process, obtained with an OCT system. Processed with (a) 500 MHz burst mode and at a scanning velocity of 0.1 mm/s, (b) 500 MHz burst mode and at a scanning velocity of 0.5 mm/s, (c) 25 kHz uniform repetition rate mode at a scanning velocity of 0.1 mm/s and (d) 25 kHz uniform repetition rate mode at a scanning velocity of 0.5 mm/s.

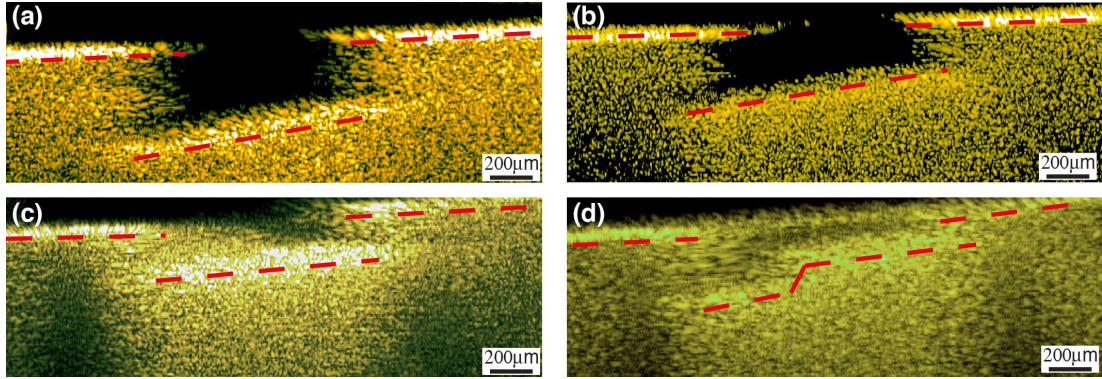


Figure 5.10: B-Scan results of tooth samples, after ablation process, obtained with the OCT system. The slice in view was obtained from the middle of the ablation zone. Processed with (a) 25 pulsed 500 MHz burst mode with burst period of 1 ms and at a scanning velocity of 0.1 mm/s, (b) 25 pulsed 500 MHz burst mode with burst period of 1 ms and at a scanning velocity of 0.5 mm/s, (c) 25 kHz uniform repetition rate mode at a scanning velocity of 0.1 mm/s and (d) 25 kHz uniform repetition rate mode at a scanning velocity of 0.5 mm/s. The dashed red lines indicate the surface.

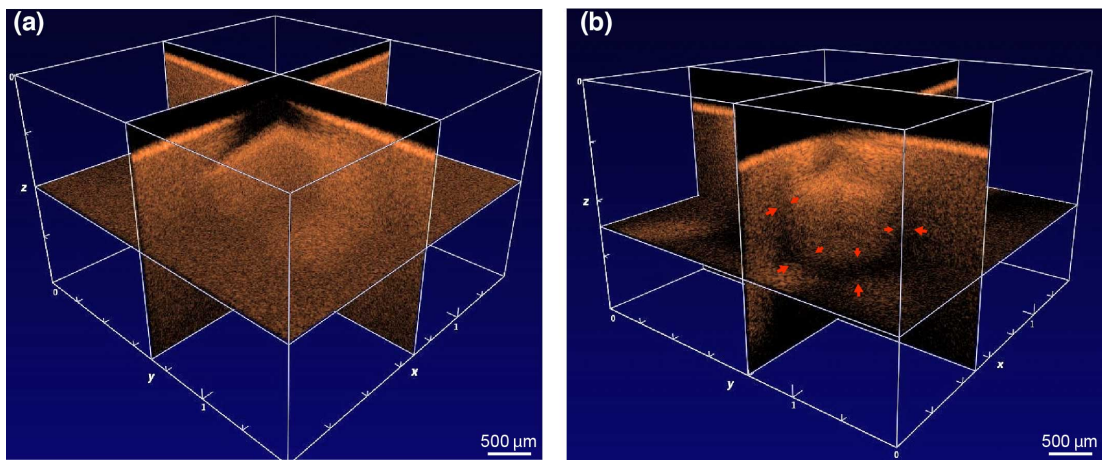


Figure 5.11: Section view of tooth samples obtained with in the OCT system. The dark spots due to carbonization of tissue during 25 kHz uniform repetition rate processing are identified. Processed with (a) 25 pulsed 500 MHz burst mode with burst period of 1 ms and at a scanning velocity of 0.5 mm/s and (b) 25 kHz uniform repetition rate mode at a scanning velocity of 0.5 mm/s.

5.2.2 Experiments at 1.73 GHz intra-burst repetition rate

So far on dentine ablation, results of previous subsection clarify that keeping every parameter the same, except the temporal profile of the pulses, burst mode results in heat effect free micro processing, whereas, corresponding uniform mode causes carbonization. One may argue that, even though there are equal number of pulses per spot, uniformly repeated pulses at 25 kHz should be further optimized in terms of reducing the thermal damage by reducing the repetition rate, in the same time increasing the per pulse energy so that energy per spot stays the same for comparison. Besides, the overall processing time can be reduced with the help of a galvo-scanner, instead of driving a manual stage which has limited velocity. In the light of material processing results (Fig. 4.2. c. and d.) increasing the repetition rate cause a dramatic reduction in ablation threshold per pulse. This issue is also going to be addressed in this subsection in order to understand the possibility of micro processing with hundreds of nano-joules pulse energies. Last, but not least, effects of increasing the burst repetition rate on processing speed will be explained.

A large set of experiments was performed on dentine using uniform and burst modes of the laser to illustrate the effect of ablation cooling. A particular subset of these results are grouped and presented in Table 5.1. These results are chosen due to the possibility of making direct and fair comparisons to each other in pairs, among which key parameters were kept constant.

The first set of experiments aimed to contrast on the depth of ablation between burst and uniform modes without causing any carbonization for both cases. The galvo-scanner was programmed to process a region with 1 mm in diameter. Tightly wound spiral patterns (approximately concentric circles) were scanned 50 times at 10 mm/s velocity and 12.5 μm separation between each circle. With these parameters, 50 % overlap between ablation spots was assured. The total scanning time for overall processing was thus 322 seconds. The details of the parameter sets can be found in Table 5.1 as experiments 5 and 6. The laser operation modes were as follows:

Experiment	Pulse repetition rate	Number of pulses per burst	Burst repetition rate	Pulse energy (μJ)	Burst energy (μJ)	Average power (mW)	Scan speed (mm/s)	Exposure time (s)	Hole diameter (mm)	Average depth (μm)	Ablation speed (mm^3/min)	Comments
1	1728 MHz	400	1 kHz	0.6	240	240	10	320	1	500	0.07	no thermal damage, but slightly lower
2	1728 MHz	200	1 kHz	1.1	210	210	10	320	1	900	0.13	no thermal damage
3	1728 MHz	25	1 kHz	4	100	100	10	320	1	1150	0.17	no thermal damage
4	1 kHz	N/A	N/A	100	N/A	100	10	320	1	240	0.04	no thermal damage
5	1728 MHz	25	1 kHz	2	50	50	10	320	1	800	0.12	no thermal damage
6	1 kHz	N/A	N/A	50	N/A	50	10	320	1	190	0.03	no thermal damage
7	1728 MHz	25	25 kHz	2	50	1250	250	12	1	750	3.0	no thermal damage
8	25 kHz	N/A	N/A	50	N/A	1250	250	12	1	N/A	N/A	stopped early due to carbonisation
9	25 kHz	N/A	N/A	8.8	N/A	220	10	320	1	0	0.00	unable to drill
10	25 kHz	N/A	N/A	12	N/A	306	10	320	1	30	0.004	no thermal damage, but unable to drill
11	25 kHz	N/A	N/A	19	N/A	475	10	320	1	100	0.01	no thermal damage
12	25 kHz	N/A	N/A	50	N/A	1250	10	320	1	N/A	N/A	stopped early due to carbonisation

Table 5.1: Comparison of results for drilling through dentine without active cooling.

- 1.73 GHz intra-burst repetition rate, 25 pulsed burst with 1 kHz burst repetition rate, $2 \mu\text{J}$ /pulse energy equivalent to $50 \mu\text{J}$ /burst energy and 50 mW average power.
- 1 kHz uniformly separated pulses with $50 \mu\text{J}$ /pulse energy equivalent to 50 mW average power.

The optical microscope and depth profile images are given in Fig. 5.12. No carbonization was observed after the processing for both operating modes. Due to creation of 25 times higher electric field (25 times higher intensity) for a single pulse, the edges appear cleaner and sharper for uniform mode of operation, resulting in $190 \mu\text{m}$ depth. On the other hand, the ablation depth is 4 times higher for burst mode, which is $800 \mu\text{m}$. The ablation speed for uniform mode for this parameters is $0.03 \text{ mm}^3/\text{min}$ and $0.12 \text{ mm}^3/\text{min}$ for burst mode.

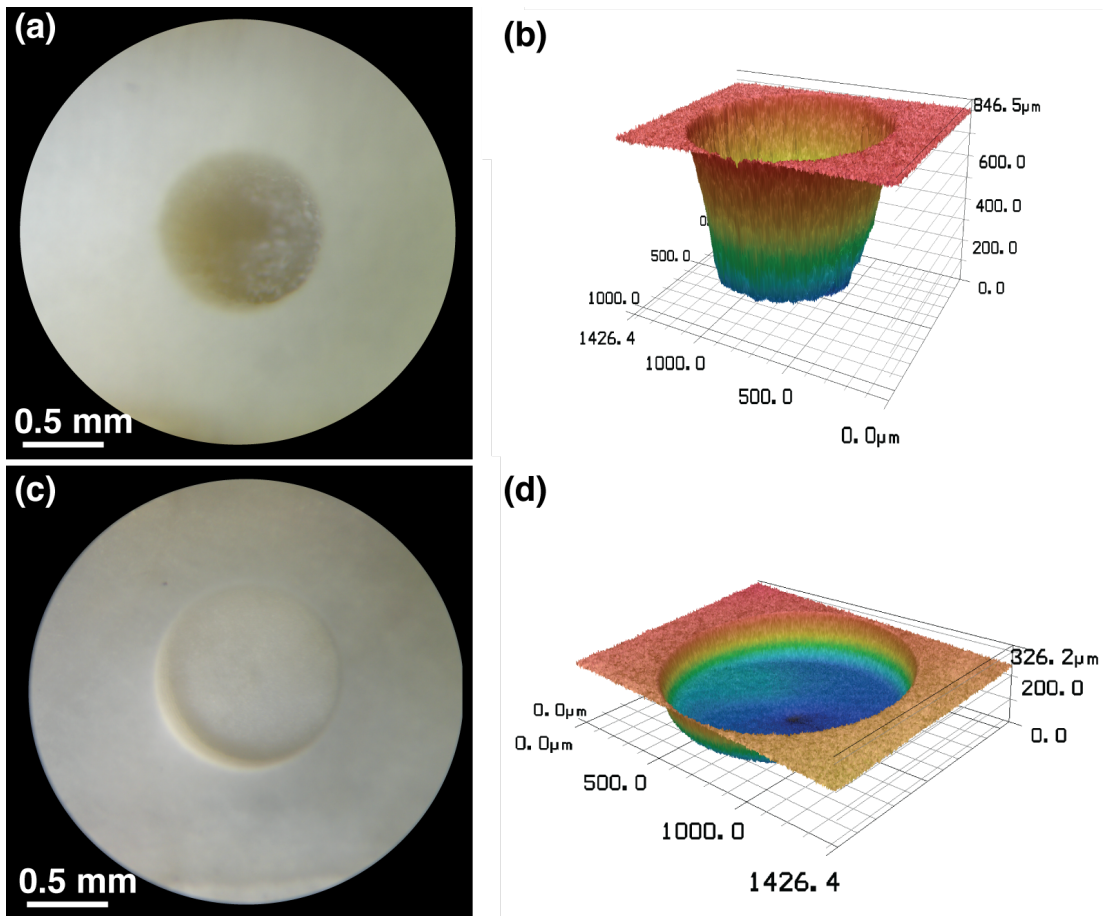


Figure 5.12: Comparison between the effect of burst and uniform modes after processing at low speeds (safe power levels for uniform mode): (a) Optical image of the $\sim 800 \mu\text{m}$ -deep hole drilled in Experiment 5 (using burst mode at 1728 MHz intra-burst repetition rate). (b) LSM image of the same hole. (c) Optical image of the $\sim 200 \mu\text{m}$ -hole drilled in Experiment 6 (using uniform mode at 1 kHz repetition rate). (d) LSM image of the same hole. The processing results for uniform mode have excellent quality, when the repetition rate and average power are low enough. It is also important to note that the burst mode is at least 4 times more efficient despite using 25 times less energetic pulses.

A similar experiment was also performed with twice as much average power, where the details of the parameter sets can be found in Table 5.1 as experiments 3 and 4. The laser operation modes were as follows:

- 1.73 GHz intra-burst repetition rate, 25 pulsed burst with 1 kHz burst repetition rate, 4 μJ /pulse energy equivalent to 100 μJ /burst energy and 100 mW average power.
- 1 kHz uniformly separated pulses with 100 μJ /pulse energy equivalent to 100 mW average power.

The optical microscope and depth profile images are given in Fig. 5.13. No carbonization was observed after the processing for both operating modes. Uniform mode resulted in 240 μm depth. On the other hand, the ablation depth is 5 times higher for burst mode, which is 1150 μm . The ablation speed for uniform mode for this parameters is 0.04 mm^3/min and 0.17 mm^3/min for burst mode.

Additional high-resolution imaging of the edges of the holes drilled in Experiment 3 is provided in Fig. 5.14, obtained using laser scanning microscopy (LSM). Other experiments using burst mode resulted in similar edge qualities. In addition, scanning electron microscopy (SEM) image of the drilled hole is also shown. However, since a regular-vacuum SEM has been used, which is strictly speaking not compatible with tissue imaging, some chips and cracks occurred during or shortly after the vacuuming stage, several times during the process of image acquisition. These cracks or chips were not present during the optical microscopy or LSM images and did not necessarily occur around the laser-processing parts either, so there is no reason to think that they indicate any reduction of mechanical robustness as a result of laser processing.

It is highly instructive to compare, using Table 5.1, Experiments 5 (with burst mode) and 6 (with uniform mode) (Fig. 5.12). In these experiments, the average power incident on the samples was identical. The repetition rate of the uniform pulses and the bursts were the same (1 kHz), meaning that total energy of each burst was given as a single pulse in the uniform mode. Despite using 25 times

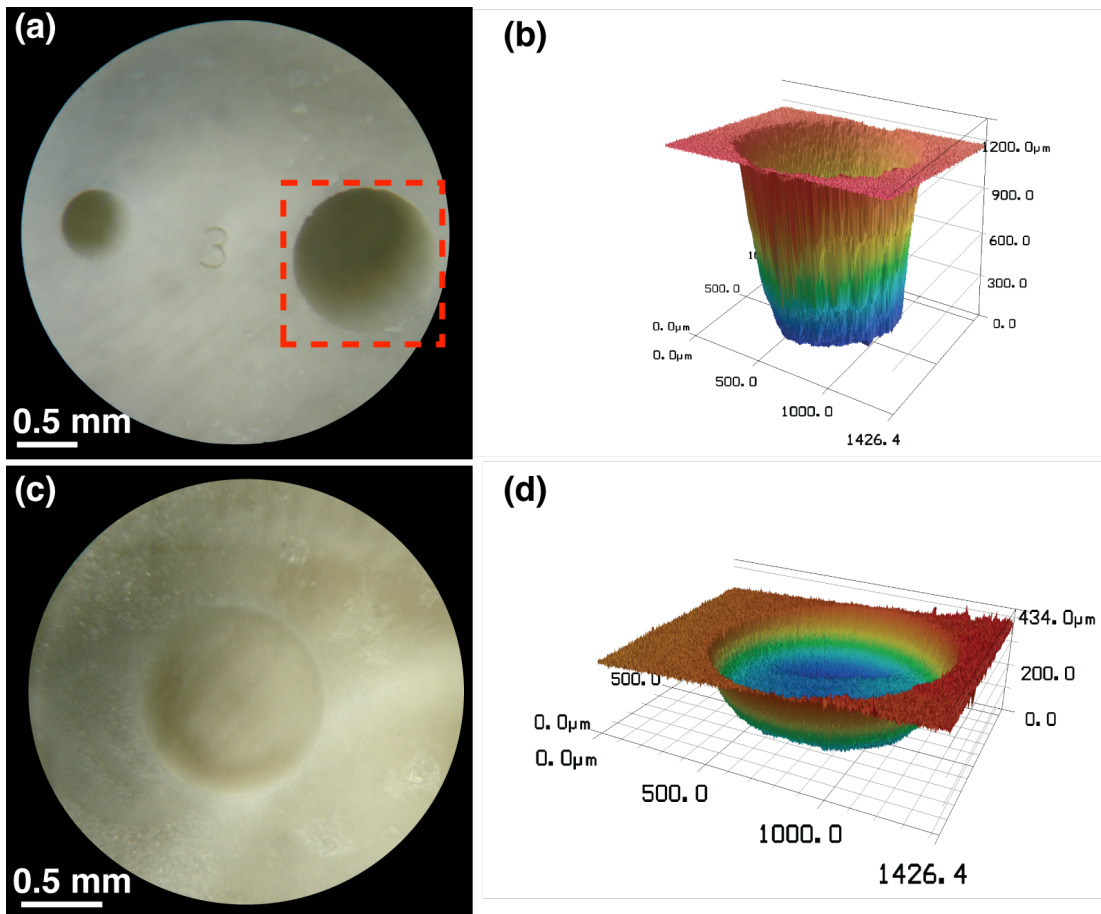


Figure 5.13: Comparison between the effect of burst and uniform modes after processing at low speeds (safe power levels for uniform mode): (a) Optical image of the $\sim 1200 \mu\text{m}$ -deep hole drilled in Experiment 3 (using burst mode at 1728 MHz intra-burst repetition rate). (b) LSM image of the same hole. (c) Optical image of the $\sim 250 \mu\text{m}$ -hole drilled in Experiment 4 (using uniform mode at 1 kHz repetition rate). (d) LSM image of the same hole. The processing results for uniform mode have excellent quality, when the repetition rate and average power are low enough. It is also important to note that the burst mode is at least 5 times more efficient despite using 25 times less energetic pulses.

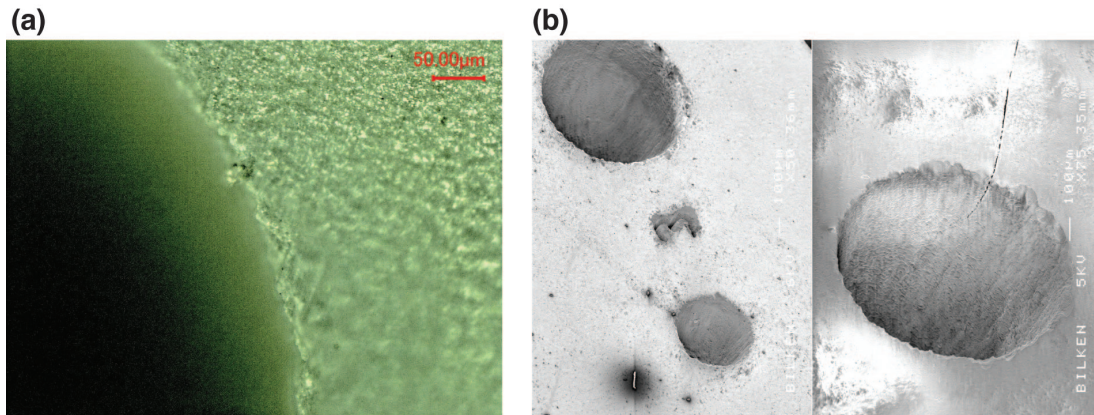


Figure 5.14: Close-up imaging of hole created in Experiment 3. (a) LSM image of the edge of the hole recorded before the SEM imaging. (b) SEM imaging of the hole (compare with the optical microscope image in Fig. 5.13 a. and b.). The chips and crack has occurred during the vacuum formation as required for SEM imaging.

higher pulse energy with the uniform mode, it was outperformed by the burst mode in terms of ablation depth and ablation speed by a factor of 4. A similar outcome emerges based on the comparison between Experiments 3 and 4, as discussed above. The fact that the ablation speed increase is also 4 for a pulse energy difference of 25 times lends further support to the repeat. This is an important result, proving the assertion that the entire burst acts practically like a single pulse (at times, even better) at sufficiently high intra-burst repetition rates. However, it is important not to over-interpret numerical values of the ablation rate comparisons in these experiments, since movement of the focal point, as the holes got deeper, had to be done manually based on checking the plasma emission during ablation. Naturally, one might move slightly slower than optimal, which can result in a slightly shallower hole. Of course, this effect works mostly to the disadvantage of the burst mode, for which the drilling is much faster and it is more likely that the manual focusing is a limiting step. While a major difference is not expected, the ablation speed increase for burst mode by a factor of 4 is likely to be a lower limit.

Another important comparison is between Experiments 7 (with burst mode) and 8 (with uniform mode) (Table 5.1). The average power was again kept the same, but increased compared to the previous cases of Experiments 5 and 6. Since

the scanning speed was proportionately increased, the total energy delivery was kept the same as in Experiments 5 and 6. This particular experiment aimed to overcome this speed limitation due to 1 kHz burst repetition rate, and both the pulse repetition rate in uniform mode and burst repetition rate was increased 25 times, together with the scan velocity (250 mm/s) of the galvo-scanner. Accordingly, the processing time has been reduced to 12 seconds for 50 passes. For this experiment set, the laser operation modes were as follows.

- 1.73 GHz intra-burst repetition rate, 25 pulsed burst with 25 kHz burst repetition rate, 2 μJ /pulse energy equivalent to 50 μJ /burst energy and 1250 mW average power.
- 25 kHz uniformly separated pulses with 50 μJ /pulse energy equivalent to 1250 mW average power.

The optical microscope, LSM depth profile and SEM images are given in Fig. 5.15. The uniform mode led to severe thermal loading of the sample, quite visible carbonization and a strong burning smell, as a result of which the experimented was interrupted before finishing. Under exactly the same conditions, the burst mode successfully completed the processing run, resulting in no indication of thermal damage to the sample and achieving the same ablation depth as in Experiment 5 (Table 5.1). Therefore, with ablation cooling, the ablation rate is increased linearly with burst repetition rate, or average power, without leading to thermal effects, at least up to the average power of 1.25 W. Further increases may be possible, but could not be explored as the laser system is limited to this power level at the present. The sustained ablation speed that has been achieved is a record-high $\sim 3.0 \text{ mm}^3/\text{min}$. In addition to being much higher than previously reported values for femtosecond dentine ablation [9], this result compares favourably to speeds achieved with state-of-the-art dental lasers, which are based purely on thermal effects despite the fact that those laser systems can only be operated if strong water cooling of the target is performed. No active cooling of the samples was performed in the experiments presented here. It appears quite likely that the repetition rate and the ablation rate could be further increased

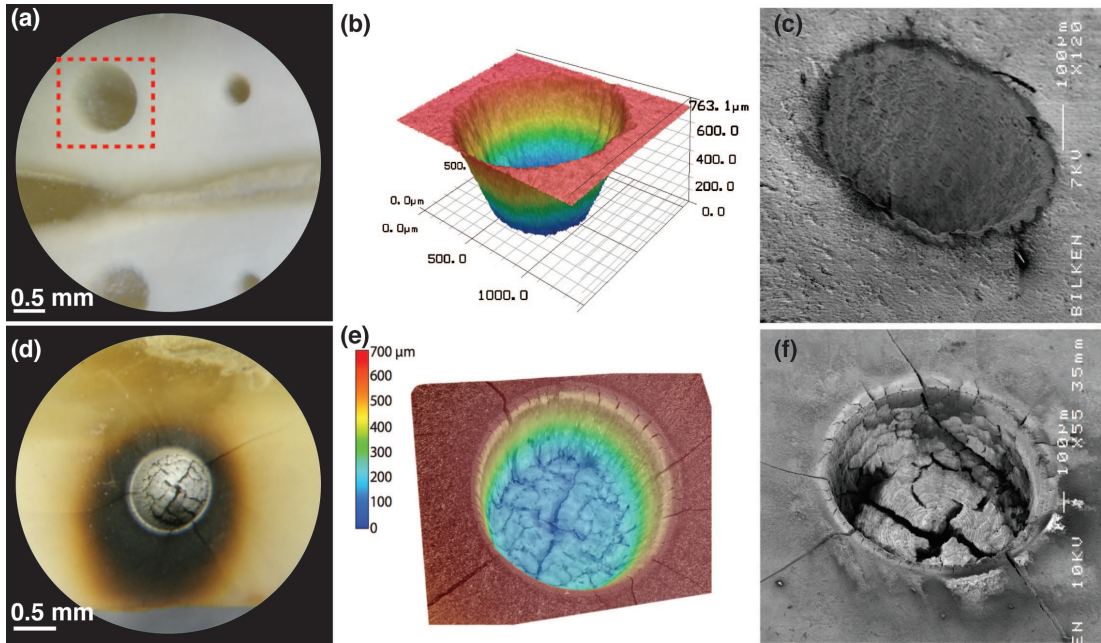


Figure 5.15: Comparison between the effect of burst and uniform modes after processing at high speeds: (a) Optical image of the $\sim 750 \mu\text{m}$ -deep hole drilled in Experiment 7 (using burst mode at 1728 MHz intra-burst repetition rate). (b) LSM image of the same hole. (c) SEM image of the $\sim 750 \mu\text{m}$ -deep hole drilled in Experiment 7 (using burst mode at 1728 MHz intra-burst repetition rate). (d) Optical image of the hole drilled in Experiment 8 (uniform mode at 25 kHz repetition rate). (e) LSM image of the same hole. (f) SEM image of the aborted drilling experiment (Experiment 8), using uniform mode at 25 kHz repetition rate. The experiment was aborted due to excessive carbonisation. These results show that despite using same average powers and delivering same total amount of energy, burst mode is able to successfully drill dentine without any apparent heat damage, whereas uniform mode results in excessive thermal damage.

without suffering from thermal damage, but the laser system was not able to provide higher average power (on sample).

These experimental results confirm several points. As it is well known, it is possible to achieve excellent ablation on tissue using the uniform mode, but there is an upper limit to the average power, therefore the ablation speed. Hence, when a certain average power is exceeded, thermal damage occurs even with ultrafast pulses. With the influence of ablation cooling, this limit is much increased. Of course, this thermal damage limit can be increased with different scanning methods or active cooling of the sample, but such remedies should benefit the burst mode equally and should not change the main conclusion drawn here. Furthermore, at a given average power level, the ablation effectiveness of burst mode is much more than uniform mode, even when using lower pulse energies.

In order to further support the claims immediately above, also contrast Experiment 5 and Experiment 7, where only the repetition rate and scanning speed (i.e., decreasing processing time) are changed by a factor of 25. It is seen that the ablation depth remains the same, meaning that the ablation rate is increased by also 25 times. In other words, at least within the limits tested here, ablation rate scales linearly with power for ablation-cooled tissue removal and that there is significant potential for further scaling. Doing the same scaling comparison between Experiment 6 and Experiment 8 shows, as discussed above, that scaling is severely limited for uniform mode by the onset of thermal damage.

Finally, the efficiency per pulse energy comparison has been made. As it has been previously shown in Fig. 4.2. c. and d., per pulse energies can further be reduced as intra burst repetition rate gets higher. In order to make a comparison, two laser modes were applied:

- 1.73 GHz intra-burst repetition rate, 400 pulsed burst with 1 kHz burst repetition rate, $0,6 \mu\text{J}/\text{pulse}$ energy equivalent to $240 \mu\text{J}/\text{burst}$ energy and 240 mW average power.
- 25 kHz uniformly separated pulses with $9.7 \mu\text{J}/\text{pulse}$ energy equivalent to 240

mW average power.

The results are given in Fig. 5.16. With pulse energies as low as 600 nJ, burst mode resulted in much more deeper ($\sim 400 \mu\text{m}$) structure (Fig. 5.16.a.) than uniform mode with $9.7 \mu\text{J}/\text{pulse}$ energy ($\sim 60 \mu\text{m}$) (Fig. 5.16.b.)

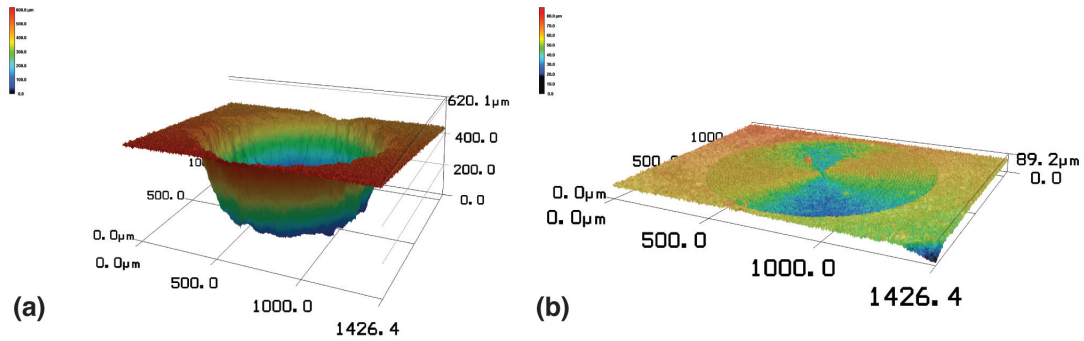


Figure 5.16: Scaling the ablation rate. (a) 400 pulsed-burst mode with 600 nJ/pulse energy at 1 kHz burst repetition rate equivalent to $240 \mu\text{J}/\text{burst}$ energy and 240 mW average power. (b) 25 kHz uniform mode with $9.7 \mu\text{J}/\text{pulse}$ energy equivalent to 240 mW average power. Total scan time = 322 seconds (50 total passes) obtained with 10 mm/s scan speed in order to have 50 % overlap.

Chapter 6

CONCLUSIONS

For a long time, it was commonly assumed that heat effects are nearly completely eliminated through the use of ultrafast pulses. Heat damage can indeed occur during ultrafast pulse processing as a result of pulse-to-pulse accumulation of residual heat that is deposited around the border of the ablated region by each pulse. This, indeed, brings a limitation to ablation rates, especially for biological tissue removal in order to keep the accumulation low. However, to pace up the process, blindly increasing the repetition rate may cause severe heating. While deposition of some residual heat by each pulse is unavoidable, several laser systems has been developed and they were utilized with the aim to catch much of this heat before it can diffuse beyond the volume to be ablated by the next incoming pulse by operating at very high repetition rates. As it has been shown with an analytic model, numerical modeling and experiments to evidence ablation cooling, this idea brings three interrelated advantages: (i) Most of the residual heat left by the previous pulse has not yet diffused out of the volume to be ablated by the next pulse. Thus, each pulse targets an already hot volume, which lowers the required ablation energy and peak power with numerous side benefits, such minimizing plasma shielding, reducing shock wave, cavitation bubble formation and self-focusing. (ii) In addition, the quantity of residual heat is proportional to the pulse energy, thus reducing the magnitude of the problem to be solved. (iii) Finally and most importantly, much of this residual heat is then carried away

from the tissue in the form of ablated matter when ablated by the next pulse, reducing the build-up of heat from pulse to pulse. This is known as ablation cooling, which is very well known in the context of atmospheric entry of shells. In order to benefit from ablation cooling, the repetition rate must exceed a critical value, which scales with the thermal conductivity of the target material, at least tens of MHz.

Given that the minimum pulse energy is substantial, continuous delivery of such repetition rates corresponds to prohibitively high average powers (which can amount to hundreds of watts). To overcome this bottleneck, burst-mode operation has been implemented, which was first demonstrated by R. Marjoribanks, *et. al.* using picosecond solid state lasers [38]. In burst mode, the laser produces packages of high-repetition-rate pulses, or bursts, which are repeated at a much lower, adjustable frequency. All the experiments were utilized with custom built fiber lasers developed in our laboratory, where the details can be found in the Appendix and in Refs. [34–37].

In this thesis, exciting results on processing of a large variety of materials, including copper, silicon, PZT, agar-hydrogel, dentin and brain tissue has been reported. In all cases, burst-mode operation, *i.e.* ablation cooling regime excels. We provided a simple physical explanation which has been supported with parabolic one-step and two-step radiation heating models. Results on non-biological targets are exciting in their own right, required individual pulse energies can be decreased by orders of magnitude, which challenges the accepted paradigm in terms of required pulse parameters. This, in turn, has major implications for the required laser technology. However, results on biological targets are even more exciting, where ablation rates of $\sim 2 \text{ mm}^3/\text{min}$ for brain tissue and $\sim 3 \text{ mm}^3/\text{min}$ for dentin has been achieved with pulse energies as low as $3 \mu\text{J}$ and 600 nJ respectively and offers room for improvement by adjusting the scan and laser parameters further. These results pave the way towards *in vivo* operation at medically relevant speeds, eventually delivered via flexible fibers to hard-to-reach targets. Fiber delivery can further enable combination of tissue processing with simultaneous magnetic resonance imaging (MRI) to be used for precise tissue removal or functional MRI studies. Another advantage of lower pulse energies is to

minimize cavitation bubble formation [8].

The maximum levels of ablation per pulse energy reported using high pulse energies can be attained with much lower pulse energies with optimized burst parameters. Careful analysis of the ablation results on silicon and copper targets reveals several important features. First, in every case tested, burst-mode operation is much more efficient than uniform-mode operation of the laser. The total ablated volumes, e.g., for copper per single pulse burst meet and even exceed the values reported previously using uniform pulsed lasers at much higher fluence levels [74]. In other words, 800 individual pulses making up a 150 microjoule burst ablate roughly as much material as a single 150 microjoule pulse. This changes completely the requirements on laser technology for efficient ultrafast material processing.

In conclusion, a new physical regime of ultrafast laser-material interactions, where heat extraction due to ablation is comparable to heat diffusion has been introduced. Reduction of required pulse energies by three orders of magnitude, while simultaneously increasing the ablation efficiency by an order of magnitude [74] and an order of magnitude faster ablation of brain tissue using nearly two orders of magnitude smaller pulse energies [11] have been presented. These results challenge long-held assumptions regarding ultrafast laser material processing with major implications for simplification, including possibility of using non-traditional laser sources, such as those exhibiting pulsation with double time scales [75]. The basic physics of the proposed method here hint at the possibility of another order of magnitude in reduction of pulse energies and up to two orders of magnitude further increase in ablation rate for tissue. In addition to immediate benefits to numerous and diverse industrial and scientific applications, combination of ablation cooling with fibre-delivery to reach otherwise inaccessible parts of the human body particularly under in-situ magnetic-resonance-imaging guidance, can herald the era of ultrahigh-precision, ultrafast laser-induced version of thermotherapy [76] at medically relevant speeds. A speculative, but exciting future direction is to explore if a suitably sculptured coherent pulse train can coherently enhance nonlinear processes, such as multi-photon transitions, effectively like a single pulse of equivalent energy [77].

Bibliography

- [1] R. R. Gattass and E. Mazur, “Femtosecond laser micromachining in transparent materials,” *Nature Photonics*, vol. 2, pp. 219–225, Apr. 2008.
- [2] W. Yang, P. G. Kazansky, and Y. P. Svirko, “Non-reciprocal ultrafast laser writing,” *Nature Photonics*, vol. 2, pp. 99–104, Feb. 2008.
- [3] J. D. Steinmeyer, C. L. Gilleland, C. Pardo-Martin, M. Angel, C. B. Rohde, M. A. Scott, and M. F. Yanik, “Construction of a femtosecond laser microsurgery system,” *Nature Protocols*, vol. 5, no. 3, pp. 395–407, 2010.
- [4] A. Plech, V. Kotaidis, M. Lorenc, and J. Boneberg, “Femtosecond laser near-field ablation from gold nanoparticles,” *Nature Physics*, vol. 2, no. 1, pp. 44–47, 2006.
- [5] A. Rousse, C. Rischel, S. Fourmaux, I. Uschmann, S. Sebban, G. Grillon, P. Balcou, E. Foster, J. P. Geindre, P. Audebert, J. C. Gauthier, and D. Hulin, “Non-thermal melting in semiconductors measured at femtosecond resolution,” *Nature*, vol. 410, no. 6824, pp. 65–68, 2001.
- [6] S. H. Chung and E. Mazur, “Surgical applications of femtosecond lasers,” *Journal of Biophotonics*, vol. 2, pp. 557–572, Oct. 2009.
- [7] M. F. Yanik, H. Cinar, H. N. Cinar, A. D. Chisholm, Y. S. Jin, and A. Ben-Yakar, “Neurosurgery - Functional regeneration after laser axotomy,” *Nature*, vol. 432, no. 7019, pp. 822–822, 2004.

- [8] T. Juhasz, F. H. Loesel, R. M. Kurtz, C. Horvath, J. F. Bille, and G. Mourou, “Corneal refractive surgery with femtosecond lasers,” *IEEE Journal of Selected Topics in Quantum Electronics*, vol. 5, no. 4, pp. 902–910, 1999.
- [9] J. Serbin, T. Bauer, C. Fallnich, A. Kasenbacher, and W. H. Arnold, “Femtosecond lasers as novel tool in dental surgery,” *Applied Surface Science*, vol. 197, pp. 737–740, 2002.
- [10] C. L. Hoy, O. Ferhanoglu, M. Yildirim, K. H. Kim, S. S. Karajanagi, K. M. C. Chan, J. B. Kobler, S. M. Zeitels, and A. Ben-Yakar, “Clinical Ultrafast Laser Surgery: Recent Advances and Future Directions,” *IEEE Journal of Selected Topics in Quantum Electronics*, vol. 20, pp. 242–255, Apr. 2014.
- [11] F. H. Loesel, J. P. Fischer, M. H. Gotz, C. Horvath, T. JUHASZ, F. Noack, N. Suhm, and J. F. Bille, “Non-thermal ablation of neural tissue with femtosecond laser pulses,” *Applied Physics B: Lasers and Optics*, vol. 66, pp. 121–128, Jan. 1998.
- [12] B. N. Chichkov, C. Momma, S. Nolte, F. Alvensleben, and A. Tunnermann, “Femtosecond, picosecond and nanosecond laser ablation of solids,” *Applied Physics A Materials Science & Processing*, vol. 63, pp. 109–115, Aug. 1996.
- [13] M. E. Fermann and I. Hartl, “Ultrafast fibre lasers,” *Nature Photonics*, vol. 7, pp. 868–874, Nov. 2013.
- [14] C. Xu and F. W. Wise, “Recent advances in fibre lasers for nonlinear microscopy,” *Nature Photonics*, vol. 7, pp. 875–882, Nov. 2013.
- [15] C. Jauregui, J. Limpert, and A. Tuennermann, “High-power fibre lasers,” *Nature Photonics*, vol. 7, pp. 861–867, Nov. 2013.
- [16] U. Keller, “Recent developments in compact ultrafast lasers,” *Nature*, vol. 424, no. 6950, pp. 831–838, 2003.
- [17] F. Bauer, A. Michalowski, T. Kiedrowski, and S. Nolte, “Heat accumulation in ultra-short pulsed scanning laser ablation of metals,” *Optics Express*, vol. 23, pp. 1035–1043, Jan. 2015.

- [18] F. Schelle, S. Polz, H. Haloui, A. Braun, C. Dehn, M. Frentzen, and J. Meister, “Ultrashort pulsed laser (USPL) application in dentistry: basic investigations of ablation rates and thresholds on oral hard tissue and restorative materials,” *Lasers in Medical Science*, vol. 29, pp. 1775–1783, Apr. 2013.
- [19] L. R. Solon, R. Aronson, and G. Gould, “Physiological implications of laser beams.,” *Science*, vol. 134, pp. 1506–1508, Nov. 1961.
- [20] C. J. Campbell, M. C. Rittler, and C. J. Koester, “The optical maser as a retinal coagulator: an evaluation.,” *Transactions - American Academy of Ophthalmology and Otolaryngology. American Academy of Ophthalmology and Otolaryngology*, vol. 67, pp. 58–67, Jan. 1963.
- [21] M. H. Niemz, *Laser-Tissue Interactions . Fundamentals and Applications*, Berlin, Heidelberg: Springer Berlin Heidelberg, 3rd, enlarged edition ed., 2003.
- [22] A. Vogel and V. Venugopalan, “Mechanisms of Pulsed Laser Ablation of Biological Tissues,” *Chemical Reviews*, vol. 103, pp. 577–644, Feb. 2003.
- [23] A. Vogel, J. Noack, G. Hüttman, and G. Paltauf, “Mechanisms of femtosecond laser nanosurgery of cells and tissues,” *Applied Physics B: Lasers and Optics*, vol. 81, pp. 1015–1047, Nov. 2005.
- [24] M. Lenzner, J. Kruger, S. Sartania, Z. Cheng, C. Spielmann, G. Mourou, W. Kautek, and F. Krausz, “Femtosecond Optical Breakdown in Dielectrics,” *Physical Review Letters*, vol. 80, pp. 4076–4079, May 1998.
- [25] F. Docchio, “Lifetimes of Plasmas Induced in Liquids and Ocular Media by Single Nd-Yag Laser-Pulses of Different Duration,” *Europhysics Letters*, vol. 6, no. 5, pp. 407–412, 1988.
- [26] T. Juhasz, X. H. Hu, L. Turi, and Z. Bor, “Dynamics of Shock-Waves and Cavitation Bubbles Generated by Picosecond Laser-Pulses in Corneal Tissue and Water,” *Lasers in Surgery and Medicine*, vol. 15, no. 1, pp. 91–98, 1994.

- [27] P. Schaaf, *Laser Processing of Materials*, vol. 139 of *Fundamentals, Applications and Developments*. Berlin, Heidelberg: Springer Science & Business Media, July 2010.
- [28] W. Steen and J. Mazumder, *Laser Material Processing*. London: Springer Science & Business Media, Nov. 2010.
- [29] R. Viard, A. Emptaz, B. Piron, P. Rochon, B. Wassmer, and S. Mordon, “Determination of the lesion size in Laser-induced Interstitial Thermal Therapy (LITT) using a low-field MRI,” *Conference proceedings : ... Annual International Conference of the IEEE Engineering in Medicine and Biology Society. IEEE Engineering in Medicine and Biology Society. Annual Conference*, vol. 2007, pp. 214–217, 2007.
- [30] J. Wahrburg and K. U. Schmidt, “A multifunctional stereotactic probe for laser-based tumour ablation in neurosurgery,” in *1996 IEEE International Conference on Systems, Man and Cybernetics. Information Intelligence and Systems (Cat. No.96CH35929)*, pp. 2829–2832 vol.4, IEEE, 1996.
- [31] J. Wahrburg and K. U. Schmidt, “A new system for minimal invasive ablation of deep seated brain tumours,” in *Proceedings of the 19th Annual International Conference of the IEEE Engineering in Medicine and Biology Society. 'Magnificent Milestones and Emerging Opportunities in Medical Engineering' (Cat. No.97CH36136)*, pp. 2438–2441, IEEE, 1997.
- [32] C. Kerse, H. Kalaycıoğlu, P. Elahi, B. Çetin, S. Yavaş, D. K. Kesim, O. Akçaalan, M. D. Aşık, B. Öktem, H. Hoogland, R. Holzwarth, and F. O. Ilday, “Ablation-cooled material removal with ultrafast bursts of pulses,” *submitted for publication*, Jan. 2016.
- [33] G. P. Sutton and O. Biblarz, *Rocket propulsion elements; 8th ed.* Hoboken, NJ: Wiley, 2011.
- [34] H. Kalaycıoğlu, K. Eken, and F. O. Ilday, “Fiber amplification of pulse bursts up to 20 μ J pulse energy at 1 kHz repetition rate,” *Optics Letters*, vol. 36, no. 17, pp. 3383–3385, 2011.

- [35] H. Kalaycioglu, Y. B. Eldeniz, O. Akcaalan, S. Yavas, K. Gurel, M. Efe, and F. O. Ilday, “1 mJ pulse bursts from a Yb-doped fiber amplifier,” *Optics Letters*, vol. 37, no. 13, pp. 2586–2588, 2012.
- [36] H. Kalaycioglu, O. Akcaalan, S. Yavas, Y. B. Eldeniz, and F. O. Ilday, “Burst-mode Yb-doped fiber amplifier system optimized for low-repetition-rate operation,” *JOSA B*, vol. 32, pp. 900–906, May 2015.
- [37] C. Kerse, H. Kalaycioglu, P. Elahi, and O. Akcaalan, “3.5-GHz intra-burst repetition rate ultrafast Yb-doped fiber laser,” *Optics Communications*, 2015.
- [38] M. Lapczynya, K. P. Chen, P. R. Herman, H. W. Tan, and R. S. Majoribanks, “Ultra high repetition rate (133 MHz) laser ablation of aluminum with 1.2-ps pulses,” *Applied Physics A Materials Science & Processing*, vol. 69, pp. S883–S886, Dec. 1999.
- [39] W. Hu, Y. C. Shin, and G. King, “Modeling of multi-burst mode picosecond laser ablation for improved material removal rate,” *Applied Physics A Materials Science & Processing*, vol. 98, pp. 407–415, Sept. 2009.
- [40] R. S. Marjoribanks, C. Dille, J. E. Schoenly, L. McKinney, A. Mordovanakis, P. Kaifosh, P. Forrester, Z. Qian, A. Covarrubias, Y. Feng, and L. Lilge, “Ablation and thermal effects in treatment of hard and soft materials and biotissues using ultrafast-laser pulse-train bursts,” *Photonics and Lasers in Medicine*, vol. 1, pp. 1–15, Aug. 2012.
- [41] A. Ancona, F. Röser, K. Rademaker, J. Limpert, S. Nolte, and A. Tunnermann, “High speed laser drilling of metals using a high repetition rate, high average power ultrafast fiber CPA system,” *Optics Express*, vol. 16, pp. 8958–8968, June 2008.
- [42] S. Tadigadapa and K. Mateti, “Piezoelectric MEMS sensors: state-of-the-art and perspectives,” *Measurement Science and Technology*, vol. 20, no. 9, p. 092001, 2009.

- [43] P. S. Tsai, B. Friedman, A. I. Ifarraguerri, B. D. Thompson, V. Lev-Ram, C. B. Schaffer, Q. Xiong, R. Y. Tsien, J. A. Squier, and D. Kleinfeld, “All-Optical Histology Using Ultrashort Laser Pulses,” *Neuron*, vol. 39, pp. 27–41, July 2003.
- [44] M. F. Ashby and K. E. Easterling, “The Transformation Hardening of Steel Surfaces by Laser-Beams .1. Hypo-Eutectoid Steels,” *Acta Metallurgica*, vol. 32, no. 11, pp. 1935–&, 1984.
- [45] T. Q. Qiu and C. L. Tien, “Heat-Transfer Mechanisms During Short-Pulse Laser-Heating of Metals,” *Journal of Heat Transfer-Transactions of the Asme*, vol. 115, pp. 835–841, Nov. 1993.
- [46] F. Vidal, T. W. Johnston, S. Laville, O. Barthélemy, M. Chaker, B. Le Droff, J. Margot, and M. Sabsabi, “Critical-Point Phase Separation in Laser Ablation of Conductors,” *Physical Review Letters*, vol. 86, pp. 2573–2576, Mar. 2001.
- [47] J. K. Chen, W. P. Latham, and J. E. Beraun, “The role of electron–phonon coupling in ultrafast laser heating,” *Journal of laser applications*, vol. 17, no. 1, p. 63, 2005.
- [48] Z. Lin and L. V. Zhigilei, “Temperature dependences of the electron–phonon coupling, electron heat capacity and thermal conductivity in Ni under femtosecond laser irradiation,” *Applied Surface Science*, vol. 253, pp. 6295–6300, May 2007.
- [49] Z. Lin, L. V. Zhigilei, and V. Celli, “Electron-phonon coupling and electron heat capacity of metals under conditions of strong electron-phonon nonequilibrium,” *Physical Review B*, vol. 77, p. 075133, Feb. 2008.
- [50] A. S. Basin, *Basic critical point parameters for metals with close-packed crystalline structure*. Chemistry and Computational Simulation. Butlerov . . . , 2001.
- [51] M. G. Burzo, P. L. Komarov, and P. E. Raad, “Noncontact transient temperature mapping of active electronic devices using the thermorefectance

- method,” *IEEE Transactions on Components and Packaging Technologies*, vol. 28, pp. 637–643, Nov. 2005.
- [52] C. Mitra, A. Banerjee, S. Maity, and N. Turnquist, “An optical method for measuring metal surface temperature in harsh environment conditions,” in *SPIE Photonics Europe* (F. Berghmans, A. G. Mignani, and C. A. van Hoof, eds.), pp. 772619–8, SPIE, May 2010.
- [53] N. Taketoshi, T. Baba, and A. Ono, “Electrical delay technique in the picosecond thermorefectance method for thermophysical property measurements of thin films,” *Review of Scientific Instruments*, vol. 76, no. 9, pp. 094903–9, 2005.
- [54] A. Soni, V. M. Sundaram, and S.-B. Wen, “A methodology for nanosecond (or better) time resolved thermorefectance imaging with coherence control of laser pulses,” *Applied Physics Letters*, vol. 102, no. 20, pp. 203112–4, 2013.
- [55] P. Elahi, S. Yilmaz, Y. B. Eldeniz, and F. O. Ilday, “Generation of picosecond pulses directly from a 100 W, burst-mode, doping-managed Yb-doped fiber amplifier,” *Optics Letters*, vol. 39, pp. 236–239, Jan. 2014.
- [56] S. Yilmaz, P. Elahi, H. Kalaycıoğlu, and F. O. Ilday, “Amplified spontaneous emission in high-power burst-mode fiber lasers,” *JOSA B*, vol. 32, pp. 2462–2466, Dec. 2015.
- [57] R. Knappe, H. Haloui, A. Seifert, A. Weis, and A. Nebel, “Scaling ablation rates for picosecond lasers using burst micromachining,” in *LASE* (W. Pfleging, Y. Lu, K. Washio, J. Amako, and W. Hoving, eds.), pp. 75850H–75850H–6, SPIE, Feb. 2010.
- [58] A. Borowiec and H. K. Haugen, “Femtosecond laser micromachining of grooves in indium phosphide,” *Applied Physics A Materials Science & Processing*, vol. 79, no. 3, pp. 521–529, 2004.
- [59] H. Huang, L.-M. Yang, and J. Liu, “Micro-hole drilling and cutting using femtosecond fiber laser,” *Optical Engineering*, vol. 53, pp. 051513–051513, May 2014.

- [60] T. Morita, “Miniature piezoelectric motors,” *Sensors and Actuators a-Physical*, vol. 103, no. 3, pp. 291–300, 2003.
- [61] F. S. Foster, C. J. Pavlin, G. R. Lockwood, L. K. Ryan, K. A. Harasiewicz, L. Berube, and A. M. Rauth, “Principles and Applications of Ultrasound Backscatter Microscopy,” *Ieee Transactions on Ultrasonics Ferroelectrics and Frequency Control*, vol. 40, pp. 608–617, Sept. 1993.
- [62] D. W. Zeng, K. Li, K. C. Yung, H. L. W. Chan, C. L. Choy, and C. S. Xie, “UV laser micromachining of piezoelectric ceramic using a pulsed Nd:YAG laser,” *Applied Physics A Materials Science & Processing*, vol. 78, no. 3, pp. 415–421, 2004.
- [63] Y. Di Maio, J. P. Colombier, P. Cazottes, and E. Audouard, “Ultrafast laser ablation characteristics of PZT ceramic: Analysis methods and comparison with metals,” *Optics and Lasers in Engineering*, vol. 50, pp. 1582–1591, Nov. 2012.
- [64] D. Wajima, M. Nakamura, K. Horiuchi, Y. Takeshima, F. Nishimura, and H. Nakase, “Cilostazol minimizes venous ischemic injury in diabetic and normal rats,” *Journal of Cerebral Blood Flow & Metabolism*, vol. 31, pp. 2030–2040, Apr. 2011.
- [65] L. Ling, J. Zeng, Z. Pei, R. T. Cheung, Q. Hou, S. Xing, and S. Zhang, “Neurogenesis and angiogenesis within the ipsilateral thalamus with secondary damage after focal cortical infarction in hypertensive rats,” *Journal of Cerebral Blood Flow & Metabolism*, vol. 29, pp. 1538–1546, June 2009.
- [66] F. Liu, D. Sag, J. Wang, L. M. Shollenberger, F. Niu, X. Yuan, S.-D. Li, M. Thompson, and P. Monahan, “Sine-wave Current for Efficient and Safe In Vivo Gene Transfer,” *Molecular Therapy*, vol. 15, pp. 1842–1847, July 2007.
- [67] J. Kozub, B. Ivanov, A. Jayasinghe, R. Prasad, J. Shen, M. Klosner, D. Heller, M. Mendenhall, D. W. Piston, K. Joos, and M. S. Hutson, “Raman-shifted alexandrite laser for soft tissue ablation in the 6- to 7- μm

- wavelength range,” *Biomedical Optics Express*, vol. 2, pp. 1275–1281, May 2011.
- [68] U. Ziegler and P. Groscurth, “Morphological Features of Cell Death,” *Physiology*, vol. 19, pp. 124–128, June 2004.
- [69] P. B. Dervan, “Design of Sequence-Specific Dna-Binding Molecules,” *Science*, vol. 232, no. 4749, pp. 464–471, 1986.
- [70] J. L. Drury and D. J. Mooney, “Hydrogels for tissue engineering: scaffold design variables and applications,” *Biomaterials*, vol. 24, pp. 4337–4351, Nov. 2003.
- [71] M. E. Phelps, E. J. Hoffman, and M. M. Ter-Pogossian, “Attenuation coefficients of various body tissues, fluids, and lesions at photon energies of 18 to 136 keV.,” *Radiology*, vol. 117, pp. 573–583, Dec. 1975.
- [72] B. Choi and A. J. Welch, “Analysis of thermal relaxation during laser irradiation of tissue,” *Lasers in Surgery and Medicine*, vol. 29, no. 4, pp. 351–359, 2001.
- [73] A. A. Oraevsky, L. B. Da Silva, A. M. Rubenchik, M. D. Feit, M. E. Glinsky, M. D. Perry, B. M. Mammini, W. Small, and B. C. Stuart, “Plasma mediated ablation of biological tissues with nanosecond-to-femtosecond laser pulses: relative role of linear and nonlinear absorption,” *IEEE Journal of Selected Topics in Quantum Electronics*, vol. 2, no. 4, pp. 801–809, 1996.
- [74] M. Hashida, A. F. Semerok, O. Gobert, G. Petite, Y. Izawa, and J. F. Wagner, “Ablation threshold dependence on pulse duration for copper,” *Applied Surface Science*, vol. 197-198, pp. 862–867, Sept. 2002.
- [75] S. Kobtsev, S. Smirnov, S. Kukarin, and S. Turitsyn, “Mode-locked fiber lasers with significant variability of generation regimes,” *Optical Fiber Technology*, vol. 20, pp. 615–620, Dec. 2014.

- [76] F. Streitparth, G. Knobloch, D. Balmert, S. Chopra, J. Rump, U. Wonneberger, C. Philipp, B. Hamm, and U. Teichgräber, “Laser-induced therapy (LITT)—evaluation of a miniaturised applicator and implementation in a 1.0-T high-field open MRI applying a porcine liver model,” *European Radiology*, vol. 20, pp. 2671–2678, June 2010.
- [77] D. Meshulach and Y. Silberberg, “Coherent quantum control of two-photon transitions by a femtosecond laser pulse,” *Nature*, vol. 396, pp. 239–242, Nov. 1998.
- [78] A. Chong, J. Buckley, W. Renninger, and F. Wise, “All-normal-dispersion femtosecond fiber laser,” *Optics Express*, vol. 14, pp. 10095–10100, Oct. 2006.
- [79] F. O. Ilday, H. Lim, J. R. Buckley, and F. W. Wise, “Practical all-fiber source of high-power, 120-fs pulses at 1 μm ,” *Optics Letters*, vol. 28, pp. 1362–1364, Aug. 2003.
- [80] B. Oktem, C. Ülgüdür, and F. O. Ilday, “Soliton-similariton fibre laser,” *Nature Photonics*, vol. 4, pp. 307–311, May 2010.
- [81] J. W. Nicholson, J. Jasapara, W. Rudolph, F. G. Omenetto, and A. J. Taylor, “Full-field characterization of femtosecond pulses by spectrum and cross-correlation measurements,” *Optics Letters*, vol. 24, pp. 1774–1776, Dec. 1999.
- [82] T. H. R. Crawford, A. Borowiec, and H. K. Haugen, “Femtosecond laser micromachining of grooves in silicon with 800 nm pulses,” *Applied Physics A Materials Science & Processing*, vol. 80, no. 8, pp. 1717–1724, 2005.
- [83] M. Abramowitz and I. A. Stegun, “Handbook of mathematical functions,” 1965.
- [84] B. S. Thurow, A. Satija, and K. Lynch, “Third-generation megahertz-rate pulse burst laser system,” *Applied Optics*, vol. 48, no. 11, pp. 2086–2093, 2009.
- [85] D. J. Den Hartog, J. R. Ambuel, M. T. Borchardt, A. F. Falkowski, W. S. Harris, D. J. Holly, E. Parke, J. A. Reusch, P. E. Robl, H. D. Stephens,

- and Y. M. Yang, “Pulse-burst laser systems for fast Thomson scattering (invited),” *Review of Scientific Instruments*, vol. 81, Oct. 2010.
- [86] I. Will, H. I. Templin, S. Schreiber, and W. Sandner, “Photoinjector drive laser of the FLASH FEL,” *Optics Express*, vol. 19, no. 24, pp. 23770–23781, 2011.
- [87] J. Bonse, S. Baudach, J. Kruger, W. Kautek, and M. Lenzner, “Femtosecond laser ablation of silicon-modification thresholds and morphology,” *Applied Physics A Materials Science & Processing*, vol. 74, pp. 19–25, Jan. 2002.
- [88] D. J. Hwang, C. P. Grigoropoulos, and T. Y. Choi, “Efficiency of silicon micromachining by femtosecond laser pulses in ambient air,” *Journal of applied physics*, vol. 99, no. 8, 2006.
- [89] J. Byskov-Nielsen, J.-M. Savolainen, M. S. Christensen, and P. Balling, “Ultra-short pulse laser ablation of metals: threshold fluence, incubation coefficient and ablation rates,” *Applied Physics A Materials Science & Processing*, vol. 101, pp. 97–101, Oct. 2010.
- [90] W. M. Rohsenow, J. P. Hartnett, and Y. I. Cho, *Handbook of heat transfer*. McGraw-Hill, May 1998.
- [91] P. Wu, W. L. Lempert, and R. B. Miles, “Megahertz Pulse-Burst Laser and Visualization of Shock-Wave/Boundary-Layer Interaction,” *AIAA journal*, vol. 38, pp. 672–679, Apr. 2000.
- [92] Z. Qian, A. Mordovanakis, J. E. Schoenly, A. Covarrubias, Y. Feng, L. Lilge, and R. S. Marjoribanks, “Pulsetrain-burst mode, ultrafast-laser interactions with 3D viable cell cultures as a model for soft biological tissues,” *Biomedical Optics Express*, vol. 5, no. 1, pp. 208–15, 2014.

Appendix A

Burst Mode Laser Systems

A.1 1 MHz - 3.5 GHz intra-burst repetition rate, 1 ps pulse duration

The experimental setup in Fig. A.1 consists of an all-normal dispersion (ANDi) laser oscillator [78] which generates a mode-locked signal at a repetition rate of 108 MHz as the seed source. The signal from the oscillator is converted to 3.5 GHz by a six-stage cascaded repetition rate multiplier and a devoted preamplifier at the end of the couplers, before seeding six stages of core-pumped fiber pre-amplifiers, a three-stage double-clad (DC) fiber power amplifier as well as synchronized pulse picking and pulsed-pumping electronics. The overall, all-fiber master-oscillator power-amplifier (MOPA) Yb-fiber architecture is based on the design in [79]. The first three stages of pre-amplifiers utilize continuous pumping while the latter three, which are positioned after the acousto-optic modulator (AOM), incorporate pulsed pumping. The 108-MHz fiber oscillator outputs ~ 22 mW with a spectrum 20 nm wide and centered at 1030 nm.

The repetition rate multiplier consists of cascaded 3 dB couplers, where for each coupler there is a length difference between the two output arms equivalent to a delay of one period of the signal repetition rate at input of that coupler.

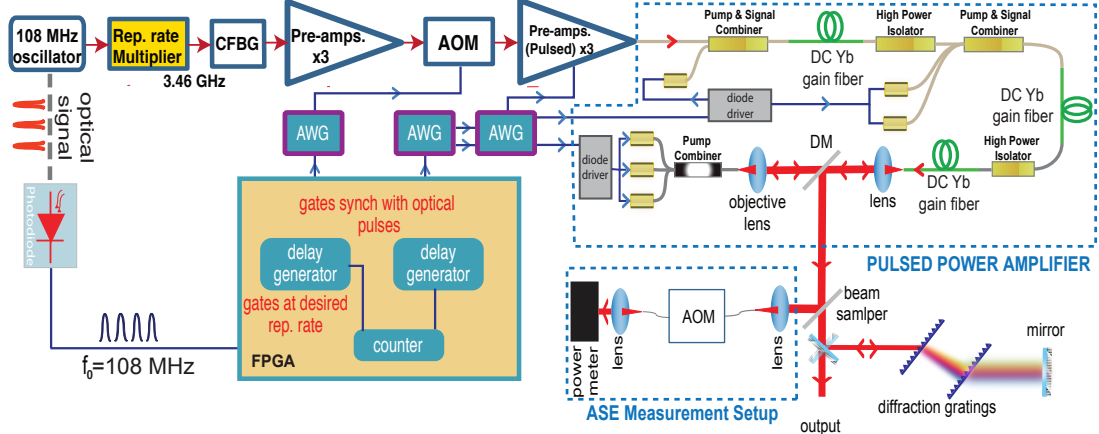


Figure A.1: Schematic diagram of the experimental setup. CFBG: chirped fiber bragg grating, AOM: acousto-optical modulator, AWG: arbitrary waveform generator, FPGA: field programmable gate array, DM: dichroic mirror, WDM: wavelength division multiplexer, PBS: polarizing beam splitter, PPF: pump protection filter, SM: single-mode, DC: double-clad.

Therefore, the repetition rate is doubled at each stage beginning with the second coupler and in this case with six cascaded couplers, it is multiplied by 2^5 , from 108 MHz to 3.5 GHz. After six couplers, the signal (7.5 mW) is polarized by a polarization beam splitter (PBS) after a polarization controller and amplified to about 300 mW, before entering the pulse stretcher. After the PBS, the system only consists of polarization maintaining (PM) components.

The seed pulses are stretched to about 2 ns in a chirped-fiber-bragg-grating (CFBG) designed to match a compressor consisting of a pair 1800 lines/mm transmission gratings with a separation of 70 cm at an incidence angle of 69° . The seed signal drops below 50 mW and the spectrum is ~ 15 nm wide at the output of the pulse stretching unit made of a circulator and the CFBG. Thereafter, it is amplified by three stages of preamplifiers to above 1 W before entering the AOM. The pulse picking and pulse pumping processes are both synchronized with 108 MHz oscillator where FPGA circuit delivers the trigger signals to Arbitrary Waveform Generators (AWG), which drive the AOM and diode drivers. This electronic configuration enables us to adjust burst duration and the burst repetition frequency on demand. The AOM, which imprints the desired pulse burst envelope onto the signal has rise and fall times of 6 and 8 ns, respectively.

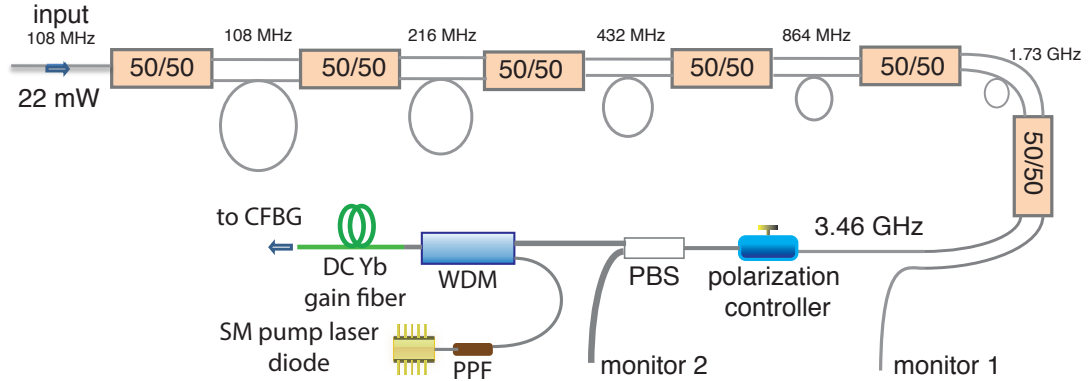


Figure A.2: Repetition Rate Multiplier of Fig. A.1. CFBG: chirped fiber bragg grating, WDM: wavelength division multiplexer, PBS: polarizing beam splitter, PPF: pump protection filter, SM: single-mode, DC: double-clad, 50/50: 50 % coupler.

With the AOM imposing bursts repeated at kHz level, the duty cycle of the signal drops sharply to 0.01% level, hence, the bursts are amplified in six stages of pulsed amplification. Comparatively short gain fibers are used in the three-stage pulsed preamplifier following the AOM to suppress ASE generation. The power amplifier at the end of the system consists of three stages also, first two forward-pumped and final one backward-pumped, which employ one, two and three 25-W pump diodes, respectively. The three stages contain Yb-1200-DC-20/125PM (nLight, Inc.) as gain fiber with lengths shorter than that required for high efficiency in continuous pumping regime. Further details on the amplifier system and the electronic control and synchronization unit can be found in Ref. [36].

After optimization of all the signal durations and frequencies, the system is able to amplify 15 ns long 50-pulsed bursts to a net energy of 215 μJ at burst repetition rate of 1 kHz. This is the shortest possible burst duration allowed by the time response of the AOM, and therefore burst pre-shaping was not possible. Hence, an electronic gate in the form of a 15 ns wide rectangular pulse applied to the AOM results in the burst shape seen in Fig. A.3(a) with a Gaussian-like pulse distribution and nearly 15 ns duration, where, the optical spectrum of this 15 ns long burst mode output is given in Fig. A.3(b). The maximum and average pulse energy inside the burst is calculated to be 8.4 μJ and 4.4 μJ , respectively.

System is also able to produce 230 ns long 800-pulsed bursts at a net energy of $490\mu\text{J}$. The recorded pulse train for 230 ns long burst in Fig. A.3(a) displays a much more uniform energy distribution compared to 15 ns long burst, due to the presence of pre-shaping, in this case. In this case, the maximum and the average pulse energy inside 230 ns-long burst is calculated as $1.1\mu\text{J}$ and $0.56\mu\text{J}$, respectively. 50% and 20% ASE content of the signal was measured for 15 ns and 230 ns long bursts, respectively, indicating the exponential growth of ASE [36] since identical pump pulses are used in each case. Actually, higher per pulse energies can be extracted by using the earlier stages of the rep. rate multiplier, hence, reducing the in-burst repetition rate. So, easily, pulse energies above $10\mu\text{J}$ can be obtained, where, up to $16\mu\text{J}$ pulses can be compressed below pico-second, which is shown in Fig. A.3(c) indicating the FWHM of 800 fs.

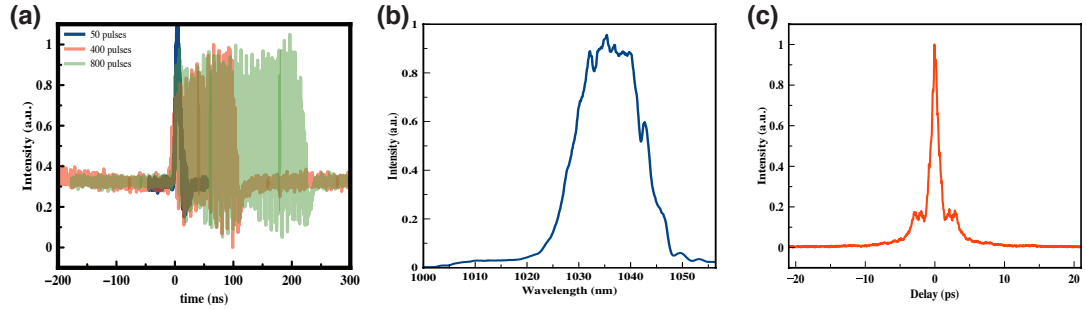


Figure A.3: (a) Pulse trains of amplified bursts: 15 ns long burst with 50 pulses, 130 ns long burst with 400 pulses and 230 ns long burst with 800 pulses. Due to the band-width limitation of the diagnostics, the pulses inside bursts are unresolvable. (b) Optical spectrum of burst output with 230 ns burst duration. (c) Autocorrelation result for compressed pulses at $16\mu\text{J}$ after pulsed power amplifier stage.

The intensity and period uniformity of the 3.5 GHz seed signal are shown in Fig. A.4(a), top and bottom panels, respectively, for a train of 32 (2^5) pulses, which constitute one full cycle of the repeated pulse train from the six-stage multiplier. The average values and standard deviation were calculated as 0.92 and 0.03 for normalized intensity, and 285.34 ps and 9.4 ps for repetition period, respectively. The RF spectrum of the seed signal is given in Fig. A.4(b). The bottom panel indicates the main repetition frequency of 3.45 GHz and its harmonics, where top panel gives a close up view on the main frequency for a span of 10 kHz and with a resolution of 20 Hz. In Fig. A.4(c), the recorded RF

spectra of the amplified burst train over a span of 20 MHz, centered at 3.4549 GHz, displays the comb generated by the burst system. Hence, the frequency domain representation of a train of 230 ns long pulse bursts repeated at 1 kHz, constitutes a comb with 1 kHz internal spacing (close up view in top panel of Fig. A.4(c)), under an envelope with 3dB band-width of ~ 4 MHz (bottom panel of Fig. A.4(c)) determined by the temporal shape of the burst. Note that the comb lines are actually much denser than as displayed in the figure, which is due to the finite number of sample points that the spectrum analyzer (FSUP26, Rohde & Schwarz) can record.

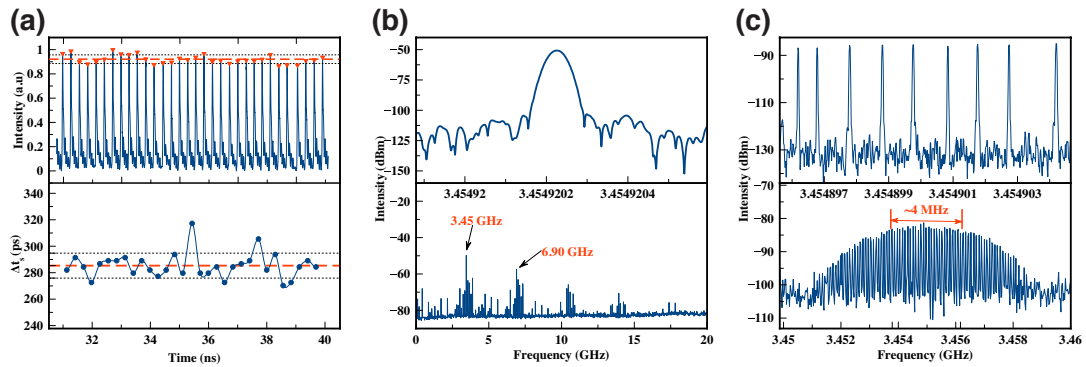


Figure A.4: (a) Intensity (top) and pulse separation time (bottom) variability of the 3.5 GHz oscillator output. (b) Measured RF spectrum of the 3.5 GHz seed signal. Highly resolved 10 KHz span around the center frequency (top). 20 GHz span showing the frequency components and the harmonics (bottom). (c) Measured RF spectrum of 230 ns long bursts repeated at 1 kHz: Frequency span of 20 MHz centered at 3.455 GHz (bottom), close up 1 kHz lines with a span of 10 kHz versus frequency offset from the central frequency of 3.455 GHz, with a resolution band-width of 30 Hz (top).

The detailed analysis of the system explained here can be found in Ref. [37].

A.2 22.3 MHz intra-burst repetition rate, 300 fs pulse duration

The experimental setup is depicted in Fig. A.5. The seed pulses originate from a Yb-doped fiber oscillator operating in the all-normal dispersion regime at a

repetition rate of 22.3 MHz. Mode-locking is initiated and stabilized by nonlinear polarization evolution. The oscillator generates 4-nJ (80 mW) pulses centered at 1037 nm with a spectral width of 15 nm (Fig. A.6(a)) and seeds a 100 m-long polarization-maintaining (PM) fiber stretcher. The seed pulses are thus stretched to 55 ps. This is followed by an in-line fiber pre-amplifier (Yb1200-6/125DC-PM, Liekki), which boosts the signal level to 500 mW. The repetition rate is either reduced to a uniform value of 200 kHz or bursts of pulses are produced at 50 kHz (Fig. A.6(b)) in a fiber-coupled acousto-optic modulator (AOM). After the AOM, the power is reduced to 2 mW. The AOM is controlled by a special FPGA-based (SPARTAN 3E, Xilinx) electronic circuitry developed in house for synchronous pulse picking, burst formation and acts as a master controller for the entire system.

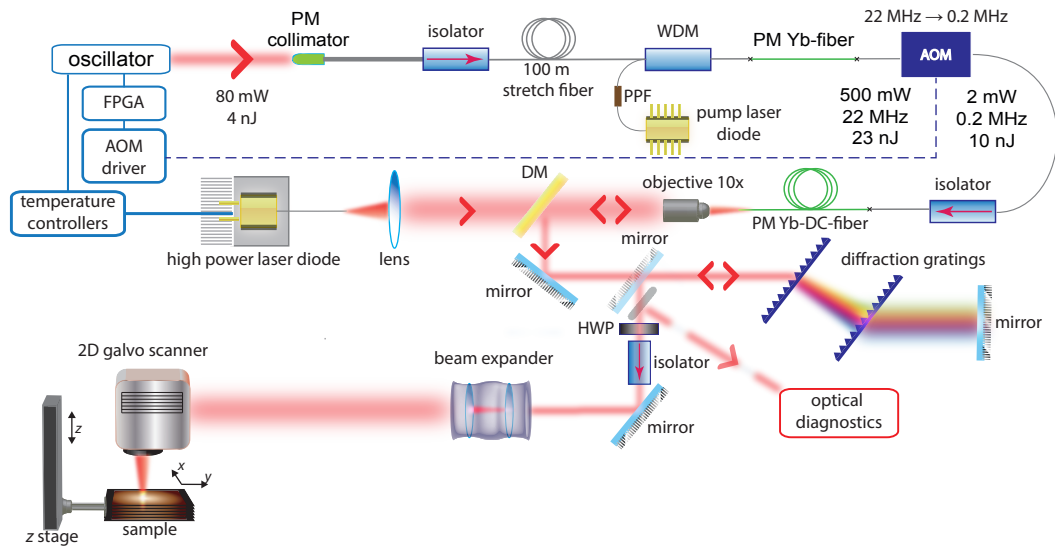


Figure A.5: Schematic diagram of the laser and tissue processing setups; PM, polarization maintaining; PPF, pump protection filter; WDM, wavelength division multiplexer; DC, double clad; DM, Dichroic Mirror; HWP, half-wave plate.

At the power amplifier stage, the setup consists of a 10-W pump diode stabilized to 976 nm by temperature control, a short section of double-clad highly doped Yb gain fiber with core diameter of 20 μm , cladding of 125 μm and optics for backward pumping (Yb1200-20/125DC-PM, Liekki). This configuration minimizes the nonlinear effects. Nearly 75% of the pump power is coupled into the gain fiber with a collimating lens of 25 mm focal length and a 10x objective.

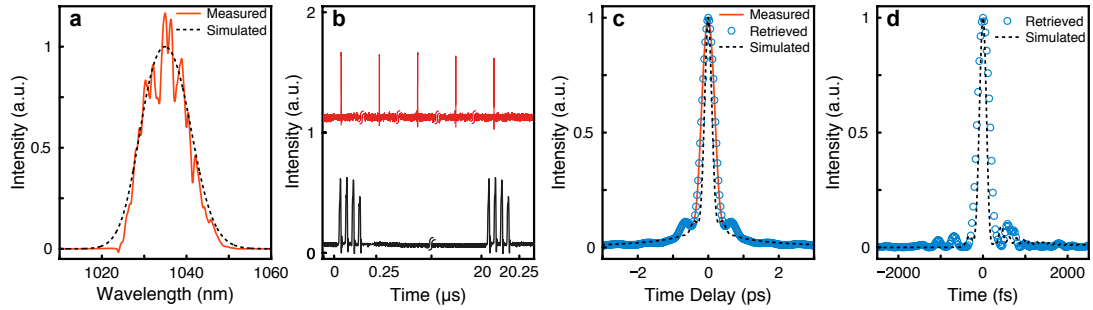


Figure A.6: For $8 \mu\text{J}$ compressed pulse energy: (a) measured optical spectrum, (b) measured temporal profile of 200 kHz pulses and 4-pulsed bursts, (c) measured, simulated and PICASO-retrieved autocorrelation, (d) inferred pulse shape using the PICASO algorithm and simulated pulse shape.

Amplified signal is extracted via a dichroic mirror which transmits the pump and reflects the signal wavelengths. We used numerical simulations to guide the experimental design. The details of the simulations can be found in [80]. The simulations predict pulse duration of 200 fs for $8 \mu\text{J}$ shown in Fig. A.6(c). The retrieved pulse form (Fig. A.6(d)) from measured autocorrelation and spectrum with PICASO algorithm [81], indicates ~ 300 fs FWHM. This result is in close agreement with the simulation, while the effective pulse width of 375 fs of the retrieved pulse reflects the effect of the pedestal caused by the interaction of uncompensated third order dispersion and nonlinearity. Even higher pulse energies (up to $40 \mu\text{J}$) can be generated, but result in longer pulses due to increased nonlinear phase accumulation.

Following dechirping, a high-power isolator is placed to prevent back reflections from the target. The optimized transmission of the compressor, half-wave plate and polarizing isolator (which allows continuous reduction of power) is 80%. The beam is then expanded with a telescope to completely fill the aperture of a 2D galvanometer scanner (ScanCube 14, ScanLab).

A.3 500 MHz intra-burst repetition rate, 1 ps pulse duration

A 1030-nm Yb-doped burst mode fibre laser system seeded by a 500-MHz oscillator was used for hard tissue experiments. The system consists of three stages of core-pumped fibre pre-amplifiers, a double-clad fibre power amplifier, which were controlled by a field programmable gate array (FPGA) (Spartan 3E, Xilinx, Inc, San Jose, CA, USA) for synchronized pulse picking and pulsed pumping. The laser amplifier is largely identical to the one described in a previous publication [35]. The beam positioning setup consists of a 3-axis motorized stage (MAX343, Thorlabs, Newton, NJ, USA), 10x focusing objective (LMH-10X-1064, Thorlabs) and imaging setup including a CCD camera (DCC 1545M, Thorlabs) and a dichroic mirror, a focusing lens, an IR filter. The laser spot diameter is estimated to be 12 μm , confirmed by directly observing craters on the surface of a copper plate and independently by the knife-edge method.

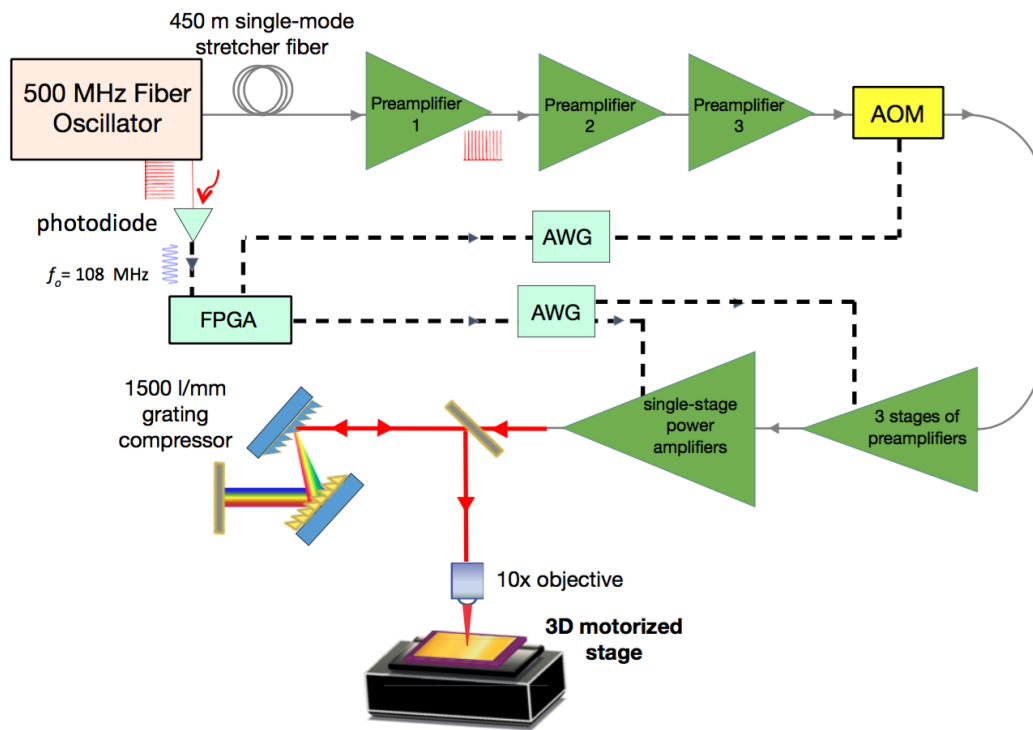


Figure A.7: Laser, optical scanning and sample positioning setup custom-built for the hard-tissue and piezoelectric ceramic cutting experiments.

Appendix B

Parameters of Toy Model in Figures

The parameters that were used in obtaining the predictions of the toy model for the ablation with 800-pulse bursts of 3456-MHz intra-burst repetition rate and 25-pulse bursts of 108-MHz intra-burst repetition rate, along with the results for 100-pulse bursts at 432 MHz intra-burst repetition rate are as follows for the silicon target:

- $\frac{\tau_B}{\tau_0} = 10/\eta$
- $T_c = 15000(K)$
- $T_0 = 300(K)$
- $\Delta T = \frac{20E_{burst}}{N}(K/\mu J)$
- $\beta = 23(\mu m^3)$
- $N = 25\eta$

where $\eta = 1, 4$ and 32 for repetition rates of 108 MHz, 432 MHz and 3456

MHz, respectively. For 1 MHz and 25 MHz, $\eta = 0.25$, *and* 0.01, while N remains equal to 25.

The parameters that were used in obtaining the predictions of the toy model for the ablation with 800-pulse bursts of 3456-MHz intra-burst repetition rate and 25-pulse bursts of 108-MHz intra-burst repetition rate, along with the results for 100-pulse bursts at 432 MHz intra-burst repetition rate are as follows for the copper target:

- $\frac{\tau_R}{\tau_0} = 12.5/\eta$
- $T_c = 15000(K)$
- $T_0 = 300(K)$
- $\Delta T = \frac{20E_{burst}}{N}(K/\mu J)$
- $\beta = 24(\mu m^3)$
- $N = 25\eta$

where $\eta = 1, 4$ *and* 32 for repetition rates of 108 MHz, 432 MHz and 3456 MHz, respectively. For 1 MHz and 25 MHz, $\eta = 0.25$, *and* 0.01, while N remains equal to 25.

The parameters were chosen to correspond to values for simulations of Si described in Chapter 2.2 and for tabulated data for Cu in Table 4.1. The β parameter was calibrated based on experimental values in Fig. 4.2, as it could not easily be determined from the theory.